Spectral And Timing Properties Of Class Variable Source GRS 1915+105 Using Two Component Advective Flow Solution

Thesis Submitted for the Degree of
Doctor of Philosophy (Science)
in
Physics (Theoretical)

by
Anuvab Banerjee

Department of Physics
University of Calcutta
2021

...To my parents

Acknowledgements

After the long stretch of several years, now is the time to look back and convey the note of thanks, gratitude and appreciation to all who are deeply involved in this extensive process of learning, gaining experience and becoming acquainted with some aspects of life hitherto unexplored. Requirements of a Ph.D. ideally demand a complete reorientation of one's thinking process as well as the problem solving approach, and cumulative effect of day-to-day infinitesimal changes make this journey a life changing experience. The people with whom we are connected during this phase of ups and downs also become special.

First of all, I would take this opportunity to convey my sincerest gratitude to my supervisor Prof. Sandip K. Chakrabarti who has been a wonderful person with his continuous support, constant enthusiasm and motivation. Long discussions with him are always fruitful and enriching because of his insight and exceptional command over the literature related to the subject. He has always insisted to be precise and brief while drafting the manuscripts and consideration of his suggestions have always elevated the quality of every manuscript I have drafted so far. His direct and sharp questions during the scientific talks in conferences I have attended so far was also a source of indirect way of gaining further insight into the subject.

With almost no background in the methodology of scientific research during my Master's days, I was finding myself to be a fish out of water during the initial days of my research career. I consider myself to be immensely fortunate to have my childhood friend *Ayan* with me since day one of my stay in my institute. I have barely met a person so far possessing this level of unrelenting dedication, intellectual stamina, level-headedness and multitudinous inherent talent who oozes his genius through his action and word. I have learnt from him the art of breaking complex scientific problems with smaller actionable pieces and managing them independently. Deep long con-

versations with him that I have had in almost all topics of the world were really eye-openers.

Shortly after my admission in SNBNCBS, my M.Sc. friend *Atanu* joined the institute, and with him I came to know *Juriti* as well during our mess managership. There are so many precious moments I have savoured with both of them including our local outings, sudden food hunts, directionless gossip during our idle moments and so on. Both of them have been caring enough to listen to my problems and giving counsel whenever I faced any hardship. During the preparation of our coursework, I got to know two of my constant companions: *Samrat* and *Dhrimadri (Khata)*. Samrat possesses the unique talent of perking up the atmosphere with his quirky jokes and comically candid way of airing his frustration that lifts up our temper instantly, whatever the situation may be. Khata is idiosyncratic in his own way with his sudden, unpredictable mood swing, his intense passion on football, his unique ability to make us giggle by his sheer presence. I am fortunate to have a friend like *Shreya*, who has been almost a sister to me during my Ph.D. tenure. Apart from being a constant companion in everyday affair and unadulterated banter, she is one of my most trusted confidant to share my problems and worries and having assuring practical suggestions. Given my interest in theoretical physics, I have always enjoyed hour long discussions with *Debabrata (Debu),* another friend from my M.Sc. days. Questions popped up during such discussions have inwardly prompted me to think deeper and investigate further during my research. I can't quite remember how I first ran into *Mahebub*, but having such a friend by my side was always a source of joy, encouragement and support. Deep conversations with him during our aimless nightwalk was always soul filling. Our fun filled evenings with *Suchetana*, local trips and unbridled gossip that I so dearly miss now used to always inculcate a fresh lease of life and refreshed me with rejuvenated exuberance. I am lucky to have come across such a friend who has always been patient enough to listen to my problems and giving comfort. With his distinct trait of cracking oddball jokes and being always pleasurable, *Arnab* is really someone special to have who never lets the mood sink. My fun-filled short outings with Arnab, Shreya and *Tuhin*, another friend of mine with his cheerful presence, has always been a treasurable experience to have. I miss the relentless enthusiasm of *Mithun* and *Sayani* in arranging our occasional gatherings. Without friends like you, days of Ph.D. would have been extremely gruelling and far less colorful. I thank everyone for being a part of my life during these days of mine. In the natural course of life we may grow apart after our Ph.D. days

and initially the life would feel quite drab and lonesome, but the warmth of this years of togetherness and long montage of memories would forever be there to cherish, would always be there to look back and draw spirits to enliven ourselves in our tougher days.

I am very fortunate to have juniors like *Prantik* and *Piklu* in our group, both of whom are more of my friends than juniors. Apart from being a source of constant entertainment and humorous exchanges, frequent discussions with Prantik has really benefitted me during my research period. Piklu has always been down-to-earth and practical in his approach, and academic exchanges with him has always been quite enjoyable and thought provoking. My other junior *Ruchi* has always been forthcoming with encouragement and suggestions during the hours of need. Her dedication to work and expertise in her field of study are quite inspiring. I really miss the charm of my gleeful evening outings with Ayan and Ruchi after a day long toil that so refreshingly made me forget the frustrations of the day and prepared me for a new tomorrow. *Bihalan* and *Pallabi* has always made our gatherings more enjoyable with their lively presence. Whenever needed, I got *Riddhi*, yet another junior of mine, for discussions and counsel. It was a joy to have juniors like *Siddhartha, Sourav, Riju, Subhadip, Dipanjan, Subrata, Dipika* and so on during my Ph.D. days, each of whom are special in their own way.

I am deeply indebted to *Partha Da*, from whom I first gained the hands-on lessons of data analysis, which has been immensely helpful during my research career so far. He was kind enough to scrutinize our approach towards a problem during the early days and suggesting fruitful techniques to gain further insight into the data. *Arindam Da* has always been a great source of motivation, enthusiasm and encouragement because of his incredible passion in the subject, his keen attention to details and his thoughtful suggestions. Hour long discussions with him has developed my understanding a lot. I am thankful to *Dipak Da* for his suggestions and comments during manuscript preparation and analysis. I thank *Arka Da, Broja Da, Kingshuk Da and Sudip Da* for academic discussions in various occasions. *Supriyo Da* has always been helpful with comments and suggestions after carefully listening to my problems. I always enjoy the lively interaction with *Sudipta Da, Ankan Da and Rito Da* in different occasions whenever we got together. I am thankful to my seniors in SNBNCBS like *Arnab Da, Abhishek Da, Somnath Da, Anindita Di and Victor* for providing me a caring and loving atmosphere that made the Ph.D. days so enjoyable. I thank my friends, colleagues and juniors in ICSP, i.e. *Shreeram, Argha, Debjit, Kaushik and Aslam* for their

care, support and fruitful suggestions.

I still cherish the invaluable bonds built during my M.Sc. with *Anirban, Maitrayee, Pranjal, Sagarika, Promita, Subrata, Pallabi, Soumi, Pratik, Sanket, Pallab and Sekhar*, each of whom opened a new unexplored world before me and made those days so incredibly special. My outings with Pratik, Sanket, Pallab and Sekhar, along with Samrat and Mahebub are experiences to be treasured in the deepest of my heart for the rest of my life.

I am deeply indebted to Dr. Ramkrishna Das of SNBNCBS who was assigned to handle official matters in the capacity of an *officiating supervisor* after the superannuation of Prof. S.K. Chakrabarti. Dr. Das has helped me streamlining all the official processes leading to the timely submission of this Thesis. I am thankful to Prof. Soumen Mondal and Prof. Archan Majumder for my interactions with them in various occasions during my Ph.D. I am also thankful towards Dr. Tilak Katoch (TIFR) for my interactions with him during the collaboration and his insightful comments that broadened my understanding regarding some of the analysis techniques. I convey my gratitude to Prof. H. M. Antia (TIFR) for carefully examining the manuscript during our collaboration and offering valuable suggestions that improved the quality of the manuscript.

It would not have been possible to pursue my research career without the encouragement, unconditional support and constant motivation from my loving parents *Prabir Banerjee* and *Mamata Banerjee*. It is not possible for me to express my gratitude towards them in my feeble words, so I will not make such fruitless attempt. This thesis is for my parents. Throughout my Ph.D. I have probably turned down many many offers of family gatherings and outings, which I realise now is part and parcel of every Ph.D. student. I owe all my family members my deepest gratitude for letting me indulge in my routine and taking my decisions independently.

I gratefully acknowledge the funding sources that made my Ph.D. work possible. I was funded by SNBNCBS fellowship during my Ph.D. tenure and the institute allowed me to have an one year extension, which was extremely helpful. I thank *Chandrakana Di* and *Rupam Da* for always being cooperative and helpful in any official matter.

List of Publications

The thesis is based on the following publications

1. **Spectral Analysis of χ Class Data of GRS 1915+105 Using TCAF Solution** by **Anuvab Banerjee**, Ayan Bhattacharjee, Dipak Debnath, Sandip Kumar Chakrabarti, 2020, accepted in RAA, (arXiv: 1905.01538v2).

2. **Accretion Flow Properties of GRS 1915+105 During Its θ Class Using AstroSat Data** by **Anuvab Banerjee**, Ayan Bhattacharjee, Debjit Chatterjee, Dipak Debnath, Sandip Kumar Chakrabarti, Tilak Katoch & H. M. Antia, 2020, (submitted to ApJ), (arXiv:2007.05273).

3. **Similarities and Differences in Accretion Flow Properties between GRS 1915+105 and IGR J17091-3624: a Case Study** by **Anuvab Banerjee**, Ayan Bhattacharjee , Dipak Debnath and Sandip K. Chakrabarti (2021, under communication, arXiv:2101.11854v1)

Publications not included in the thesis

1. **Signatures of two-component flow in the λ class of GRS 1915+105** (manuscript in preparation)

2. **Constraining Mass of Cygnus X-1 from Analysis of the Hard State Spectral Data using TCAF Solution** by Indrani Baneree, Ayan Bhattacharjee, **Anuvab Banerjee**, Dipak Debnath and Sandip K. Chakrabarti, 2020, under communication (arXiv 1904.11644v1)

3. **AstroSat Observation of Non-Resonant Type-C QPOs in MAXI J1535-571** by Debjit Chatterjee, Dipak Debnath, **Anuvab Banerjee**, Ayan Bhattacharjee, Arghajit Jana, Kaushik Chatterjee, R. Bhowmick, S. Nath, J. R. Shang, S. K. Chakrabarti & H. K. Chang, 2020, (under communication) (arXiv:2006.09077)

4. **The 2004 outburst of BHC H1743-322: analysis of spectral and timing properties using the TCAF solution**, by Ayan Bhattacharjee, Indrani Banerjee, **Anuvab Banerjee**, Dipak Debnath, Sandip K Chakrabarti in Monthly Notices of the Royal Astronomical Society, 2016, 466, 1372-1381

Chapter in books

1. Chapter **"Spectral and Timing Analysis of Transient, Persistent and Variable Black Hole X-ray Binaries: The Present Viewpoint"** in Springer Book *"Exploring the Universe: From Near Space to Extra-Galactic"*, Editors: Banibrata Mukhopadhyay & Sudipta Sasmal, 2018, ASSP, 53, 283 (DOI: 10.1007/978-3-319-94607-8) [Book ISBN : 978-3-319-94606-1 (hardcopy); 978-3-319-94607-8 (ebook)]

Contents

List of Figures

Chapter 1

Introduction

1.1 Introduction

A comprehensive analysis of any physical system and making inferences requires two things: conducting experiments and collecting data as well as coming up with plausible hypotheses based on physical laws to explain the observation. In case the hypothesis can predict future observations within the statistically acceptable limit, that provides further confidence to the legitimacy of that hypothesis in describing the underlying physical system in prescribed conditions. One important component in effectuating this procedure is to set up tabletop experiments and study the system as a function of different adjustable parameters. This is a useful way to understand the evolution of the system as the corresponding parameters evolve.

Unfortunately, this well-recognized time-tested methodology of studying nature needs to be revised when it comes to astrophysical systems. Due to the extreme conditions corresponding to the systems, it is not possible to reproduce them in an experimental setup and study the sensitivity with respect to dynamical parameters. As a result of this, it is necessary to rely on direct observational data of astrophysical sources and indirect observational evidence to understand and infer about such systems. Thanks to the tremendous improvement of the detection capabilities of astronomical satellites over the past four decades, as well as the dedicated and concerted effort of the scientific community worldwide to post-process, categorize and archive the huge wealth of data for wider usage, the scientific community has now the opportunity to test physically relevant models against observational findings.

This has given the discipline of astrophysics the deserved momentum, which is inspiring the new generation of observers and theoreticians to push the envelope further and come up with more comprehensive models to understand the astrophysical systems.

X-ray astronomy provides the required window to study astrophysical compact objects such as black holes, neutron stars and white dwarfs. The X-ray observation of astrophysical sources cannot be undertaken from ground-based observation capabilities owing to the absorption of X-rays in Earth's atmosphere. Therefore, one must consider space-based facilities for this purpose. The first significant discovery to demonstrate the Sun as a source of X-ray emission was carried out after World War II (Friedman et al., 1951). It took almost a decade to arrive at the deserved sensitivity and technological capacity to detect the first extra-solar X-ray emitting object (Giacconi et al., 1962). This source was later named Scorpius X-1 (Sco X-1). Subsequent to this discovery, some other phenomenal investigations and discoveries followed which include: (1) discovery of optical counterpart of Sco X-1, (2) discovery of active galaxy M87, (3) micro-flare detection of Sco X-1, and (4) detection of crab nebula. In the subsequent decades, the launching of other X-ray telescopes such as Rossie X-ray Timing Explorer (RXTE), BeppoSAX, Swift, Chandra X-ray observatory, XMM Newton, etc. has taken the field of astronomy to new heights.

Among the X-ray sources, the X-ray binaries are particularly interesting to investigate. The X-ray binaries belong to a category of binary stars which are luminous in X-rays. X-rays are generated as the stellar matter is accreted from the companion star (typically a normal star) onto a compact object. Details of this accretion and X-ray emission processes will be discussed later in this Chapter. Studying X-ray binaries is particularly fascinating since this provides a unique window to examine the physics of a strong gravity region filled with the matter in extreme conditions. Apart from this, the extensive observation of these X-rays in the time or energy domain enables us to comment on the dynamics of the central object indirectly.

Gathering the photons released by the accreting systems and using them for different purposes is one crucial component of X-ray astronomy. With the rapid advancements in the study of semiconductor devices, more accurate and robust detection systems have been launched into operation for throwing new light on the present understanding. More sophisticated devices have ensured greater precision and accuracy of detection. Once the photons are accumulated by the detectors, they can be primarily used in two ways: (a)

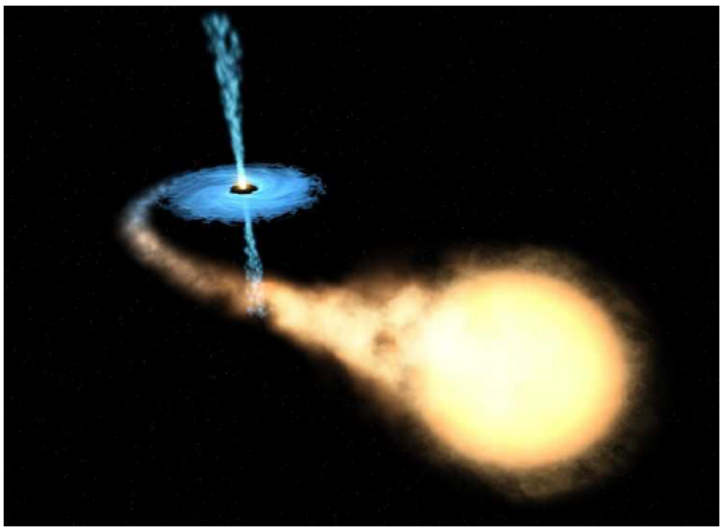

Figure 1.1: Artist's impression of accretion process onto a compact object. Matter is released from the companion star and captured by the compact object. Figure is adopted from Wikipedia.

photons can be binned in time so that the evolution of the source with the passage of time could be recorded, and (b) photons can be binned with respect to their respective energies, which is known as a 'spectrum'. Further, the pixel distribution of the photons becomes helpful to detect the source and measure the background contribution as well, and this is known as 'imaging'. In this thesis, we have mainly carried out all our analyses involving the first two methods only. We provide below the nuances of each of these methods.

1.2 Methods of Analysis

1.2.1 Timing Analysis

Statistical and analytical tools are indispensable in the timing analysis in order to make sense of the time series. Fourier analysis turns out to be extremely helpful in such situations, which we will briefly describe below.

Fourier Analysis Techniques

The Fourier power spectrum of the underlying time series provides the variance of power density $P(\nu)$ as a function of the frequency of photon detection ν (van der Klis 1989). The power spectrum is constituted by several variability components or power spectral components. Any underlying aperiodic element is spread over a large frequency domain, while certain periodic components are confined within a narrow frequency domain. Broad structures are known as 'noise' components and the narrowly confined structures on top of the noise are known as peaked components.

There are different types of frequency dependence of noise components. The power-law noise, as the name suggests, maintains a power-law relationship with frequency ($P(\nu) \sim \nu^{-\alpha}$). The power-law index α lies between 0 and 2. The detection of a power-law index of more than 2 is not reliable for power leakage problems (Bracewell 1986). In case the frequency dependence is flat across the frequency range ($\alpha = 0$), it is known as the white noise. The $\alpha = 1$ case is known as 1/f noise. In case $P(\nu)$ decreases with frequency, it is known as red noise.

The Band Limited Noise (BLN) is that kind of noise that gradually steepens towards higher frequency ($\frac{-d\log P}{d\log \nu}$ reduces with ν). In case power density remains almost constant below a particular cut-off frequency for BLN, it is known as the flat-topped noise. The steepening of noise can be gradual or abrupt (with a break) depending on the system under consideration.

The distinct peaked structures in the PDS are particularly important features since they are indicative of some characteristic oscillation of the system, known as the 'Quasi-Periodic Oscillation (QPO)'. Typically, they are described using Lorentzian profiles $P(\nu) \propto \lambda/((\nu-\nu_0)^2 + (\lambda/2)^2)$, where ν_0 is the centroid frequency and λ is full-Width at Half Maxima (FWHM). This is actually the Fourier transform of the exponentially damped harmonic oscillator. The quality factor, alternatively the coherence $Q = \nu_0/\lambda$ is a crucial determinant in qualifying a peak as a QPO. Typically for a QPO, this quantity has to be more than 2.

The strength of the QPO depends on the integrated power, which is $\propto Q$. Typically it is expressed as a ratio with the total power output of the source. For a peak to qualify as a QPO, the RMS power has to be significant (at least 5-6%).

As the source evolves over time, the various power spectral components can also evolve and change their characters. Therefore when one source is

analyzed over successive data blocks over a long time, peaked components can make a transition to noise components and vice versa. For this reason, sometimes it is suggested that any particular instance of PDS should not be considered in isolation but as a realization of the continuous evolution of source states. A clear band-limited noise component can manifest itself as a QPO or vice versa with the evolution of the source (Di Salvo et al., 2001). For this reason, PDS of both BHCs and neutron stars have been later analyzed using a combination of Lorentzian components only, some of which are broad (Q < 1) (Miyamoto et al., 1991, Nowak 2000; Belloni, Psaltis & van der Klis, 2002).

Red noise or BLN has only one characteristic frequency (break frequency), but QPO and peaked noise have two (centroid frequency and FWHM). This poses a challenge in describing QPO evolution and detecting the transition of QPO to peaked noise. For this reason, it is often helpful to track the variation of frequency times power density ($\nu P(\nu)$) instead (Belloni et al., 2002). In the X-ray analysis software HEASOFT, inbuilt tools are provided to subtract the white Poisson noise from the data.

1.2.2 Spectral Analysis

A combination of timing studies with spectroscopic diagnostics can significantly enhance the understanding of physics near compact objects. Two dominant methods are followed for the purpose of spectral variation detection (changes in $\delta E/E$): multi-band photometry and spectral fitting method. We describe these two procedures briefly.

Multi-Band Photometry

The excursions of the source can be quantified by defining X-ray *colors*, which is nothing but the ratio of photon intensity in two different energy bands. Photons in the higher energy band are of *hard color*, and those in the lower energy band are of *soft color*. Often it is useful to record the dynamics of the source as a function of 'hardness ratio' (ratio of photons in higher and lower energy band), which is a measure of the spectral slope. The broadband spectral variation often corresponds to the power spectral variations as well. In case the two colors are plotted against one another (color-color diagram; CD hereafter), the source is often found to move through the diagram and create certain patterns. However, one must note that these patterns may be

artifacts of the chosen hard and the soft band as well and may not reflect any deeper physical insights. Such patterns are often found in Hardness-Intensity Diagrams (HID) or color intensity diagrams as well, which are nothing but the plot of color vs. intensity of the source.

The combination of photometry with timing studies provides a convenient methodology in categorizing the source variations, but this is quite dependent on detector sensitivity variations. There is a broad inhomogeneity in X-ray detectors and their performance is time-dependent. It becomes problematic to correct the X-ray color with detector response. Therefore, without an active knowledge of intrinsic spectral characteristics, the measured spectral properties are blended with imperfections driven into the detection process by the detector itself. Contrary to optical photometry, there is only one bright standard source (Crab). The process of scaling by Crab colors and unfolding through the detector response matrix, consequently, suffers from intrinsic imperfections (Kahn & Blisset, 1980; Kuulkers et al., 1994).

Spectral Fitting method

The description and making inferences regarding X-ray spectral variations in terms of physical models turns out to be the complementary method to multi-band photometry. It involves more quantities for the full spectral description, contrary to photometry which requires only 2-3 parameters (like X-ray colors). This can lead to interpretive degeneracies, redundancies, and also spurious correlations between model parameters which can lead to misleading conclusions as well. Even with these few drawbacks, carefully crafted model-dependent spectral analysis coupled with adaptive adjustment and modifications of the models in the face of new observations have met with considerable success in the past few decades. Effective spectral fitting requires longer integration time as compared with the timescales in which X-ray color variations are measurable. Comparison of synthetic time series, PDS, and spectral variations with the detected ones and extraction of model parameters via spectral fitting provides a detailed physical description of the accretion flow around the source.

1.3 Radiative Processes in X-ray Astronomy

In the universe, a large majority of astrophysical objects are recognized by their electromagnetic emissions ranging from radio to γ rays. The generation of this radiation in different frequency bands depends upon the details of the physical processes involved and the nature of the medium. In the case of black hole astrophysics, radiation is predominantly obtained in the X-ray domain. All the emission mechanisms can be broadly divided into two subcategories: thermal and non-thermal emissions (Rybicki & Lightman, 1979). We discuss below some of the important emission processes relevant to X-ray astronomy.

1.3.1 Thermal Emission

Thermal emission is observed in the case of any matter with a finite temperature. The thermal motion of electrons is responsible for this emission. The intensity and distribution of photons are governed by the temperature of the radiating source. We discuss the dominant thermal radiation processes in some detail.

Blackbody radiation

Black body radiation is emitted by a medium that is in perfect thermodynamic equilibrium with its surroundings and also with itself. It has a characteristic continuous energy spectrum such that once the temperature of the system is fixed, its energy spectrum is completely determined. The energy distribution of photons obey Planck's law

$$B_\nu(T) = \frac{2h\nu^3}{c^3} \frac{1}{\exp\left(h\nu/k_B T\right) - 1}, \tag{1.1}$$

where h, k_B, and ν are Planck's constant, Boltzmann's constant, and the frequency of the photon respectively. T is the characteristic temperature of the system. The spectrum is peaked at a characteristic frequency which shifts towards a higher frequency domain with increasing temperature of the system. The population of particles in two different energy levels E_1 and E_2 follow Boltzmann distribution law

$$N_1/N_2 \propto \exp[-(E_2 - E_1)/k_B T]. \tag{1.2}$$

This emission mechanism would be dominant for accreting matter with high angular momentum but negligible radial momentum. Such mediums are known to be 'optically thick' since the photons encounter many collisions before being released from the medium. Since the radiation energy density varies as T^4, the total energy output rapidly increases with the increase of temperature.

Thompson Scattering

Thompson scattering is observed during elastic scattering between photons and non-relativistic charged particles. During the scattering event, the photon is absorbed by the charged particles and another photon is re-emitted. The differential cross-section for the Thompson scattering is given by

$$\frac{d\sigma}{d\nu} = \frac{1}{2}(1 + \cos^2\theta)r_0^2, \tag{1.3}$$

where $r_0 = \frac{e^2}{mc^2}$ is the classical electron radius. The integrated cross-section is given as

$$\sigma_T = 2\pi \int_0^\pi \frac{d\sigma}{d\nu} \sin\theta d\theta = \frac{8\pi}{3}(\frac{q^2}{mc^2})^2. \tag{1.4}$$

In case of scattering with the electrons, this total cross section turns out to be $6.65 \times 10^{-25}\text{cm}^2$. The cross section heavily depends on mass. In case of scattering with photons, the cross section is smaller by a factor $(\frac{m_p}{m_e})^2 \sim 10^6$.

Thompson scattering becomes very important in the radiative output of accreting matter. Any photon produced within the material interacts with the surrounding electrons. In this way, energy is exchanged between photons and electrons. The escape probability of the photons from the accreting medium depends on the optical depth, which is given by

$$\tau = \int n_e \sigma_T dx, \tag{1.5}$$

where n_e is the electron density and dx is the differential line element along the line of sight. The mean free path of the photons $(1/n_e\sigma_T)$ decides the level of energy exchange between the photons and the medium.

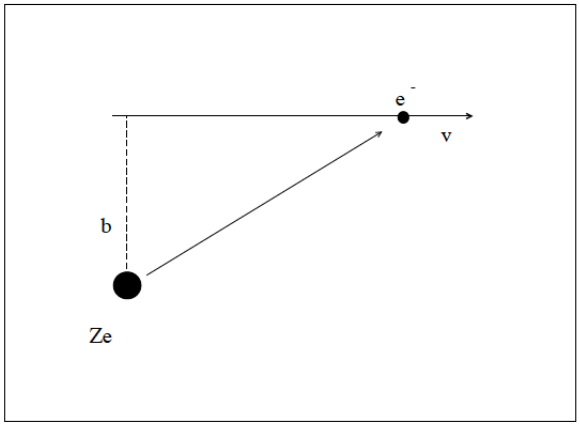

Figure 1.2: An electron of charge e moving in the electric field of a neighbouring ion of charge Ze. The impact parameter is b (From Rybicki & Lightman (1979)).

Classical Electron-ion Bremsstrahlung

Bremsstrahlung is the electromagnetic radiation produced due to the acceleration of a charged particle under the influence of a neighboring charged particle. The loss of kinetic energy of the moving particle is converted to the energy of a photon, maintaining the conservation of energy. Classical non-relativistic and relativistic treatments of the Bremsstrahlung process approximate to a significant extent the real-world observations.

In the case of an electron of charge $-e$ moving past an ion with charge Ze with impact parameter b (Figure 1.2). The second derivative of the electric dipole moment is $\ddot{\mathbf{p}} = -e\dot{\mathbf{v}}$. The Fourier transform of this equation reads as

$$-\omega^2 \mathbf{p}(\omega) = -\frac{e}{2\pi} \int_{-\infty}^{\infty} \dot{\mathbf{v}} \exp(i\omega t) dt, \tag{1.6}$$

The collision time could be defined as $t_c = \frac{b}{v}$. For asymptotic limit ($\omega t_c >> 1$), the exponential term does not dominate because of large number of oscillations. On the other end, for $\omega t_c \ll 1$, the exponential is almost unity. Therefore, (6) could be rearranged as

$$\mathbf{p}(\omega) \sim \frac{e}{2\pi\omega^2} \Delta v, \qquad \omega t_c \ll 1, \tag{1.7}$$

where Δv is the change in velocity during the collision. The total liberated energy per unit frequency range per unit solid angle is given as

$$\frac{dW}{d\omega} = \frac{2e^2}{3\pi c^3}(\Delta v)^2. \tag{1.8}$$

In the case of small-angle scattering, the change in velocity is particularly normal to the path and it reads as

$$\Delta v = \frac{Ze^2}{m_e}\int_{\infty}^{\infty} \frac{bdt}{(b^2+v^2t^2)^{3/2}} = \frac{2Ze^2}{m_e bv}. \tag{1.9}$$

Substitution of this expression yield the final radiation density to be

$$\frac{dW}{d\omega} = \frac{8Z^2e^6}{3\pi c^3 {m_e}^2 v^2 b^2} \tag{1.10}$$

Thermal Bremsstrahlung

In order to determine the effects of Bremsstrahlung on a population of electrons and ions in a plasma cloud of densities n_e and n_i respectively, the emission per unit time per unit volume per unit frequency is given as

$$\frac{dW}{d\omega dV dt} = 2\pi n_e n_i v \int_{b_{min}}^{b_{max}} \frac{dW}{d\omega} b db, \tag{1.11}$$

where all the ions and electrons in a shell of differential area $2\pi b db$ have been considered. Here b_{min} and b_{max} are the minimum and maximum of the impact factor. Simplification of this equation yields

$$\frac{dW}{d\omega dV dt} = \frac{16e^6}{3c^3 {m_e}^2 v} n_e n_i Z^2 \ln(\frac{b_{max}}{b_{min}}). \tag{1.12}$$

One additional parameter, known as the Gaunt factor (g_{ff}) needs to be incorporated in this equation, which is a function of energy of the electrons and emission frequency. This equation needs to be weighted by thermal velocity distribution and integrated to obtain the power output as

$$\frac{dW}{d\omega dV dt} = \frac{\int_0^{\infty} \frac{dW}{d\omega dV dt} f(v) dv}{\int_0^{\infty} f(v) dv}, \tag{1.13}$$

where $f(v)$ is the thermal velocity distribution of electrons

$$f(v)dv = 4\pi(\frac{m}{2\pi k_B T})^{3/2} v^2 \exp(-\frac{mv^2}{2k_B T})dv. \tag{1.14}$$

Considering $d\omega = 2\pi d\nu$ and performing the integration, one obtains the emissivity due to thermal Bremsstrahlung as

$$\Lambda(\nu) = \frac{2^5 \pi e^6}{3m_e c^3}(\frac{2\pi}{3mk_B})^{1/2} {T_e}^{-1/2} Z^2 n_e n_i \exp(-h\nu/k_B T) \bar{g_{ff}}, \tag{1.15}$$

where $\bar{g_{ff}}$ is the velocity averaged Gaunt factor. If, on the other hand, protons are moving in a high electron density plasma cloud, the process is called 'inverse bremsstrahlung'. The energy output, however, is lesser in this case because of the higher rest mass of the protons.

Compton Scattering

Compton scattering involves the momentum transfer between a photon and a charged scatterer, such as the electron. In the case of low energy photons ($h\nu \ll m_e c^2$, m_e is the mass of an electron), the scattering event reduces to that of Thompson scattering. In such a case, the incoming radiation does not experience any change in wavelength. However, for high energy photons, the recoil effect of the scatterer will be significant, and the quantum correction could not be ignored. The scattering will therefore be no longer elastic.

The energy exchange and the modulation of photon's frequency due to the scattering event could be determined from the momentum and energy conservation relationships in the rest frame of the electron. The four momentum of the incident and scattered photons can be taken as $P_{\gamma i} = (\epsilon/c)(1, \mathbf{n_i})$ and $P_{\gamma f} = (\epsilon^{'}/c)(1, \mathbf{n_f})$ respectively, where $\mathbf{n_i}$ and $\mathbf{n_f}$ are the unit vectors along incident and scattered directions (Fig. 1.3). The initial and final four momentum of the electron in its rest frame would be $P_{ei} = (m_e c, \mathbf{0})$ and $P_{ef} = (E/c, \mathbf{p})$ respectively. Employing energy and momentum conservation, we obtain

$$\epsilon^{'} = \frac{\epsilon}{1 + \frac{\epsilon}{m_e c^2}(1 + \cos\theta)}, \tag{1.16}$$

such that the change in wavelength is given as

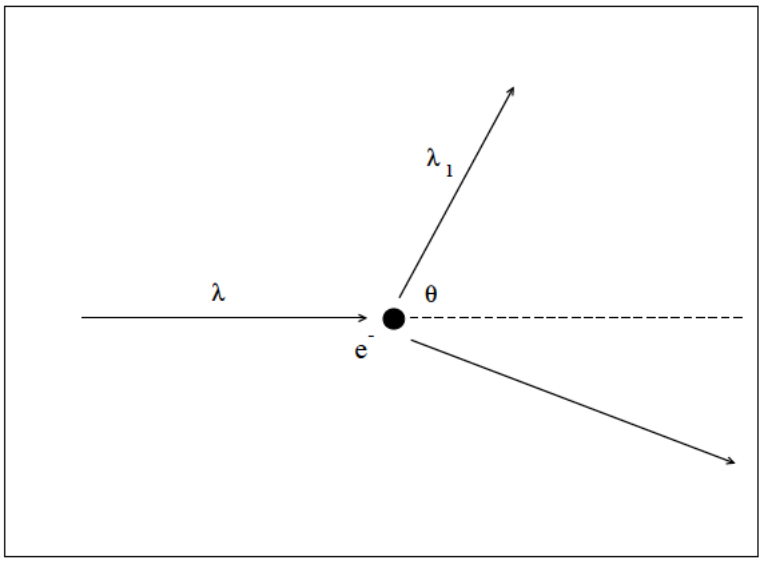

Figure 1.3: Scattering of an incident photon by an electron. The deflection angle is θ. Figure is adopted from Rybicki & Lightman (1979).

$$\lambda^{'} - \lambda = \Delta\lambda = \lambda_c(1 - \cos\theta), \tag{1.17}$$

where $\lambda_c = \frac{h}{m_e c}$ is the Compton wavelength and λ and $\lambda^{'}$ are the initial and final wavelengths of the photon. Therefore, the shift in wavelength is $\sim \lambda_c$. For $\lambda \gg \lambda_c$, the scattering is almost elsatic.

The differential scattering cross section for Compton scattering is obtained by Klein-Nishina formula using the quantum electrodynamic inputs. The formula reads as

$$\frac{d\sigma}{d\Omega} = \frac{{r_0}^2{\epsilon_1}^2}{2\epsilon^2}(\frac{\epsilon}{\epsilon_1} + \frac{\epsilon_1}{\epsilon} - \sin^2\theta). \tag{1.18}$$

With $\epsilon \sim \epsilon_1$, this yields the classical Thompson scattering cross-section.

The situation becomes more interesting in the case of scattering of photons by moving electrons. The energy of photons in the laboratory frame and rest frame of the electron, using the Doppler shift formula, are respectively obtained as

$$\epsilon^{'} = \gamma\epsilon(1 - \beta\cos\theta), \tag{1.19}$$

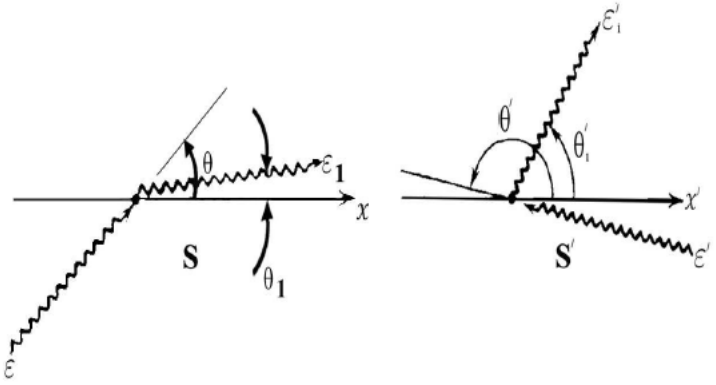

Figure 1.4: Scattering event in the laboratory frame and the rest frame of the electron respectively. Adopted from Rybicki & Lightman (1979).

$$\epsilon_1 = \gamma\epsilon_1'(1 + \beta\cos\theta_1'), \tag{1.20}$$

where γ is the Lorentz factor. Their relationship reads as

$$\epsilon_1' \sim \epsilon'(1 - \frac{\epsilon'}{m_e c^2}(1 - \cos\Phi)) \tag{1.21}$$

where $\cos\Phi = \cos\theta_1'\cos\theta' + \sin\theta_1'\sin\theta'\cos(\phi_1' - \phi')$, where ϕ' and ϕ_1' are the azimuthal angles corresponding to incident and scattered photons in the rest frame of the electron respectively.

Inverse Compton Scattering

In the case of inverse Compton scattering, low energy photons are scattered by ultra-relativistic electrons, as a result of which the photons gain energy at the expense of the energy of the electron. Therefore, in order for the process to happen, it needs to be ensured that $h\nu \ll m_e c^2$ in the rest frame of the electron (S'). The energy of the photons in this frame is obtained as

$$\nu' = \gamma\nu(1 + \frac{v_e}{c}\cos\theta), \tag{1.22}$$

where θ is the angle between the photon and high energy electron in the laboratory frame (S). In the rest frame of the electron, this angle would transform as

$$\sin\theta' = \frac{\sin\theta}{1 + \frac{v_e}{c}\cos\theta}. \tag{1.23}$$

The photon being of low energy, the scattering process reduces to Thompson scattering and as a result, the energy loss rate is of the electron is the same as Thompson scattering, which reads as

$$-(\frac{dE}{dt})' = \sigma_T c {U_{rad}}', \tag{1.24}$$

where ${U_{rad}}'$ is the energy density in the rest frame of the electron. The energy density in primed frame is, on the other hand,

$$U'_{rad} = [\gamma(1 + \beta\cos\theta)]^2 U_{rad}. \tag{1.25}$$

After integrating over angular coordinates, the total energy density is obtained as

$$U'_{rad} = \frac{4}{3}U_{rad}(\gamma^2 - \frac{1}{4}), \tag{1.26}$$

which finally yields

$$(\frac{dE}{dt})' = \frac{4}{3}\sigma_T c U_{rad}(\gamma^2 - \frac{1}{4}), \tag{1.27}$$

The energy of the photons needs to be subtracted from this to obtain the net energy gain by the photons, which comes out to be

$$(\frac{dE}{dt}) = \frac{4}{3}\sigma_T c U_{rad}(\gamma^2 - \frac{1}{4}) - \sigma_T c U_{rad} = \frac{4}{3}\sigma_T c \gamma^2 \beta^2 U_{rad}. \tag{1.28}$$

On the other hand, the mean number of photons with average energy $\hbar\omega$ in a population of electrons is given by $\frac{c\sigma_T U_{rad}}{\hbar\omega}$. The fractional energy gain of the photons would be

$$\langle\frac{\Delta E}{E}\rangle = \frac{4}{3}\gamma^2(\frac{v}{c})^2. \tag{1.29}$$

For a Maxwellian distribution of non-relativistic electrons, $mv^2 = 3k_B T_e$. Substitution yields, in such case,

$$\langle\frac{\Delta E}{E}\rangle = \frac{4k_B T_e}{m_e c^2}. \tag{1.30}$$

Substituting the energy of the photons as well, we obtain the average gain of photon energy as

$$\langle \frac{\Delta E}{E} \rangle = \frac{4k_B T_e - \langle E_\gamma \rangle}{m_e c^2}. \tag{1.31}$$

For inverse Compton scattering, i.e. the transfer of energy from electrons to photons to happen, the condition $4k_B T_e > \langle E_\gamma \rangle$ needs to be satisfied. This process serves as a major contributor behind the cooling of hot plasma and the generation of high energy photons to produce high energy power-law tail in spectral energy distributions. The significance of scattering is determined by the *Compton y-parameter* as well, which is the product of the average fractional energy exchange per scattering and the average number of scattering. In case $y > 1$, the scattering events can be considered quite significant.

Because of the power-law distribution of energy of electrons in an electron cloud, the consequent energy spectrum of photons is also a power-law. However, from a population of electrons with non-power-law distribution but with small optical depth, the power-law spectrum can be produced as well. In A is the average amplification factor for photon energies per scattering, then after n number of scattering events, the amplification of energy could be expressed as

$$\epsilon_{final} \sim \epsilon_{initial} A^n. \tag{1.32}$$

In this way, Compton scattering can knock up the energy of low energy photons manifold and produce a power-law tail extending up to very high energy.

Line Emission Process

When an electron from a higher energy shell makes a jump to the lower energy shell by way of some external perturbation, a photon of energy equal to the energy difference between the two shells is released. This energy is characteristic of any element which is being bombarded by high-energy particles like high-energy photons. For a particular element, this energy of an emitted photon is pre-determined because the energy levels are arranged in any element according to the quantum mechanical rules. When an electron makes a jump from L-shell to K-shell, then the emission is known as K_α line. From M-shell to the K-shell jump, the emission is called K_β line. In

the astrophysical accretion flow context, it is quite relevant and prevalent in the case of high-density matter in high energy photon fields. This will be discussed more extensively later in this Chapter.

Line emission is predominantly observed in plasmas with temperature within $\sim 10^7$K. Beyond this temperature, the electrons are no longer bound, and therefore inter-orbital jumps to produce line emissions are not possible. Therefore, only a continuum emission profile is observed beyond those temperatures. In the case of X-ray observation for stellar-mass black hole sources, the K_α emission line from Fe atom plays an important role in spectral energy distribution. The centroid frequency of this line lies at ~ 6.4 keV. However, broadening of this Iron line can also happen because of Doppler boosting, Lorentz factor, and gravitational redshift.

The broad Iron Kα lines were the first indicator of the presence of an accretion disk in Active Galactic Nuclei (AGN). In the case of Seyfert galaxies, the asymmetry of the line emission profile strongly suggests the emission from an innermost segment of the accretion disk (Fabian et al. 2000; Reynolds & Nowak 2003). Iron Kα line was first observed in the Cygnus X-1 spectrum of EXOSAT data (Barr et al. 1985). This immediately prompted interest in the scientific community to investigate such line generation processes in the vicinity of Schwarzschild black holes, which had later been generalized in Kerr metric as well (Laor 1991). The relativistic smearing of this line had also been examined by Done et al. (1992). All of these initiatives were part of a broader investigation of the illumination of the accretion disk by hard photons from some coronal region, which produces a reflection continuum as well (George & Fabian 1991). The first conclusive evidence of such line profile first appeared through the high-resolution observation by ASCA (Tanaka et al. 1995a). This broad Iron Kα fluorescence line is generally recognized as a consequence of the irradiation of the cold, weakly ionized disk by hard X-rays from the Comptonizing region. The asymmetry of the line profile can be contributed by the relativistic beaming effect and gravitational redshift.

The studies of the Kα emission line suffer from the limitation of energy resolution and uncertainty of the response matrix at $1-2\%$ because the line profile is only $1-5\%$ above the X-ray continuum. In the case of RXTE PCA, the energy resolution is only FWHM ~ 1.2 keV at Fe Kα line. Therefore, the studies of emission lines need to be exercised with caution.

Significant high-resolution emission line studies have been performed subsequently using XMM-Newton and Chandra observatory. In Miller et al. (2002a), deviation of the line profile from Gaussian has been observed, sug-

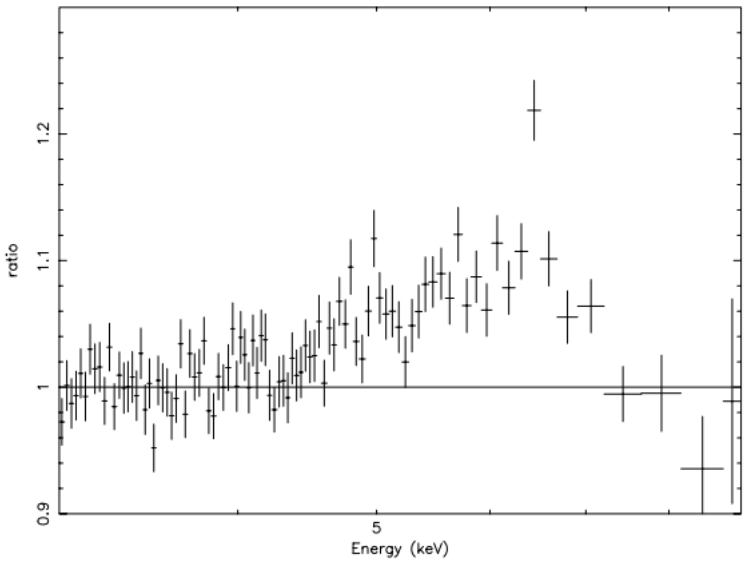

Figure 1.5: Data/model ratio for XTE J1650-500 shows excess emission around 6 keV, suggesting an Iron Kα emission. Figure adopted from Miller 2002(b).

gesting the presence of a Kerr black hole. The steady decline of luminosity with radial distance has also been reported. The investigation on Cygnus X-1 using Chandra Observatory attributed the broadening of the line predominantly to Doppler shift and gravitational redshift, as well as to Compton scattering due to reflection (Miller et al. 2002b).

1.3.2 Non-Thermal Emission

Non-thermal emission generally refers to radiation from particles having non-Maxwellian distribution. This becomes important when the amplification of particle energy happens because of agencies other than particle collision (like the magnetic field). We discuss some of the significant non-thermal emission processes below.

Cyclotron Radiation

Cyclotron radiation is the electromagnetic radiation emitted by accelerating charged particles under the influence of an external magnetic field. If mag-

netic field lines are threaded through a blob of hot plasma, then the Lorentz force on the moving particles act orthogonal to the magnetic field and the particle velocity both ($q\mathbf{v}\times\mathbf{B}$), causing the charged particles to gyrate around the field lines. In the non-relativistic limit, the radiation because of particle acceleration peaks at the gyro-frequency proportional to the magnetic field strength and inversely proportional to the particle mass ($\omega_g = \frac{eB}{m}$). For this reason, the Cyclotron frequency of electrons would be much higher compared to that of protons. The radiation is linearly polarized when viewed from orthogonal to the magnetic field lines, and appears to be circularly polarized from the end-on direction. The energy emitted per unit time is provided as

$$-\frac{dE}{dt} = \frac{\sigma_T B^2 v^2}{c\mu_0}, \tag{1.33}$$

where σ_T is Thompson scattering cross-section and μ_0 is the permeability of free space. Evidently, unless the magnetic field is significant, neither the frequency nor the emitted power is going to be significant. In some astrophysical systems with magnetic field $\sim 10^{12}$ Gauss, the Cyclotron energy can go up to ~ 30 keV as well.

Synchrotron Radiation

In the case of the motion of relativistic particles under the influence of the external magnetic field, the radiated power and frequency of radiation have a more complex dependence on the system parameters and this is known as Synchrotron radiation. For a particle of mass m and charge q moving through a magnetic field of strength B, the parallel and perpendicular components of velocity satisfy the relationship, obtained from the equation of motion of relativistic particles, as below

$$\frac{d\vec{v}_\parallel}{dt} = 0; \qquad \frac{d\vec{v}_\perp}{dt} = \frac{q}{\gamma mc}\vec{v}_\perp \times \vec{B} \tag{1.34}$$

where $\vec{v}_\parallel$ and $\vec{v}_\perp$ are the velocity components along and orthogonal to the magnetic field lines respectively. This equation implies a constant $v_\parallel$. Since motion is already orthogonal to the magnetic field, the resultant motion would again be helical around the magnetic field direction with the gyration frequency

$$\nu_B = \frac{qB}{\gamma mc}. \tag{1.35}$$

The total emitted power would be

$$P = \frac{2q^4\gamma^2 B^2}{3m^2c^5} v_\perp^2. \tag{1.36}$$

However, for an isotropic electron distribution in a plasma, one needs to average this out with respect to the pitch angles (angle between velocity of the particle and magnetic fild lines), to obtain

$$\langle v_\perp^2 \rangle = \frac{v_\perp^2}{4\pi} \int \sin^2 \alpha d\alpha = \frac{2v^2}{3}. \tag{1.37}$$

This implies, the total radiated power, after averaging over pitch angles, would be

$$P = \frac{4q^4\gamma^2 B^2 v^2}{9m^2c^5}. \tag{1.38}$$

Thus, the power is inversely proportional to the square of the mass, therefore the Synchrotron radiation strength for electrons would be overwhelmingly larger as compared to the proton counterpart (emitted power of electrons would be $\sim 10^7$ times larger).

In the case of such radiation from ultra-relativistic particles, the radiated power would not be isotropically distributed but would be predominantly confined within a narrow cone of opening angle $\phi \sim \frac{1}{\gamma}$ due to relativistic beaming effects. The pulse duration would be $\Delta t \sim 1/\gamma^3\nu$. Therefore, the pulse duration is much smaller compared to the gyration period, which makes the spectrum really broad. The emitted power per frequency interval may be written as

$$P(\nu) = \frac{\sqrt{3}q^2 B \sin\alpha}{2mc^2} F(x), \tag{1.39}$$

where $x = \nu/\nu_c$, ν_c is the critical frequency and

$$F(x) = \frac{\nu}{\nu_c} \int_{\frac{\nu}{\nu_c}}^{\infty} K_{5/3}(\xi) d\xi, \tag{1.40}$$

where $K_{5/3}$ is the modified Bessel function of order 5/3. For a population of electrons with energy distribution between E_1 and E_2, the total integrated power per unit frequency per unit volume may be written as

$$\epsilon = \int_{E_1}^{E_2} P(E) n(E) dE, \tag{1.41}$$

where $n(E)$ is the number of electrons in an infinitesimal window of length dE. Typically, this is distributed in a power-law profile like

$$n(E)dE = kE^{-p}dE. \tag{1.42}$$

Integration of emitted power weighted with this profile produces

$$P \propto \frac{q^3 B \sin\alpha}{p+1}(\frac{m\nu}{qB\sin\alpha})^{(p-1)/2}, \tag{1.43}$$

which implies that the total integrated power will depend on the power-law index $\frac{(\alpha-1)}{2}$. This is important in many astrophysical scenarios, including the radio emission from ultra-relativistic outflows, the optical and radio emission from Crab Nebula.

Non-thermal Comptonization

In presence of relativistic electrons within the plasma cloud, the process of Comptonization also gets modified according to the relativistic scenario. In the thermal case, the photons extract energy from electrons during the scattering event and there is a cut-off in the high energy tail of the spectral energy distribution above a few hundred keV. However, the presence of non-thermal electrons extends the power-law tail beyond this thermal rollover threshold. The tail appears because of the superposition of spectra of individual non-thermal electrons with low optical depth ($\ll 1$).

The seed photons for the Comptonization process may be provided by the Synchrotron events. Therefore, a scenario arises where the Synchrotron photons are up-scattered by the same electrons which are responsible for the generation of those photons in the first place. These up-scattered photons can also contribute to the overall photon energy pull, and this triggers the possibility of multiple self-Compton events.

1.4 Emission States of Black Holes

The black hole binaries (BHBs) exhibit both thermal and non-thermal radiation, both of which are widely variable in intensity patterns. It has long been observed that BHBs transit between different emission states, which are dominated by either of these radiations or one of the radiation components make significant excursions in dominance. Previously, the characterization

of X-ray spectral states almost exclusively relied upon the spectral and temporal properties observable in the X-ray domain. However, presently with the advent of numerous observation capabilities, the X-ray observations are aptly supplemented by radio, IR, and optical studies to provide a more comprehensive picture regarding the emission properties of BHBs.

From the X-ray observation as early as in 1971, the X-ray state change of persistent black hole Cygnus X-1 had been observed, in which the intensity in soft X-ray band decreased by a factor of 4 with the simultaneous increase of hard band intensity (Tananbaum et al., 1972). The brightening of the radio counterpart had also been observed simultaneously. A similar spectral transition had also been pointed out in the case of X-ray novae in the immediate aftermath of this study (Coe et al., 1976). This suggested, for the first time, that some common underlying physical and dynamical phenomena may be at work in both of the cases.

The soft X-ray state is generally associated with high luminosity, prompting the name *high/soft* (HS) state. In this case, the hard power-law tail contributes only a fraction of the total luminosity. In the hard state, on the other hand, the low energy (2-10 keV) flux is considerably low compared to HS state, thereby suggesting the frequent references to *low/hard* (LH) state. The soft state spectrum is best explained by the multi-color black body spectrum (Shakura & Sunyaev, 1973), whereas the LH state spectrum conforms to the power-law profile with a photon index characteristic of that spectrum (Sunyaev & Titarchuk, 1980, 1985).

Many spectral models have been devised so far in order to effectively describe the black hole spectral states. In most of cases, inverse Comptonization and/or Synchrotron emission processes are invoked in order to explain the non-thermal continuum. However, these processes could be applied with a wide variety of geometric variations and fundamental assumptions. In some of the phenomenological models, the two components are allowed to vary independently of each other as well. In order to provide a rudimentary first-order characterization of the spectral properties, the multicolor disk (MCD) model coupled with power-law is often employed, with some additive or multiplicative model if required. In the case of GRS 1915+105, thoroughgoing analysis has been done to completely classify its vast suite of variability patterns and spectral energy distributions. However, before discussing this spectacular source in detail, some discussion regarding the fundamental emission states of normal BHBs is warranted.

Quiescent State

Most of the BHBs spend the majority of their observation span in a state characterized by low luminosity ($\sim 10^{30} - 10^{33}$ erg/s) and occasionally make excursions to states that are few order of magnitudes greater in luminosity. Such transitions are known as outbursts. The predominant low luminosity state marked by a spectrum that is distinctly hard and non-thermal is known as the quiescent state. The quiescent spectra are well fitted by a single power-law coupled with an interstellar absorption model. The power-law index in most of the cases is close to 2 (Kong et al., 2002; McClintock et al. 2003), and the interstellar absorption is determined from the optical extinction. In some of the cases (like in the case of V404 Cyg), the power-law index can go below 2 (Kong et al., 2002).

Thermal Dominated (TD) or High Soft (HS) State

In order to properly understand the BHB observations, one needs to model the hydrodynamic and radiative transfer processes around the black holes. One of the earliest endeavors in this direction was the geometrically thin and optically thin accretion disk, such that every annulus emits black body radiation individually (Pringle & Rees, 1972; Shakura & Sunyaev, 1973; Novikov & Thorne, 1973). The high specific angular momentum of the material released from the companion prevents the material to plunge into the black hole directly, as a result of which it settles down in the form of a disk in the equatorial plane. The outward angular momentum transfer is triggered because of viscous dissipation, which makes the inner disk flow hotter.

Confirmations of this model largely stemmed from the description of the soft x-ray components using MCD model. It is typically observed that below 10 keV the thermal component is predominant. With a few exceptions, the temperature of the innermost part of the disk lies in $0.7-1.5$ keV. The power-law component is faint in these states, as mentioned earlier. Compared to standard BHBs, in the case of GRS 1915+105 and GRO J1655-40, the power-law slope falls more sharply with e-folding energy > 3.5 keV (Sobczak et al., 1999).

The PDS corresponding of HS state shows low variability and falling of power as ν^{-1}, which is a defining signature of many physical processes including turbulence as well (Mandelbrot 1999). The mid-frequency QPOs (0.1-30 Hz) are generally not observed in HS state, although there are exceptions.

QPOs with low integrated RMS ($\sim 0.3\%$) are observed in the TD state of GRO J1655-40 (Remillard et al., 1999) and XTE J1550-564 (Homan et al., 2001).

The LD state is thus characterized by the absence of QPO in 2-30 keV PDS or very weak QPO features (RMS $\ll 1\%$), coupled with the disk flux contributing more than 75% in the unabsorbed 2-20 keV total flux (Sobczak et al., 2000a). The thermal interpretation gets further support from the observed $L \propto T^4$ relationship for constant inner disk radius (Kubota et al., 2001).

In principle, for those sources with well-constrained distance and inclination angle measurements, the inner disk radius could also be measured from the disk normalization parameter $(\frac{R_{\rm in}}{D})^2 \cos\theta$, where $R_{\rm in}$ is the inner disk radius in kilometers, D is the distance of the source in 10 kpc unit and θ is the inclination angle (Arnaud & Dorman, 2002). The MCD model has been further corrected for the radiative transfer through Comptonization by the inclusion of 'spectral hardening factor' (Shimura & Takahara, 1995) and plausible modifications of inner disk emissivity and geometry by way of inclusion of general relativistic effects (Zhang et al., 1997). However, these modifications have their respective limitations (Merloni et al., 2000) and therefore, MCD model is best suited for accessing the inner disk temperature, the consequent spectral state estimation, and the computation of fractional disk flux in the total luminosity only.

Low-Hard (LH) State

Most of the transient sources have been observed to make the transition into low-luminosity, non-thermal spectral state, which can be modeled using a power-law of the slope below ~ 1.7. In some instances, an enhancement of high energy tail (20-100 keV) has also been observed, which has been attributed to the reflection of the power-law component from the inner accretion disk (Di Salvo et al., 2001).

Recently, there has been a significant advancement in our understanding regarding the association of compact and quasi-stable radio jets and hard spectral states. The VLBI radio images have shown quasi-steady radio jets during flat radio spectrum and hard X-ray emission domains of GRS 1915+105 (Dhawan et al., 2000) and Cygnus X-1 (Stirling et al., 2001). It had further been asserted that X-ray sources residing in prolonged periods of spectral hardness are predisposed to show correlated X-ray and radio lumi-

nosities coupled with flat radio spectrum (Fender et al. 1999a; Fender 2001; Klein-Wolt et al., 2002). In the case of GX 339-4, even 2% linear polarization in radio intensity during almost constant inclination angle has also been observed (Corbel et al., 2000). The quenching of radio emission during the transition into the soft state has been also observed routinely (Brocksopp et al., 1999, Corbel et al., 2000).

The exploration of physical properties of the accretion disk in a hard state has been a subject of great deliberation in the interest of gathering a holistic view of the accretion flow. The observation of ASCA in 0.5-9 keV has shown that in hard states of Cygnus X-1 (Takahasi et al., 2001) and GX 339-4 (Wilms et al., 1999), the power-law spectra is coupled with a soft excess which can be modeled by a large accretion disk with ~ 0.1 keV inner disk temperature. The evidence of large and cool disks in the hard state has later been found in other BHBs, including in GRS 1915+105 as well. Using simultaneous observations by HST, EUVE, and Chandra on XTE J1118+480 in its hard state, the inner disk radius and temperatures were determined to be $\geq 100R_g$ and ~ 0.02 keV respectively using the MCD model (McClintock et al., 2001). From BeppoSAX observations, a high temperature of the inner disk has also been reported (Frontera et al., 2003).

Even though it has been demonstrated that the inner disk radius is quite large and the temperature is low In case of the hard state, the physical properties of accretion flow within this truncation radius is still a matter of discussion and there is no consensus among the scientific community regarding this issue. The so-called 'Compton cloud' (Sunyaev & Titarchuk, 1980, 1985) has found different interpretations in the literature from magnetic coronal structure (Galeev et al., 1979) to 'hot gas corona' (Haardt & Maraschi 1993; Zdziarski et al. 2003). However, the Two-Component Advective Flow (TCAF) solution as a natural consequence of transonic flow solutions (Chakrabarti 1990, Chakrabarti & Titarchuk 1995, 1996a, Chakrabarti 1997) has found substantial support in the observational evidence to this day, which will be discussed more elaborately later. Instead of describing the spectra as a combination of blackbody and power-law component, TCAF addresses the entire question of spectral states from the purview of accretion flow parameters like shock location as well as accretion flows with low and high angular momentum. For example, in the case of XTE J1118+480, the same power-law slope could be fitted using the synchrotron model (Markoff et al., 2001) and the thermal Comptonization model (Frontera et al., 2001). However, using TCAF, the entire gamut of spectral states could be described

in terms of the interplay between two types of accretion rates only (Debnath et al. 2014, 2015a,b, 2017; Mondal, Debnath & Chakrabarti 2014; Chatterjee et al. 2016, 2019; Jana et al. 2016a,b; Mondal, Chakrabarti & Debnath 2016; Shang et al. 2019; Banerjee et al. 2020a,b).

In spite of having such a plethora of spectral models, the association of radio jets with the LH state and the LH state characterization and arrival at a possible accretion flow picture is certainly a significant step forward.

Very High (VH) or Steep Power-law (SPL) State

Apart from the LH and HS states, an additional X-ray state is observed in the case of BHBs where the spectrum displays significant luminosity in both disk and power-law component ($> 0.2\ L_{Edd}$), and the appearance of mid-frequency QPOs (0.1-30 Hz) had also been observed in the presence of these components. In this state, the photon index (≥ 2.4) is typically steeper than standard LH states. These characteristics had first been observed in the case of GX 339-4 (Miyamoto & Kitamoto 1991) and X-ray Nova Mus 1991 (Miyamoto et al. 1993). The high brightness was also attributed to the high mass accretion rate (van der Klis 1995).

The distinction between the LH state and VH state had been further strengthened after the OSSE observation (one of four observation capabilities on Compton Gamma Ray Observatory (CGRO) satellite) in 40-500 keV (Grove et al. 1998). It was observed that in a hard state, the spectrum is harder below 100 keV before experiencing an exponential roll-off beyond 100 keV. On the other hand, in the VH state, the spectrum is steeper with photon index > 2.5. This gamma-ray photon index for different spectral states is consistent with the X-ray counterpart.

The extensive RXTE monitoring has revealed that explanation VH state is more involved than originally assessed. In some cases, the X-ray luminosity is smaller than the HS state, but both steep power-law slope and appearance of QPOs are observed (Remillard et al. 2002). However, XTE J1550-564 and GRO J1655-40 show the highest luminosities in this state (Sobczak et al. 1999, 2000b). Thus, steep power-law seems to be quite a legitimate discriminator, while the distinction on the basis of luminosity becomes blurred.

The association of radio properties and SPL state has also been a subject of great enthusiasm. In the case of Cygnus X-1 and GRO J1655-40, the source appears to be radio-quiet as it switches to an SPL state (Tomsick et al. 1999). However, SPL states with powerful bipolar radio jets have also

been reported (Hannikainen et al. 2001). However, it has also been proposed that the X-ray state might have increased in luminosity subsequent to the jet ejection. This conjecture gains support from radio observations where the X-ray spectrum remains in SPL state while the radio luminosity decays below a statistically significant threshold (Corbel et al. 2001). Therefore the evidence available so far imply that the SPL states are in general radio-quiet.

Intermediate State

X-ray spectral states are also observed which combine the features of all of the above states. Therefore, the two basic states can not explain the full range of spectral characteristics.

In the case of hard state spectra which is power-law dominated, the PDS is often found to exhibit a band-limited continuum (a flat continuum in the low-frequency domain that steepens towards higher frequency). Such properties had also been observed in association with strong disk component as well (Mendez & van der Klis 1997). Thus the source state depicts properties of LH state and HS state both.

On the other hand, in the case of XTE J1550-564, the spectral energy distribution and QPO are reminiscent of the SPL state (Sobczak et al. 2000b) but the nature of PDS with band-limited continuum suggests an intermediate state (Homan et al., 2001). The exploration of such PDS is still going on. In such states, the inner disk radius appears to be larger than the TD state but the inner disk temperature appears to be lower. Therefore, it could suggest a linkage between the hard and SPL state. Contemporaneous radio observations are required to further reinforce these conjectures.

However, it has been demonstrated that in case the two-component flow of Chakrabarti & Titarchuk (1995) (CT95) is granted, then the hard and soft states of the black hole candidates, the occurrence of QPOs as well as the properties of nova outbursts can be explained naturally (Chakrabarti 1997). In case of several transient sources it has been demonstrated that the hard and soft intermediate states (HIMS and SIMS) interpolate between standard hard and soft states in terms of accretion flow parameters like accretion rates and shock location (Jana et al. 2016, 2017; Chatterjee et al. 2016; Molla et al. 2016, 2017; Bhattacharjee et al. 2017). This will be discussed later in this Chapter more elaborately.

X-ray states of GRS 1915+105

GRS 1915+105 is a unique X-ray source that shows a wide variety of temporal and spectral variabilities, because of which it has attracted heightened attention of the astrophysics community over the past few decades (Greiner et al. 1996; Belloni et al. 1997a,b). Nevertheless, within this phenomenological complexity, efforts had been made to identify and integrate the spectral and timing features with other X-ray emitters. The extensive RXTE monitoring has revealed that almost half of the observations do not show any structured variability (RMS $< 15\%$ in 2-30 keV). However, in many cases, the variation of ~ 3 Crab is detected within a span of a few hundred seconds as well (Greiner et al. 1996). Among the variable classes, the entire variability patterns had been reduced to the transition between three basic states: A (low time variability, a substantial contribution from the disk to the overall flux), B (dominated by strong thermal component and accompanied by a weak power-law tail) and C (spectra is dominated by strong Comptonized component and 0.5–10.0 Hz QPO is observed) (Belloni et al. 2000). In the case of GRS, the power-law component sometimes extend up to as high as 600 keV (Grove et al. 1998).

Most of the steady intervals show resemblance with either thermal dominated (TD) state or hard state in terms of the spectral characteristics and QPO features (Muno et al. 1999; Fender 2001). However, some noteworthy differences need to be considered while comparing this object with other black hole sources. The energy contained in the ejection events as estimated by Mirabel & Rodríguez (1994) was found to be $> 10^{46}$ erg. Conservative estimation of an injection time-scale of ≤ 3 days yielded the jet power to be $\sim 10^{41}$ erg/s. Fender et al. (1999) further estimated the legitimate lower bound to be 10^{38} erg/s. Such powerful jets are characteristics of GRS 1915+105, which is not normally observed in black hole systems. Further, the X-ray photon index is found to be steeper than usual (~ 2.2), even though it remains flatter compared to the SPL state (≥ 2.4) or power-law tail of thermal dominated state. Therefore, the hard photon index appeared to be shifted upwards.

Overall one can say that the features of GRS 1915+105 can be considered to be at per with X-ray transients if one relaxes the bounds regarding the luminosity and photon index.

1.5 A Short Overview on Accretion Flows around Black Holes

Black holes are unique celestial objects which are devoid of any solid surface and the boundary condition is fixed, i.e. the velocity of a particle on its boundary has to be the same as that of the velocity of light in free space. In case the mass of the stellar core exceeds $3M_{\odot}$, there is no outward pressure generating agency that can resist the collapse of the star after the exhaustion of its nuclear fuel and it collapses into a black hole. As mentioned earlier, black holes are not directly observable because light can not escape from inside a black hole, but the radiation emanating from the diffused matter gathering around the black hole under the influence of gravity can provide substantial evidence regarding the state of matter in its proximity. This is the sole source of power generation of AGNs, quasars, and micro-quasars because non-gravitational energy production mechanisms (like nuclear burning) are much less efficient ($\sim 0.6\%$ only) compared to the gravitational counterpart (around 10%).

The problem of accumulation of matter around the central object had been first studied earlier in 1939 (Hoyle & Lyttleton, 1939). However, no pressure effects had been taken into consideration. Incorporation of the effects of pressure and the exploration of different accretion branches under the purview of spherically symmetry matter accumulation had been first undertaken by Hermann Bondi (1952). The study clearly demonstrated the possibility of transition of the subsonic flow at a large distance to supersonic flow near the surface of the central object. This study paved the pathway for remarkable discoveries in the context of solar physics as well. In order to explain the genesis of the tail of the comets, propositions based on solar wind closely followed the solution provided by Bondi (Parker 1958).

Owing to the development of radio observation facilities subsequent to WWII, the spherically symmetric accretion flow solution had immediately been applied to explain the luminosity of quasars. The first Quasi Stellar Object (QSO or quasar) QSO 3C272 was discovered using radio observations (Hazard, Mackay & Shimmins, 1963), and various propositions WERE immediately offered to explain its luminosity. Soon it was confirmed by Salpeter (1964) that the observed luminosity is explained by a spherically symmetric accretion onto the central object of mass $> 10^7\ M_{\odot}$. The approximate

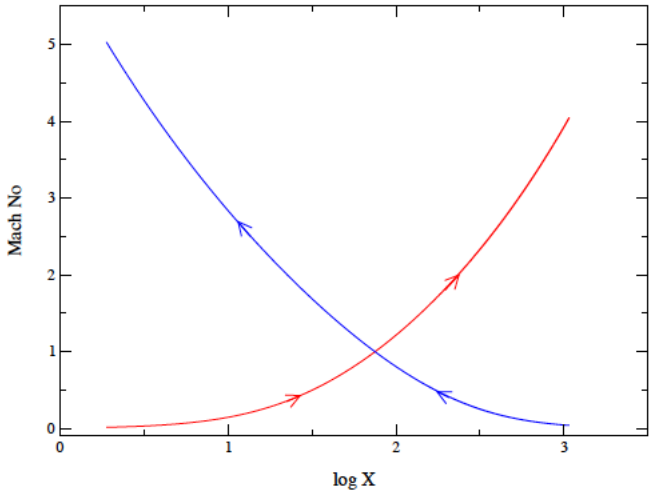

Figure 1.6: The variation of Mach number with radial distance from the central object as proposed by Bondi flow. The blue and red curves are representatives of accretion and wind branches respectively (adopted from Chakrabarti 1990).

time scale of such collapse had also been computed. Further observations on AGNs during this period established QSOs to be only a special case of AGNs.

Bondi accretion flow model was simple enough to be a first-order approximation in the slew of accretion flow models that followed in the subsequent decades. This flow was later found to be unsuccessful for the explanation of the observed quasar luminosity. Therefore, incorporation of the correction factors contributed by other physical parameters like the magnetic field, the compressional heating effects of the collapsing gas, and the plausible modifications due to angular momentum were warranted. The effects of bremsstrahlung radiation was incorporated by Shapiro (1973). Some modifications involving the tangled magnetic fields was carried out by Zeldovich & Novikov (1971) and evidence of synchrotron radiation in the infra-red region was observed. The inner boundary condition was modified to include the changes in accretion flow configuration and radiation pattern in the presence of a solid inner boundary (Shapiro & Salpeter (1975)). Turbulent dissipation was considered as a conversion mechanism from gravitational energy to thermal energy (Meszaros 1975).

For a comprehensive description of accretion flow properties, both hydrodynamics and radiative transfer are important. In this context, the concept of the Eddington rate is quite significant. The Eddington rate is defined by the accretion rate at which the inward gravitational pull on protons is balanced with the outward radiation pressure exerted on the electrons. This provides the upper limit of accretion rate and the corresponding luminosity, assuming 100% radiative efficiency, would be given as

$$L_{Edd} = \frac{4\pi G M m_p c}{\sigma_T} = 1.265 \times 10^{38} (\frac{M}{M_\odot}) \text{ ergs/sec}, \tag{1.44}$$

where m_p is the mass of the proton and σ_T is Thompson scattering cross-section. The energy output from AGNs are typical of this order, and the best-known argument behind such high luminosity is the continuous influx of diffused matter into an extremely massive central object ($\sim 10^6 - 10^9\ M_\odot$). However, with accretion flows with smaller radiative efficiency, this luminosity would be achieved with more accretion rate.

1.5.1 Accretion Disk Models

The wealth of evidence with the advancement of observational facilities gradually revealed that the detailed spectral features and luminosities of QSOs cannot be explained with just radial spherically symmetric accretion flow, and one needs to take the effects of angular momentum and viscosity into consideration. The infall time scale of the radial flow is small because of its low angular momentum, as a result of which even if energy is produced due to dynamical effects, it is mostly advected inwards. With the addition of angular momentum, the infall velocity becomes lower, which allows the viscous processes more time to dissipate energy and angular momentum.

The first comprehensive disk accretion flow model had been proposed by Shakura and Sunyaev (1973; hereafter SS73), which had later been modified for general relativistic corrections as well (Novikov & Thorne 1973). In this model, the modifications due to angular momentum, as well as the effects of viscosity parameters, have been considered in detail. The viscous dissipation between different layers of accretion flow arising out of differential rotation makes the matter rotate in successive Keplerian orbits, such that at each layer the gravitational force equates with the centrifugal force. The viscous torque ($t_{r\phi}$) acting between different layers is responsible for the transportation of

viscosity outwards, which makes the accretion of disk matter possible. However, the turbulent viscosity being of magnetohydrodynamic (MHD) origin, the problem of angular momentum transfer is difficult to tackle analytically, for which a viscosity parameter had been introduced in SS73. The viscous torque had been proposed to be proportional to the vertically averaged local pressure

$$t_{r\phi} = \alpha_{SS} P, \tag{1.45}$$

where α_{SS} is Shakura-Sunyaev viscosity parameter. in general, $\alpha_{SS} < 1$. With the increase of this parameter, the viscous process becomes more efficient in transporting the angular momentum in outer layers. This viscous dissipation makes the accretion flow settle down on the equatorial plane, such that it is geometrically thin ($H(r) \ll r$). The local pressure effects prevent the disk from the vertical gravitational collapse.

The surface density (Σ) can be written in terms of the vertical height and local density as $\Sigma \sim 2H\rho$. The viscous stress tensor is written as

$$t_{r\phi} - \frac{3}{2}\eta\Omega, \tag{1.46}$$

where η is the dynamic viscous coefficient and Ω is the Keplerian angular velocity. The viscous stress in the azimuthal direction is related to the viscous stress tensor as $f_\phi = -t_{r\phi}$. The vertical momentum balance condition in a shick disk system yields

$$\frac{H}{r} \sim \frac{a_s}{v_\phi}, \tag{1.47}$$

where a_s is the sound velocity. From this equation, the vertically thick disk structure implies that the flow is subsonic. The computation of energy dissipation per unit area yields

$$Q(R) = \eta\Sigma^2 R^2 (\frac{d\Omega}{dR})^2, \tag{1.48}$$

where $(\frac{d\Omega}{dR})$ in case of standard Keplerian disk is evaluated as

$$\frac{d\Omega}{dR} = -\frac{3}{2}\frac{\Omega}{R}. \tag{1.49}$$

Substitution of this equation after some algebric rearrangement produces

$$Q(R) = \frac{3GM\dot{M}}{8\pi R^3}[1 - (\frac{R_0}{R})^{\frac{1}{2}}], \tag{1.50}$$

where R_0 is the physical extent of the central object. This equation can be utilized to calculate the total energy emitted between R_1 and R_2 as $\int_{R_1}^{R_2} 2\pi RQ(R)dR$. This calculation produces

$$L(R_1, R_2) = \frac{3GM\dot{M}}{2}[\frac{1}{R1}(1 - \frac{2}{3}(\frac{R_0}{R1})^{1/2}) - \frac{1}{R2}(1 - \frac{2}{3}(\frac{R_0}{R2})^{1/2})]. \tag{1.51}$$

In case of the asymptotic limit of $R_2 \to \infty$ and $R_1 \to R_0$, the total luminosity is obtained as

$$L_{total} = \frac{GM\dot{M}}{2R_0}, \tag{1.52}$$

which implies that half of the accretion energy is emitted as radiation.

The SS73 disk being optically thick, each radial element emits black body radiation with the peak energy

$$T(r) = 5.0 \times 10^7 (\frac{M}{M_\odot})^{-1/2} \dot{M}_{17}^{1/4} r^{-3/4} [1 - \sqrt{6/r}]^{1/4} \text{ K}, \tag{1.53}$$

where M is measured in terms of $M_\odot$, $\dot{M}_{17}$ is in unit of 10^{17} gm/s. Each radial layer of the disk was found to emit disk black body with temperature which scales with radial distance as $r^{-3/4}$. This is the basis of the MCD model mentioned earlier (Mitsuda et al. 1984). In the case of stellar-mass black holes, the inner disk thermal energy peaks around 1 keV while in the case of supermassive black holes excess emission is observed from ultraviolet to soft X-ray band and is formally recognized as the big blue bump (Malkan & Sargent 1982, Sun & Malkan 1989). However, this model suffers from the drawback that it is unable to explain the high energy power-law tail extending beyond 10 keV. It had also been pointed out that in the inner radiation pressure dominated region, the constant viscous coefficient prescription by SS73 would imply the disk might not be stable and break into thin rings (Lightman & Eardley 1974). Single component disk models on the basis of two temperature flow flaring into thick disk-like structures close to the inner edge had also been proposed (Eardley et al. 1976).

1.5.2 Thick Accretion Disk paradigm

The role of the radiation pressure in triggering different kinds of thermal and viscous instabilities and consequent possibilities of thickening of accretion disk had been realized by several workers, which implied the advancement of the thick disk paradigm (Thorne & Price 1975; Eardley, Lightman & Shapiro 1975). The importance of radiation or pressure was taken seriously into consideration. The investigation of steady-state accretion flows with constant angular momentum under a general relativistic framework had been carried out extensively by Lynden-Bell (1978). Under the assumption of constant angular momentum, it was demonstrated that giant vortices could be developed along the axis and the disk can be bloated in the proximity to the black hole. This work had been further advanced and expanded by Paczyński and his collaborators (Kozlowski et al. 1978; Abramowicz et al. 1978) by incorporating different angular momentum combinations. It was shown that thickening of accretion disks can occur in case the inner edge of the disk extends to the marginally bound circular orbit ($\frac{4GM}{c^2}$ in case of Schwarzschild black holes). The pseudo-Newtonian potential constructed by Paczyński and Wiita (1980) was able to explain the thick disk phenomena provided the inner edge lies within the marginally stable circular orbit ($\frac{6GM}{c^2}$). It had further been shown that the accretion rate can exceed the nominal critical rates and this may cause super Eddington luminosity.

The possibility of funnel wall formation had also been associated with the thick disk paradigm, which was met with enthusiasm for its capability in providing a workable framework to understanding the problem of the launching of outflows. However, the thick disk models were not self-consistent because of the consideration of angular momentum distribution on an ad hoc basis. Employing the concept of constant angular momentum surfaces (von-Zeipel cylinders), the first prescription for the angular momentum distribution in a thick disk under a general relativistic framework had been introduced by Chakrabarti (1985). This solution is valid for axisymmetric flows. Subsequently extensive smoothed particle hydrodynamics simulation results demonstrated that shocks are essential for the formation of thick accretion disks, and the shocks are stable for a vast range of flow parameters (Molteni, Lanzafame & Chakrabarti 1994). It was shown that for a large range of energy and angular momentum, the correct thick accretion disk solution occur only in the post-shock region till the inner sonic point close to the black hole. Formation of hot winds which are subsonic close to the disk

surface and gradually becoming supersonic within few tens of Schwarzschild radius were also observed in these simulations.

The thick disk paradigm deserves a separate mention for its role in paving the way for a more comprehensive accretion flow solution including the advection effects. It was gradually being realized that without the inclusion of radial velocity of accretion flows, the scope of accretion flow solutions in describing the observational findings would be limited. Using smoothed particle hydrodynamics (SPH) simulation of inviscid flow, it was observed that accretion mechanism is associated with the formation of normal and oblique shocks for a large range of parameter space and the post-shock region resembles the thick accretion disk. Temperature becomes higher in the post-shock region, and the contours of constant Mach number and dimensionless temperature resemble that of thick accretion disk (Molteni, Lanzafame & Chakrabarti 1994). It was also shown that the post-shock heating generates large pressure gradient force which can push matter away from the accretion plane as well. The centrifugal pressure supported boundary layer (CENBOL; this will be elaborately discussed in the next section) generated in a transonic, advective accretion flow contains most of the features of the thick accretion disk; although in the advective disk paradigm the advection of matter is included self-consistently while in thick disk paradigm advection is totally ignored.

1.5.3 Advective Disk paradigm

Incorporating angular momentum effects, the transonic accretion flow towards a black hole had been studied in great detail in the early '80s (Liang & Thompson 1980, Abramowicz & Zurek 1981, Matsumoto et al. 1984 and Abramowicz 1985). It was shown that a geometrically thin, rotating, adiabatic flow can harbor three sonic points, two of them would be saddle type and one would be center type (Liang & Thompson 1980). Abramowicz and Zurek (1981) had pointed out that with the same specific energy and specific angular momentum, two transonic flow solutions could be possible whose sonic points are different. They also proposed that the disk can oscillate back and forth between two sonic points. It had soon been demonstrated from hydrodynamic solutions for accretion flow in vertical equilibrium that such an oscillating disk would make the entropy to oscillate as well, which makes the solution implausible (Chakrabarti 1989). In the context of the solar wind, the shock formation mechanism in the presence of two saddle type

sonic points is quite well known (Holzer and Axford 1970). In the astrophysical frameworks under the condition of preheating, the possibility of the existence of two such sonic points had been elaborated subsequently (Chang & Ostriker 1985).

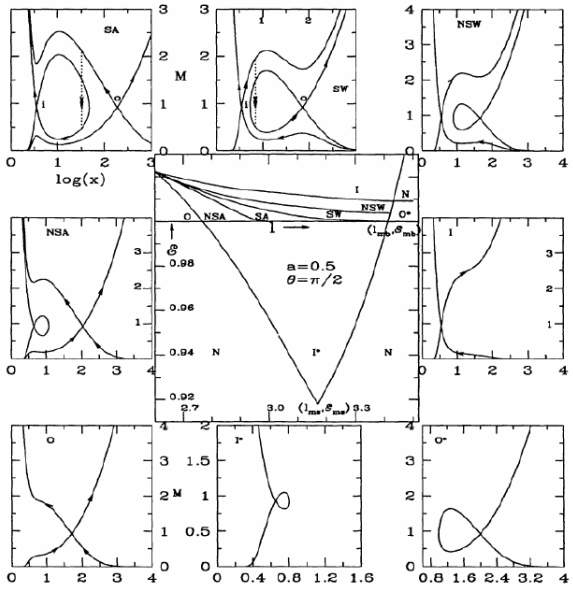

Figure 1.7: Solution topologies for accretion flow around a Kerr black hole. Adopted from Chakrabarti (1996b).

The significant advancement came in 1989 when the global solution of astrophysical flow was proposed by Chakrabarti (1989). Detailed properties of the accretion flows could be understood through a systematic study of hydrodynamic equations involving radial and azimuthal components of velocity. The hydrodynamic solutions were found to be stable. In the context of black hole accretion process, since the accreting matter is bound to be captured within the event horizon, gravitational force finally dominates and makes the flow sink deeper into the potential well even with a constant angular momentum. Different shock solutions (adiabatic, isothermal, or isentropic) emerged as a natural consequence of such hydrodynamic solutions and it was observed that the flow can only enter into the black hole following certain solution topologies. All solution topologies are obtained from the specific energy ($\mathcal{E}$) and angular momentum (λ) values.

In order to understand the accretion flow properties, non-dissipative accretion flow in the context of three different accretion flow geometries (conical model, constant height model, and vertical equilibrium model) had been studied (Chakrabarti 1990). The flow starts with negligible radial velocity in the asymptotic limit ($v \sim 0$) and has to be supersonic before entering into the black hole ($v > a$, a is the velocity of sound). In other words, the Mach number has to be > 1. This makes the flow transonic, which implies that it has to pass through at least one sonic point. Thus close to the black hole the flow sinks rapidly in the potential well, which makes angular momentum almost constant ($\lambda \sim$ constant). The possibility of the existence of multiple sonic points as obtained from the hydrodynamic solutions is that the flow may be slowed down by the centrifugal barrier. In case the barrier is strong enough, the flow may pass through a shock which can heat up the flow in the post-shock region because of energy conversion. The detailed characteristics of the shock depend upon the underlying flow parameters like energy and specific angular momentum. The exploration of the parameter space yielded the fact that the shock solution is stable for a wide range of parameter values (Chakrabarti 1990). The shock could be standing or oscillating depending on the flow parameter.

Extensive investigation on the accretion and wind branches using numerical tools like Smoothed Particle Hydrodynamics (SPH) scheme had been carried out by Chakrabarti & Molteni (1993). It was observed that shock solutions in inviscid flows are extremely stable. It was also concluded that the numerical results agree quite well with the theoretical findings within the limit of numerical accuracy. Both accretion and wind branches had been investigated under the purview of SPH, and it was observed that the outer and inner shock locations are stable for accretion and wind branches respectively.

Two Component Advective Flow (TCAF) solution

Based upon the solutions of hydrodynamic and radiative transfer equations of viscous and inviscid flows around black holes, the Two-Component Advective Flow (TCAF) solution had been formally introduced by Chakrabarti (1995, 1997). To date, it has been found to be the most generalized, fully self-consistent, and quite successful solution to describe the accretion flow around black holes. Recently, it has been successfully applied to understand the spectral and timing properties in the case of neutron stars as well (Bhattacharjee & Chakrabarti 2017, 2019).

It had been proposed that the accreting matter actually comprises of two kinds of accretion flow components: high angular momentum and radiatively efficient Keplerian disk component ($\dot{m}$) as well as the low angular momentum and radiatively inefficient sub-Keplerian halo component. In the case of the isothermal and adiabatic flows, there exists a critical viscosity parameter (α_{cr}), such that the flow with super-critical viscosity forms the disk component. In one-dimensional systems, this had already been verified (Chakrabarti & Molteni 1995). Through extensive numerical simulations, this has been more comprehensively verified by Giri & Chakrabarti (2013). The Keplerian disk component settles down on the equatorial plane and remains submerged within the sub-Keplerian halo. The sub-Keplerian component moves in with the infall time scale, while the radial velocity of the keplerian component is low and it encounters the centrifugal barrier as it gradually sinks in the potential well. The conversion of the kinetic energy to thermal energy produces the CENtrifugal pressure supported BOundary Layer (CENBOL), which is just the reservoir of hot electrons and is optically thin compared to the Keplerian disk. A fraction of the soft seed photons from the disk is captured and reprocessed by this CENBOL region and these upscattered photons constitute the high energy power-law tail. Recently TCAF has been included in HEASARC's spectral analysis software package XSPEC as an additive table model to analyze the spectral properties of accretion flows (Debnath et al. 2014, 2015). A large number of transient sources have been successfully analyzed using this model to derive a holistic picture of accretion flow dynamics around black holes (Debnath et al. 2015a, 2015b, 2017; Chatterjee et al. 2016; Jana et al. 2016; Bhattacharjee et al. 2017; Molla et al. 2017). After obtaining the shape of the observed spectra, the synthetic data is matched exactly with the observed spectra by scaling up or down the simulated spectra using a suitable normalization parameter. In the case of phenomenological models like MCD plus power-law, the normalization comes from only the integrated photon numbers. In the case of TCAF, it is not possible to segregate the contributions from the disk and power-law components, since the integrated effect is obtained from the CENBOL construction. Therefore, the Comptonized component together with the reflection component is embedded in the TCAF code developed in CT95. The information regarding the inner edge of the accretion disk is obtained from the shock location itself, which is the CENBOL boundary as well. The normalization parameter is related to the mass, distance, and the

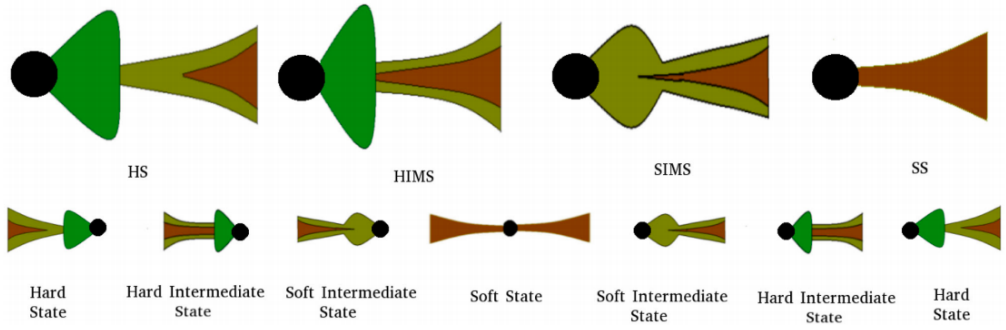

Figure 1.8: A schematic diagram representing the evolution of accretion flow configurations with the changes in spectral states. At the onset of an outburst, shock location remains far away and the halo rate plays the dominant role in the accretion flow. At this point, the source is in Hard State (HS). With the enhancement of the disk component, the cooling of the CENBOL region takes place and the shock location moves inwards. As the disk rate gradually increases, the source traverses from the hard state to the soft state through the intermediate states. Reverse sequence happens as the viscosity at the outer edge of the disk is gradually reduced (adopted from Chakrabarti 2016).

inclination angle of the source through the relation $N \sim \frac{r_s^2}{4\pi D^2}\sin(i)$ (D is the distance in 10 kpc, r_s is the location of the shock front in Schwarzschild unit) (Molla et al. 2016). In the case of the non-precessing accretion disk, the inclination angle should be the same. Further, the mass of the black hole $M \sim T^4$, therefore a small error in temperature measurement would lead to a significant error in mass. Therefore, even though ideally with known mass and inclination parameters the normalization could be uniquely determined, because of practical limitation it is suggested to let it vary within a narrow range only. TCAF has four dynamical input parameters, namely the disk accretion rate ($\dot{m}_d$), the halo rate ($\dot{m}_h$), location of the shock (X_s) and shock compression ratio (R). A resultant spectrum is generated from all these. Recently the generic nature of the solution has been asserted using numerical simulation (Giri & Chakrabarti 2013) as well as through spectral studies (Ghosh et al. 2011).

The cooling of the CENBOL makes the oscillation of the shock front possible. In case the cooling time scale is roughly within 50% of the infall time scale from the shock location, the resonance condition is satisfied and

the CENBOL region starts to oscillate which is observed as a sharp peak in PDS (Molteni, Sponholz & Chakrabarti 1996; Chakrabarti & Manickam 2000; Chakrabarti, Mondal & Debnath 2015). This mechanism explains the appearance of QPOs in the case of black hole sources as obtained in observational findings. With the increase in disk accretion rate, CENBOL cools down more rapidly and shrinks its size, which makes the QPO frequency shift towards a higher frequency domain. This is known to be the rising phase of the outburst. The QPO frequency is inversely proportional to the infall time scale. In terms of shock location, it is expressed as

$$\nu_{qpo} = \frac{\nu_{s0}}{t_{infall}} = \frac{c^3}{2GM}\frac{1}{RX_s(X_s-1)}, \tag{1.54}$$

where R is the compression ratio (Chakrabarti et al. 2008; Debnath et al. 2010, 2013; Nandi et al. 2012).

Jets and outflows can also be incorporated in a consistent manner in the TCAF framework. It had been proposed that in case the CENBOL contains enough hot electrons in hard and hard intermediate states, outflows can be generated from this region (Chakrabarti 1999a; Das & Chakrabarti 1999). As a source makes the transition from a hard state to a hard intermediate state, generally the inflow rate increases as well. With this enhancement of inflow rate, the outflow rate can also shot up (Chakrabarti 1999b). In general, two kinds of outflows are observed: continuous outflows or compact jets and discrete ejections or blobby jets (Chakrabarti & Nandi 2000). Jets move subsonically up to the sonic points, but beyond the sonic point they become supersonic. This process makes the outflow emit in UV, IR, and radio domain (Chakrabarti 1999a, 1999b; Chakrabarti & Manickam 2000). Within the sonic sphere, the outflow base is cooled down episodically and a fraction of the outflowing matter collapses on the accreting matter. This local feedback mechanism between the inflow and the outflow modulates the accretion flow in quick succession. In softer states, the soft photon supply is enhanced due to an increase of the disk rate and the outflow may be quenched (see also Garain et al. 2013). Collimation of the outflow can also be contributed by the toroidal flux tubes from convective disks (Chakrabarti & D'Silva 1994; D'Silva & Chakrabarti 1994). Recently, the photons coming from CENBOL and the outflow base have been separated and the fraction of the total flux contributed by the jet has been computed using the TCAF paradigm (Jana et al. 2017). We have used this accretion-ejection mechanism to explain the

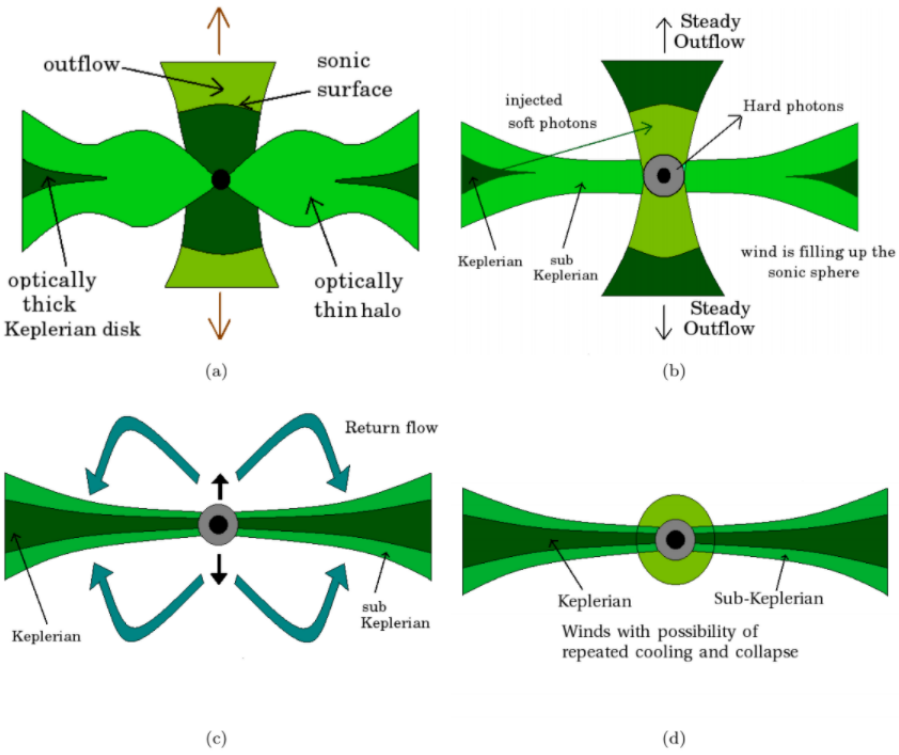

Figure 1.9: The disk-jet interaction and the consequent changes in the accretion flow configurations are depicted in Figure 1(a-d). (a) Halo rate dominating. RH condition not satisfied, hence there is no shock. The inner region is puffed up. (b) The shock produced due to satisfaction of RH condition. Outflow generated and a steady outflow rate is maintained because the average optical depth within the sonic sphere is smaller than 1. (c) The region within the sonic sphere cooled down and a fraction of outflow falling back on the initial accreting matter. The outflow beyond the sonic sphere ejecting as blobs. (d) After the draining out of excess matter, the shock reverts back to the original position and the whole process starts afresh (adopted from Chakrabarti et al., 2000).

observations in the context of class variable source GRS 1915+105, which will be discussed in detail in Chapters 3 and 4.

The ratio of outflow rate to the inflow rate had been found to be a function

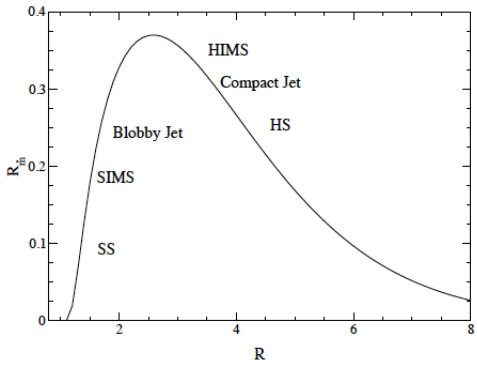

Figure 1.10: The variation of $R_{\dot{m}}$ with the shock strength. In intermediate shock strength, the outflow rate is maximum. Figure is adopted from Chakrabarti, 1999a.

of the shock strength (R) (Chakrabarti 1999a). The relation reads as

$$R_{\dot{m}} = \frac{\theta_{out}}{\theta_{in}} \frac{R}{4} \left(\frac{R}{R^2-1}\right)^{3/2} \exp\left(\frac{3}{2} - \frac{R^2}{R-1}\right), \tag{1.55}$$

where θ_{in} and θ_{out} are the opening angles subtended by the inflowing and outflowing matters respectively. The outflow rate was found to be highest for moderate shock strength.

1.6 Complexity in GRS 1915+105

As mentioned earlier, GRS 1915+105 has continuously enthused the astrophysics community owing to its rich X-ray intensity morphology. Intensity changes by the factor of a few within a span of few tens of seconds and the recurrence of such behaviors over hundreds of seconds to days have made this source quite distinct from the standard X-ray sources. Based upon the standard hardness ratio and conventional color-color diagram, the X-ray variability of the source had been sub-categorized into 12 distinct variability classes: namely α, β, γ, δ, ϕ, ν, θ, λ, κ, ρ and χ (Belloni et al. 2000). Across these different classes and even within each category, the duration and the behaviour of the 'On' (high photon intensity) and 'Off' states vary quite substantially. For example, in case of ρ class extremely regular variability of extended Off state is observed (Taam, Chen & Swank 1997), while in ν class

the variability is highly irregular. On the basis of black hole accretion flow paradigm, however, these suite of variability classes had been organized and classified into four basic spectral states: Hard, Soft, Semi-Soft and Intermediate (Nandi, Manickam & Chakrabarti 2000a). In case of χ variability class, the source is devoid of any strong variability and the photon count remains quasi steady. Depending upon the color-color diagram, the presence/absence of QPOs and the signature of contemporaneous radio emission, χ class is further sub-divided into four sub-classes: χ_1, χ_2, χ_3 and χ_4 (Belloni et al., 2000). The χ_1, χ_3, β and θ classes are found to be associated with strong radio ejections (Naik & Rao, 2000; Vadawale et al., 2003).

Attempts have been made to model such variations by assuming the persistent flux level to be of the same order as that of low hard state ($L_{bol}/L_{Edd} \sim 0.05 - 0.2$) and spectra at the peak flux level to be statistically the same as that of high soft state ($L_{bol}/L_{Edd} \sim 0.7 - 1.2$) (Vierdayanti, Mineshige & Ueda 2010). People have attempted to model the energy spectra at both flux levels with disk blackbody (including non-zero torque condition as well) and power-law (Nobili et al. 2000; Trudolyubov 2001; Klein-Wolt et al. 2002; Fuchs et al. 2003; Rodriguez et al. 2004; Martocchia et al. 2006; Ueda et al. 2009). Thermal Comptonization of seed photons in the presence of a strong non-thermal component corresponding to the power-law tail has also gained ground in spectral modeling using simultaneous observation of RXTE (Done et al. 2004; Pahari & Pal 2010) and OSSE/CGRO observations (Zdziarski et al. 2001; Rau & Greiner 2003) as well as BeppoSAX observations (Mineo et al. 2012). It had further been pointed out, the spectra of GRS 1915+105 resembling HS state is inherently complex, and cannot be adequately modeled by multicolor disk blackbody alone (Sobolewska & Zýski, 2003).

Some of the earlier attempts with limited success had focused on modifying the standard Keplerian disk solution for radiation pressure effects near the inner edge. In the steady-state, the temperature of the standard accretion disk varies with radial distance as $T(r) \sim r^{-3/4}$. This exponent has later been allowed to be a free parameter ($T(r) \sim r^{-p}$), which has been included in *XSPEC* as `diskpbb` model (Mineshige et al. 1994; Watarai et al. 2000; Kubota et al. 2005). They had argued that in case the luminosity of the source exceeds $\sim 30\%$ of Eddington luminosity, the inner disk region grows thicker due to the radiation pressure effect and the advection effect in the inner edge contributes to the cooling of the disk. In such cases, the exponent (p) becomes ~ 0.5. The local effective temperature is reduced by a factor of f, which had been considered to be a constant irrespective of the radial

distance (Shimura & Takahara 1995). However, assuming a Compton cloud away from the disk plane, people had proposed that this factor may have a radial dependence as well.

The analysis of spectral variation using RXTE/PCA data revealed that the observed phenomenological variations could be a result of rapid evacuation and subsequent slow replenishment of the inner accretion disk region (Belloni et al. 1997b) prompted by thermal-viscous instability. Subsequently, the notion of various instability parameters (including radiation pressure-driven instability) as the primary cause of the observed variabilities became acceptable. The inflation of the inner edge of the standard disk because of radiation pressure effect and consequent instability (Nayakshin, Rappaport & Melia 2000) as well as the stochastic variations of the viscosity parameters (Watarai et al. 2000) had been applied and some observed variations could be explained. However, the crucial question remained unanswered: if the instabilities are the primary agency behind the large amplitude intensity variations, then why this phenomenon is so apparent only in the case of GRS 1915+105 but remains unobserved in standard X-ray binaries?

The results of the numerical simulation of radiation pressure dominated disk were found to be at variance with the observed variability features (Janiuk & Czerny 2005). Modifying the viscosity prescription to include the effects of energy dissipation in the corona and a luminosity dependent energy deposition in the jet, the order of magnitude intensity variations detected in κ and λ classes could be reproduced (Nayakshin et al. 2000). Janiuk, Czerny & Siemiginowska (2000) showed that the time-dependent behavior of GRS can be well reproduced if the earlier modifications in standard α prescription are incorporated.

In spite of all such initiatives of providing a qualitative picture targeting to reproducing observed variabilities, a comprehensive understanding of the accretion flow responsible for all such spectral and temporal variabilities remained wanting. It was crucial to understanding whether the flux variation is a consequence of the appearance and expulsion of one spectral component, or the spectral evolution that happens as a result of low state to a high state transition. One important point to note is that notwithstanding efforts in incorporating radiation pressure and instability effects in standard disk configuration and initiatives in modifying the standard viscosity prescription, the central notion of disk component to be the sole contributor to the accretion flow was being challenged. Efforts were being made to incorporate the behaviour of magnetic flux tubes embedded in the disk and their possible

contribution on the jet formation and micro-variability. Chakrabarti & Di Silva (1994) had shown that over a large range of the angular momentum distribution as well as the size and strength of the flux tubes, the axisymmetric and toroidal magnetic flux tubes can gather in the chimney (vortex like opening region formed on either side of radiation or ion-pressure dominated disk, where the continuously ejected matter is collimated), making the chimney magnetically active. This explains the expulsion of flux tubes from adiabatic thick accretion disks. Subsequently, it was also demonstrated that in the case of isothermal or radiative disks, weaker flux tubes oscillate around equipotential surface dictated by gravitational force and centrifugal force; but are not expelled away. Once their strengths are amplified by shear, they become more buoyant and are eventually expelled away (Di Silva & Chakrabarti 1994). In hot plasma (temperature $\geq 10^{10}$K) the collapse of magnetic flux tubes under magnetic tension force would be the dominant phenomena and this would eject the hot disk matter transverse to the disk plane (Nandi et al. 2001). Such evacuation of disk matter can explain the launching of 'baby jets' reported earlier (Mirabel et al. 1998). The estimated mass contained in the post-shock region (10^{18}) was found to be one order of magnitude smaller compared to the earlier estimation of mass contained in the baby jets (Mirabel et al. 1998). This observation implies that the sub-Keplerian component could also contribute to the ejected matter, which is commensurate with the analytical solution of mass outflow provided by Chakrabarti & Bhaskaran (1992). This qualitative picture requires the evacuation of the Comptonizing region during soft X-ray dips as proposed by Vadawale et al. (2001, 2003).

Thus, the importance of two kinds of accretion flow components (Keplerian and sub-Keplerian) in the context of rich structured morphological features of GRS 1915+105 has found recognition in the literature. However, the numerical values of the accretion flow components corresponding to different stages of variabilities have not been extracted in a systematic way.

1.7 IGR J17091-3624: Another Source of Rich Structural Variability

Previously, one problem of proper understanding of the spectro-temporal behaviour of GRS 1915+105 was the non-availability of another source with similar variability properties. Another question seems to be quite pertaining:

why such rich structured variability features are detected so far only in the case of GRS 1915+105, but remains undetected in any other almost no other transient or persistent black hole X-ray binaries? Subsequently, in the case of another Galactic X-ray emitting black hole candidate IGR J17091–3624 discovered with *INTEGRAL*/IBIS in 2003, similar rich variability patterns like GRS 1915+105 was detected (Kuulkers et al. 2003). Extensive investigation by a slew of X-ray missions confirmed that IGR J17091–3624 was active in 1994, 1996, 2001, 2003, 2007 and 2011 (Revnivtsev et al. 2003; Capitanio et al. 2006, Krimm et al. 2011). The 2011 outburst of this source showed recurrent, large-amplitude intensity oscillations in the lightcurves similar to GRS 1915+105 (Altamirano et al. 2011a,b,c,d; Pahari et al. 2011). Following the criteria of defining the variability classes corresponding to GRS 1915+105 (Belloni et al. 2000), Altamirano et al. (2011d) identified α, β, μ, ν, ρ and λ classes in the case of IGR J17091-3624 as well. Extended periods of non-variability typical of χ classes of GRS 1915+105 had also been detected. Some unique variability classes had also been reported in the case of IGR J17091-3624, which had never been observed in the case of GRS 1915+105 (Pahari et al. 2012). LFQPOs, as well as mHz and high-frequency QPOs (HFQPOs) had been detected during Rossi X-ray Timing Explorer (RXTE) mission (Rodriguez et al., 2011, Altamirano et al., 2011c,d; Altamirano & Belloni, 2012). The discovery of a second source with similar phenomenological characteristics as that of GRS 1915+105 provides a unique opportunity to test the models used to understand the spectro-temporal behaviors of GRS 1915+105.

Despite similar variability characteristics of these two sources, IGR J17091-3624 is observed to be 10-50 times fainter compared to GRS 1915+105. Assuming the variability patterns as a consequence of near Eddington limit emission, this mismatch of intensity had been attributed to either IGR J1709-3624 hosting a small black hole ($< 3\ M_{\odot}$), or residing in more than 17-20 kpc away (Altamirano et al. 2011a). However, results from other multi-wavelength investigations are at variance with these conclusions. Contemporaneous multi-wavelength campaigns implied that the source distance lies between 11 kpc and 17 kpc (Rodriguez et al. 2011). Employing the photon index (Γ)-QPO frequency (ν) correlation method as well as broadband spectral fitting using Two-Component Advective Flow (TCAF), the mass of IGR J17091-3624 had been inferred to be in the range of $8.7\ M_{\odot} - 15.6\ M_{\odot}$ with 90% confidence level (Iyer, Nandi & Mandal 2015). Alternative scenarios like high inclination angle of the disk plane ($i > 53^{\circ}$) and low black hole spin

were proposed to explain the observed faintness (Capitanio et al. 2012; Rao & Vadawale 2012). In the absence of direct measurement of the fundamental physical parameters of IGR J17091-3624, all the source parameters like mass, inclination angle and spin remain poorly constrained and the physical origin of the timing behavior of this source and its parallel with GRS 1915+105 is still debated.

1.8 Objective of the Thesis

In this thesis, we focus on the following theme:

- First, we focus on the sub-classes ($\chi_1 - \chi_4$) which are devoid of any structured variability, and the photon intensity across the evolution of those sub-classes remain almost constant within the statistical limit. However, some of these sub-classes are associated with simultaneous radio observations (radio plateau states), while in case of the other sub-classes no simultaneous radio observation has been detected. These sub-classes are also widely varying the detected flux levels. We have attempted to understand whether there is some systematic difference between such classes with different luminosities and different contemporaneous radio counterparts in terms of the accretion flow behavior, and whether that can be connected to the accretion flow features of standard black hole X-ray binaries.

- We have also focused our attention to understand the behavior of additional spectral components which might be responsible for the relative changes of the radio counterparts across the relevant sub-classes. In particular, the relative contribution of TCAF and the additional spectral components to fit the high energy tail is an interesting aspect to get a complete understanding of the accretion-ejection behavior of the source.

- We have also ventured into investigating the features of power spectrum across different sub-classes and QPO behavior. The characteristics of broadband noise and peaked components of these sub-classes provide important information regarding inner regions of the accretion flow.

- Subsequently, we have attempted to analyze the θ class data using Indian satellite AstroSat. The source is highly variable in this class such

that the photon intensity changes by a factor of 3-4 within an interval of a few hundred seconds. The class is characterized by recurrent dips with pre-dip short duration flares. The intensity variation happens in a much shorter time-scale compared to the standard BHBs. We examined the variations of QPO feature during the rising and declining branches to understand the temporal variation of the source. It is also interesting to investigate how correlated is the QPO features with intensity variations.

- We extract the accretion flow parameters after fitting the spectra using TCAF. This becomes important to correlate the accretion flow parameters and the evolution of the source. In this way we are providing a plausible flow configuration and evolution mechanism that explains the observed spectro-temporal features.

- Finally, we attempt to undertake a case study to compare the spectral and temporal features of GRS 1915+105 and IGR J17091-3624 and provide a plausible underlying accretion flow mechanism that explains the observed variabilities of both of these sources. We show that once the presence of two accretion flow components is granted, there is a way of explaining the variability properties as a consequence of the interplay between the flow components. This opens up the pathway of a larger program of undertaking extensive wide band spectro-temporal analysis and making comparative studies for all the major variability classes detected in these two sources and understanding the holistic accretion flow picture that such a study reveals.

Chapter 2

Data Analysis and Observation Tools

2.1 Introduction

All the results and conclusions presented in the thesis are based upon the analysis of the archival data obtained from Rossi X-ray Timing Explorer (RXTE) and Large Area X-ray Proportional Counter (LAXPC), AstroSat. For spectral analysis purposes, X-ray spectral fitting package `XSpec` has been utilized. In this chapter, we will present a brief discussion of all these facilities.

2.2 Data acquisition from X-ray Missions

2.2.1 Rossi X-ray Timing Explorer (RXTE)

NASA's astronomy project Rossi X-ray Timing Explorer (RXTE) was launched from Kennedy Space Center on December 30, 1995. It was active for 16 years before it was decommissioned in 2012. The entire mission was monitored and controlled by NASA's Goddard Space Flight Center (GSFC). The principal objective of the mission was to observe the brightest sources in the sky such as the X-ray binaries, AGNs as well as Ultra Luminous X-ray sources (ULXs). The unprecedented detector specifications were particularly a characteristic feature of RXTE. The unique microsecond timing resolution coupled with broad energy coverage over 2-200 keV enabled the scientific community to

explore detailed geometrical features in relation to the accretion flows around the compact objects, as well as their physical characteristics (such as mass, spin, magnetic field, etc).

The mission is driven by two pointed onboard instruments: Proportional Counter Array (PCA) which covers the lower energy domain (2 - 60 keV) (Jahoda et al., 1996), and the High Energy X-ray Timing Experiment (HEXTE) which covers the upper segment of the energy domain (15 - 200 keV) (Rothschild et al., 1998). In addition, the onboard All-Sky Monitor (ASM) instrument operates in 1.5 - 12 keV and scans around 80% of the sky in each satellite orbit (Levine et al., 1996). We provide a short description of the exclusive capabilities and scopes of each of these instruments below.

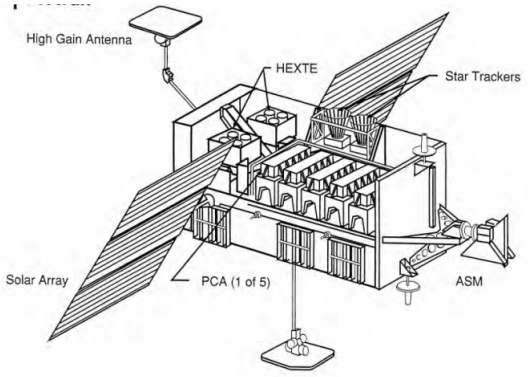

Figure 2.1: Schematic diagram of RXTE. Photo courtesy: NASA.

All-Sky Monitor (ASM)

The ASM instrument is equipped with three Scanning Shadow Cameras (SSC), each of which contains a position-sensitive proportional counter (PSPC) to perceive the sky through a slit mask. The source intensities and directions are inferred from the movements and depths of the shadow patterns produced by the sources within the Field of View (FOV). Each partition of PSPC is associated with $6^\circ \times 90^\circ$ FOV. The total photon collection area of all these PSPCs is 90 cm^2. The Spatial resolution is $3' \times 15'$, with the total detection efficiency of 20 mCrab.

The on-board Event Analyzers (EAs) in the Experiment Data System (EDS) compress the event mode data recorded by ASM and the scientifically

processed data is then fed into the telemetry system. The ASM EA mechanism bins the counts as a function of position and such counts of 90 seconds exposure are recorded in 'dwell' mode. Corresponding to every dwell, the SSC orientation is kept fixed. The final histogram thus encapsulates the complete superposition of all the shadow patterns corresponding to each and every source lying within the FOV.

ASM also provides the unequally sampled event mode data of 0.125 second time resolution, daily averaged over a number of dwells. The source intensity database (light curves) for different 'colors' enables the observer to study the source variation across different energy bands. The background events of 1 second time resolution are also stored in a separate file.

This quick scan and record capability of ASM has proved itself to be extremely useful in new source detection, monitoring the intensity variation over a long period of time and detect state changes of previously detected sources. Photon collection in different energy bands also enables to compute the time lag of different accretion flow components and predict the outburst phenomena of transient sources using the variation of dynamic photon index (Ghosh & Chakrabarti, 2018).

Proportional Counter Array (PCA)

The PCA detector consists of five identically prepared and co-aligned Proportional Counter Units (PCU) with a geometric photon collection area of 1600 cm^2 apiece. Each of these detectors is facilitated with a mechanical collimator with FWHM $\sim 1^\circ$. The events are detected in the Xenon-filled active volume of the detectors and are passed on to the Analog to Digital (AD) converter. There is also propane filled 'veto' volume that tracks the background events. Signals captured in 'veto' layers are not recorded through AD converters but are rather transferred to EDS to be recorded as a pulse height. In the case of 'good' X-ray events, i.e. the genuine events from the source trigger only one discriminator bit of EDS, and the pulse height can be unambiguously associated with the source signal. In the case of coincident events, there is ambiguity regarding the digitization of signals and such events are typically not recorded.

The PCA detector facilitates observation of sources producing fluxes ranging up to 20000 counts/s/PCU unit. The combination of instrumental and operational specifications made PCA sensitivity quite strong to the time variability of Galactic compact objects and AGNs. Notable instrumental char-

acteristics were large photon collection area, microsecond time resolution of photon detection and efficient background detection. The key distinguishable operational features were swift rocking of the mounted collection unit, flexible observation planning, and accessibility of wide celestial sphere beyond 30° of the Sun. We have used RXTE PCA data for the analysis of the χ class data of GRS 1915+105 (Chapter 3).

High Energy X-ray Timing Experiment (HEXTE)

HEXTE contains two independent detector clusters, each consisting of four collimated NaI(Tl)/CsI(Na) phoswich scintillation counters. The co-alignment of all the collimators offers a 1° FOV corresponding to each cluster. The combined photon detection area is 1600 cm^2 with detection capacity in 15 - 200 keV. The average energy resolution at 60 keV is $\sim$ 15%. The cluster organization filters systematic background variation via gain control mechanism, splitting of the source signal, and anticoincidence shielding.

However, the nominal photon count rate of HEXTE is only 289 counts/s for crab and the photon detection sensitivity is low (1 Crab = 360 count/s per HEXTE cluster). Compared to background event register sensitivity (50 count/s per HEXTE cluster), this is not high enough. This causes a larger systematic error in the high energy domain compared to PCA and puts a limitation on spectral and timing studies using HEXTE. Owing to these reasons, we have not used HEXTE data for any of our analyses.

Data Mode and Screening Criteria

The comprehensive and carefully maintained RXTE public data archive has provided a great opportunity to the astrophysics community all over the world to download, process, analyze the raw data of numerous X-ray emitting sources of various kinds and draw inferences. Over 250,000 individual observations are registered in this public archive. In order to make the data mining process straightforward as well as facilitate swift and efficient data analysis capacity, RXTE Guest Observer Facility (GOF) has made available the standard data products (StdProds) corresponding to every individual observation of RXTE, alongside the data product files. High-level products like source and background intensity variations, spectral variabilities, flares, and brightness transitions, spectral hardness are produced from raw data files using the `StdProd` files.

Raw science data is stored in two basic formats: *science array* and *science event*. Different data modes and configurations of PCA and HEXTE are together described to the underlying software through configuration describing strings in Data Descriptor Language (DDL). RXTE filter files are separately provided to obtain 'good' science data on the basis of various housekeeping data.

The *science array* format bins data in equal intervals of time. For example, PCA Standard 2 configuration accumulates data every 16 seconds for all 129 channels. The `XTE_SA` extension of science array files contains science data in matrix form, where each row contains data corresponding to each accumulation and each column contains data histogram of photon counts in different channels. Separate keywords in the data header contain information regarding the data mode, the name of the corresponding data gathering instrument, start and end time of data collection, the bin size as well as some instrument specifications.

In the case of *science event* data, on the other hand, register individual time-stamped events for all the channels and PCU IDs, but the data remains unbinned. The data is recorded in two columns. The first column registers the time instances and the second 'event' column records strings of ones and zeros (event words) which represent the event characteristics with respect to the pre-defined templates. Like science array files, separate keywords contain details of data attributes here as well. The data is transmitted to the processing unit as unevenly spaced data points unbinned data blocks.

While analyzing science data, it is important to filter the unwanted data from the raw science files. In order to facilitate that, RXTE science array files contain Good Time Interval (GTI) extensions and specific GTI files that contain GTI corresponding to good data acquisition periods as dictated by suitable and appropriate data filtration criteria. The filtration includes the screening of data below a particular elevation angle (usually below 10 degrees) to avoid the Earth occultation effects, filtration of data beyond recommended offset level (usually above 0.02) to avoid instrument rocking motion and initial spikes, screening of events during the South Atlantic Anomaly (SAA) passage as well as the filtration of unwanted electron contamination. In order to select the good data, specific filter files are provided which contain various housekeeping data and relevant derived quantities. In case requisite information are not there in the filter files, the curated ones could be generated by the user using the built-in *xtefilt* command. The filter file is then provided as input to the *maketime* task which creat the curated GTI file by

assembling the appropriate subsets of time from the housekeeping file.

2.2.2 AstroSat

AstroSat is the first Indian satellite targeted specifically towards comprehensively observing celestial sources in Ultra-Violet (UV), X-ray, and optical band. Five co-aligned scientific payloads Scanning Sky Monitor (SSM), UV Imaging Telescope (UVIT), Soft X-ray Telescope (SXT), Large Area X-ray Proportional Counter (LAXPC), and Cadmium Zinc Telluride Imager (CZTI) enable the observer to study astronomical targets across all wavelengths simultaneously. It was sent into its orbit on September 28, 2015, using PSLV-C30. The orbit has an inclination angle of 6 degrees. The science data gathered using all the science payloads are transmitted to the spacecraft control centre at the Mission Operations Complex (MOX) of ISRO. After processing and properly organizing, the data is archived at the Indian Space Science Data Centre (ISSDC), Bengaluru. The minimum life span of operation of AstroSat was estimated to be five years.

We provide a brief description of all these payloads below.

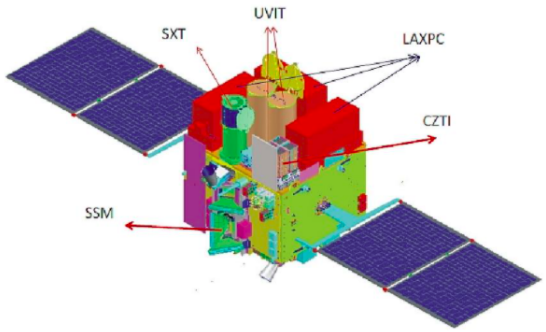

Figure 2.2: Schematic diagram of AstroSat. Photo courtesy: ISRO.

Scanning Sky Monitor (SSM)

The principal scientific objective of SSM is to detect new cosmic transient sources as well as to observe the intensity variations in cataloged X-ray sources. The operational domain of this instrument is 2.5 keV - 10 keV. SSM monitors and searches for Galactic and extra-Galactic X-ray sources in

the designated energy band with the three mounted on-board cameras. SSM is equipped with three position-sensitive proportional counters, each with one-dimensional coded mass. It has a built-in alert generation mechanism for the detection of fresh cosmic sources as well as flux variation of known sources. These alerts are then transmitted to the ground-based observatories for follow-up strategies. This instrument is similar to ASM in RXTE in its construction and operation.

Large Area X-ray Proportional Counter (LAXPC)

LAXPC is a major payload in AstroSat design which accumulates X-ray data in 3-80 keV from detected cosmic X-ray sources. It consists of three identical detectors with combined effective area of 6000 cm^2 in 5-20 keV. The total X-ray detection volumn is 100cm $\times$ 36cm $\times$ 15cm. The LAXPC detectors are labelled as LAXPC10, LAXPC20, LAXPC30, all of which can operate independently and record the independent event with a remarkable time resolution of 10 μs. Each of these detectors contains 5 anode layers, each of which contains 12 anode cells of size 100 $\times$ 3 $\times$ 3 cm. The two top layers are further sub-divided into two sub-layers, in each of which alternative cells are connected, providing 7 main anode layers in total. Along with these main anodes, three veto detectors are associated to catch the background. The processing electronics are designed in such a way as to reject any event that triggers any of these veto anodes, or trigger more than one main anode, or deposited more than 80 keV in any of these anodes. This procedure was found to be effective in filtering the background with 99% accuracy.

The increased pressure and depth of the LAXPC detectors facilitate higher effective area at high energies ($>$ 30 keV); but at the same time, it leads to the increased background, making it problematic to study faint sources. In our analysis, we have used LAXPC10 data for spectral and timing studies (chapter 4). We provide details of data downloading and analysis of LAXPC data later in this chapter.

Cadmium Zinc Telluride Imager (CZTI)

AstroSat CZTI is a hard X-ray imager operative within 10-150 keV, consisting of Pixellated Cadmium-Zinc-Telluride detector array with geometric photon collection area $\sim$ 1000 cm^2 (Vadawale et al. 2016; Bhalerao et al. 2017). CZTI provides excellent detection efficiency ($\sim$ 100% in high energy)

and high energy resolution ($\sim$ 2% at 60 keV) compared to standard proportional counters. The overall field of view of CZTI as defined by the collimator is $6^\circ \times 6^\circ$ in 10-100 keV. During the CZTI performance characterization in the first six months of launching, it was observed that CZTI is highly sensitive to particle showers because of improved pixel density. This results in higher data volume with many spurious events unsuitable for carrying out the core scientific objectives of CZTI. The remedial mechanism has been implemented in the on-board data products generating software as well as high-level data processing pipeline.

Ultra Violet Imaging Telescope (UVIT)

The operative frequency domain of UVIT is UV and optical (Subramaniam et al. 2016). UVIT contains two distinct telescopes. One of them operates in optical (320-550 nm) and Near UV (NUV) wavebands (200-300 nm). The other one operates in the Far UV (FUV) waveband (130-180 nm). The spatial resolution of UVIT is 1.8 arcseconds and the field of view is 0.5 degrees. The photon-counting detectors can measure the location and time of incidence of individual photons. Since targets are fainter in UV compared to visible, the UV signals are amplified before reading out using 'intensified CMOS' readout cameras. UVIT can image the total field of view with a frequency of 30/seconds. The photon capturing CMOS detector registers photons by producing charge equivalents corresponding to incoming photons. This makes the UVIT interior vulnerable to bright radiation. Sunlight scattered from bright satellite surface reflected glow from Earth surface, emission from excited molecules from Earth's outer atmosphere can threaten the sensitivity and even stability of UVIT. Therefore UVIT operates only at night, with proper protective shielding and electronics.

Soft X-ray Telescope (SXT)

AstroSat SXT conducts X-ray imaging in 0.3-8.0 keV (Singh et al. 2016). Nested mirror foils are installed to enhance the effective photon collection area of SXT. The collimated photons are finally registered by a cooled charge-coupled device (CCD) with 600×600 pixel array. The CCD detectors are cooled in order to filter stray noises. The spectral resolution of SXT is 150 eV at 6 keV. Total effective area of SXT is 120 cm^2. The focal plane of

onboard CCD detectors of SXT are structurally and operationally similar to Swift/XRT.

AstroSat LAXPC Data Acquisition and Usage

LAXPC detectors gather data through two basic modalities: Event Analysis (EA) mode and the Fast Counter (FC) mode. In EA mode, the timestamp of each event is recorded along with their channel and anode information. Each event is registered as 5 bytes of data. The estimated deadtime of the detector is 42 μs. EA mode also generates a Broad-Band Counting (BBC) mode which registers intensities in 3–6 keV, 6– 18 keV, 18–40 keV, and 40–80 keV energy bands. BBC mode also contains the counts for rejected events.

In FC mode, counts from only the top anode layer in 160 μs time window are accumulated in 3–6 keV, 6–8 keV, 8–12 keV, and 12–20 keV energy bins. The dead time of FC mode is higher compared to EA mode (10 μs) and this makes FC mode suitable for bright sources.

The stability check of the detectors is performed periodically to check for drift in the channel to energy mapping with the passage of time. Due to abnormal gain changes in the LAXPC30 unit, that particular unit had been switched off on March 8, 2018. From that day onwards, LAXPC30 is no longer available for observation. The other two units (LAXPC10 and LAXPC20) have been functioning as usual.

AstroSat is India's first proposal-driven, multi-wavelength observation facility. Science data could be acquired corresponding to two kinds of observations: Announcements of Opportunity (AO) data and Target of Opportunity (ToO) data. Availability of AstroSat time for curated observations requested by PIs is circulated through AO cycles. Proposals are submitted for operating onboard science instruments for the purpose of deserved scientific objectives using a web-based utility system in AstroSat Proposal Processing System (APPS), ISSDC. Separate observation times are allocated for Target of Opportunity (ToO) observations which are quickly processed for level1 data and are place in the ISSDC archive. These data do not have any proprietary period and could be used immediately after initial data processing is complete.

2.3 X-ray Data Extraction Procedure

RXTE PCA

In order to create a single light curve or spectrum from a raw Science Array (SA) file(s), `saextrct` task is used by the user. This command allows the generation of the data products after filtering for Good Time Interval (GTI) information, for specific time windows of interest, for specific input channels, and phase information. This command takes level0 XTE/SA FITS file or a list of such files and produces level2 lightcurve or spectrum in standard FITS format. In order to filter for the good time corresponding to all the input files that are being processed by the *saextrct* task, one or multiple GTI information could be inserted via `GTIANDFILE` parameter. Up to 100 GTI files could be sorted and added together. Saxetrct also allows accumulating columns corresponding to different detectors or keep them as separate columns as the user decides. This could be realized through `ONE` (for summing of all columns) or `MANY` (for retaining of individual columns) option tag in the *accumulate* parameter. The name of the column in the input file to be binned is prompted through `COLUMNS` keyword. If `columns = "GOOD"` is inserted, only the good science data corresponding to the input filed would be sorted and processed. Similarly, if `ERROR` and `BACKEST` keywords are provided by the user, the corresponding error or background columns would be processed and accumulated. Products of desired time resolution could be obtained in providing suitable time resolution in seconds. Ftools task `TIMETRANS` allows the user to generate ASCII files containing time-stamps in absolute unit corresponding to desired time ranges. This ASCII file is then fed into `TIMEINT` prompt to produce data products in some particular time domain of interest. Set to default input `INDEF`, the set the time range over the entire domain of observation. Pairs of minimum-maximum channel bins could be inserted through `CHINT` keyword for generation energy-resolved data products. All channels are by default selected by this range is not specified by the user.

In order to correct the science data for background contamination, the ftool task `pcabackest` is available to produce synthetic background data by matching the respective background condition during the observation span. This estimation is performed by the use of suitable model files containing background observations corresponding to relevant quantities like spacecraft position with respect to South Atlantic Anomaly (SAA). Light curves and spectra for the background could be generated from the background data file

which comes as the end product of *pcabackest* task.

In order to run *pcabackest*, the input file or list of files are provided by the user. The Perl script then asks for the output file name and user-defined suffix. The name of the background model file generated by the PCA instrument team needs to be applied in *background model file* prompt. A list of model files containing different parameters could also be applied, or the 'CALDB' option could be resorted to for the selection of appropriate files from the calibration database. However, since the model files in CALDB are not being updated significantly, the PCA team recommends using appropriate background models provided in RXTE GOF. Default available or user-curated filter files need to be provided as well in order to provide additional parameters required by the model to estimate the background. In order to generate a separate background estimate for each anode layer, pcabackest must be instructed to include individual Xenon layers to produce one column corresponding to each anode. During the analysis of Standard1, Standard2, or Good Xenon modes, PCA gain correction need not be applied. For other modes, the final product should be produced after gain correction since the data is finally transmitted to the processing unit after combining counts from all PCA. SAA history files contain information regarding particle collection during SAA passage. This file is periodically updated by the PCA team and needs to be provided to correct for the exponential decay of activation after SAA transit.

The final background file we obtain contains the full 256 channel binning, but we need to rebin it as per our original data file. Ftools task `rddescr` is applied to generate an output file containing the binning information after reading the header of the original data file. Subsequently, using the task `rbnpha`, a distinct binfile could be produced and the final binned background product can be generated.

However, imperfect modeling of detector activation profile after SAA passage can sometimes result in imperfect background estimation. This leads to overall over or underestimation of actual background. One workaround for this problem is to filter all the data after 30 minutes of SAA passage. Since the profile is roughly exponentially decaying, this procedure provides corrected background estimation.

AstroSat LAXPC

Developed in TIFR/IUCAA, LAXPC spectral and timing analysis software `LaxpcSoft` is recommended for extraction and processing of LAXPC level1 data. The software contains two Fortran codes. One of them (`laxpcl1.f`) is used for scientific data processing and generation of time series, event files, source and background files as well as GTI files. The other code (`backshift.f`) is responsible for applying the gain shift to proper alignment of the source and background data and identification of desired response file specific to the observation.

In *laxpcl1.f*, multiple observations can be combined and the overlapping data is rejected. However, the program does not check for data gaps which are filled by data pertaining to subsequent observations. The output for each LAXPC detector is processed separately. Data corresponding to SAA passage and elevation more than a threshold of 3.5 degrees relative to Earth's limb are by default excluded. However, stray peaks that might have occurred during this time domain are subsequently filtered in the GTI file. The GTI can also be modified to generate data products pertaining to some particular time domain of interest.

The program with its present dimension is capable of processing 100 orbits simultaneously. In case more input files are fed into the program, products will be truncated and the task terminates with an error exit. In such a case the full observation has to be split into suitable segments.

The program provides a flag for event selection before producing the event file. By default, the program selects double events depositing all their energies in one single anode. However, using the suitable flag, only those events that deposit their energies in a single encounter with anode could be selected as well.

Before the creation of final products, an input file containing the list of relevant level1 files needs to be created by the user. For each orbit, these files included .tct (for the purpose of conversion from instrument time to UTC), .mkf (file containing data related to orbit, pointing details, etc), and two .FITS files containing event mode and binned mode data. All these files are sequentially read by the program. In order to perform this routine task, a shell script `findfile` is provided that reads all these inputs from the normal directory arrangement provided by level-1 `tar` file. The program will encounter an error if any of these files are missing or there are some additional redundant files.

The number of laxpc detectors to be included for data processing, the time resolution for the time series, the number of channels to be included, the number of anode layers to be used need to be provided by the user. The program provides options for the generation of data products during Earth occultation as well.

In order to generate the background spectra, a separate file containing the list of desired file names is also provided. The required files contain background photons as a function of latitude and longitude, background spectrum in low to high ULD count range (final background is produced by combining and multiplying by appropriate weightage factors), observed unscaled background spectrum, and fit to the background as a function of latitude, longitude, altitude. Before performing spectral studies, it is important to shift the background spectrum to the same gain as that of the source file. A proper response file needs to be added before generating background-subtracted spectra. Program *backshiftv3.f* is dedicated to the alignment of the source and background spectra and identifying the desired response file.

The program *backshiftv3.f* is designed to read the background ASCII files produced by *laxpcl1.f* as well as the gain measurements to gauge the amount of gain shift required to align the background and source spectrum files and then applies the gain. During this process, the program is not equipped to filter the double events, which may lead to artifacts such as bump-like features beyond 35 keV. The number of anodes to be used, the LAXPC detector, the number of channels to be used and other necessary details need to be provided by the user. The program also prints diagnostic messages including the suggested response file based on the observation date. Using the suggested response the entire program needs to be re-run to generate the final source and background spectra.

2.4 Analysis of X-ray Data

The timing and spectral studies were performed by general-purpose timing analysis package FTOOLS and spectral analysis package XSPEC (version 12.10.1) respectively. These tools provide specific tasks for carrying out different operations during the study. We discuss below the timing and spectral analysis details using these packages.

2.4.1 Timing Analysis

The task *fplot* reads the data vectors and corresponding error vectors from the input FITS file. The output is then transmitted to a general-purpose plotting software to enable the user to visually see the time variability along with the corresponding error bars. The data columns, error columns, and target columns are provided by the user. Further plotting commands can also be provided as strings in order to curate the plots. One or more legal plotting commands can be in a separate input file with `.pco` extension in the current directory of analysis. The first X-axis value can be taken as an offset for the X-axis by *offset=yes* keyword. By default, in one window 100000 points would be plotted. Separate plots will be generated for more data points.

In order to read data from an input FITS file and generate the power spectral density for one time series using FFT algorithm (default) or direct slow Fourier transform algorithm, FTOOLS task `powspec` is used. Both event mode and binned mode data can be inserted as input. Data filtration can be actualized using time, phase, or intensity windows. Within `XRONOS` tasks, the binning of the data is controlled by `BINS` and `NEWBINS`, subdivision of the time series is controlled by `INTERVALS` and final grouping of the output is controlled by `FRAMES`. The original time-bin is read from the input file searching for `TIMEDEL` keyword. However, during the analysis procedure, the user can rebin the data with the condition that this *newbin* must be larger compared to the original time bin and preferably an integer multiple of that (required by many XRONOS tasks). The entire observation domain can then be subdivided into several segments (*intervals*) and power spectral analysis on all such intervals would be carried out independently. The averaged out result would then be provided on one single frame. In order to obtain the white noise subtracted normalized power spectra, one can choose the `normalization` parameter to be -1.

By default, the task accepts a window file in ASCII for the exposure window. `XRONWIN` task enables the user to modify this window file and creating new window files as per requirement. The number of newbins per interval together with the newbin time dictates the length of time series to be processed within a single interval. This quantity decides the lower bound of frequency to be processed and displayed in a frame. The result obtained from all the intervals can finally be rebinned using a constant rebinning factor or a geo-

metric factor to produce equispaced intervals in the logarithmic scale. Values more than 1 represent constant rebinning factor; whereas values less than -1 represent geometric rebinning factor whose absolute value implies the step of the geometric series. The program also allows filtering an overall polynomial trend (up to 4th order) from the final PDS interval by interval using the least square method. the data gaps in the original time series can also be replaced by running averages. Like in the previous case, plt command file can be loaded as .pco extension.

In case interesting features like peaked components or QPOs are discovered over broadband noise, one wishes to fit the profile with appropriate model parameters to extract fitted parameters and gather scientific insights. For this purpose, the data can be fitted in `plt` interface. In case the coherence parameter $Q = \frac{\nu}{\Delta\nu} > 2$, the peaked component is qualified as QPO. Otherwise, they are just broad power peaks. The RMS power corresponding to the QPO provides information regarding the strength of the underlying oscillation as well.

2.4.2 Spectral Analysis

We have discussed the generation procedure of source and background spectra from raw data earlier. Another very important component is the inclusion of a response file that maps the channel number to energy and acts as a bridge between source and background. The spectrum obtained on-board is not the actual spectrum, but rather counts (C) on individual channels (I). The observed spectrum is given as

$$C(I) = \int_0^\infty f(E)R(I,E)dE \tag{2.1}$$

where $R(I,E)$ is the response of the detector and $C(I)$ is source spectrum. The detector response depends upon the probability with which a photon with energy E deposits its energy in channel I. This relation is not guaranteed to be invertible.

The standard procedure, therefore, is to construct the synthetic spectra using different models with model parameters (like $f(E, p_1, p_2, p_3...p_k)$) and compare it to the observed spectra by spectral fitting in suitable software like XRONOS package `XSPEC`. Before performing this exercise, the background spectrum must be subtracted from the source and the appropriate energy window in commensuration with the validity of the concerned model must

be zoomed in. At this stage, the response matrix must be loaded since that function calibrates the detector channels with incoming photon energies and produces a calibrated background-subtracted science-ready spectrum. Statistical tests are subsequently performed to gauge the goodness of the fit, to observe the residual pattern, and infer about selection and judiciousness of the model parameters. Different combinations of model parameters are tested for the most desirable spectral fit pertaining to the most robust fit statistic. The model parameters endowed with the most desirable statistic is known as the best fit model. Usually, in XSPEC the χ^2 test is performed which is encoded as

$$\chi^2 = (C(I) - C_m(I))^2/\sigma(I)^2 \tag{2.2}$$

where $C_m(I)$ stands for the model spectrum, $\sigma(I)$ is the standard error pertaining to the channel I. The χ^2 technique is a comprehensive assessment procedure for the acceptability of fits. In order to quantify this, it is important to consider the number of degrees of freedom ν (the difference between the total number of channels and number of model parameters) and consider reduced $\chi^2 = \chi^2/\nu$. In case reduced χ^2 approximately equals to 1 and < 2, the fit is considered to be statistically viable.

However, this exercise is contingent upon the number of model parameters being used, and it may happen that a model with too many parameters is making the model more complicated with no considerable improvement in the fit statistic. This can be tested using F-statistic which is denoted as

$$F_\chi = \frac{\chi^2(m) - \chi^2(m+1)}{\chi^2(m+1)/(N-m-1)} \tag{2.3}$$

where the fractional improvement of reduced χ^2 for changing one parameter of the model has been considered. Here N is the number of bins and m is the number of free parameters.

Thus the core objective of the spectral fitting is to extract the best-fitted parameters corresponding to the fitting function, but apart from the fitted parameters, one needs to declare the associated parameter uncertainties as well. The quality of fit is described by reduced χ^2 value, and corresponding parameter uncertainties describe the probabilities that estimated parameters are reliable estimators of the underlying parent parameters. These probabilities need to be determined to numerically assert the *confidence level* of the obtained fits.

The probability density function of Gaussian of random variable x with mean μ and standard deviation σ is given by

$$P(x;\mu,\sigma) = \frac{1}{\sqrt{2\pi}\sigma}\exp(-\frac{1}{2}(\frac{x-\mu}{\sigma})^2). \tag{2.4}$$

Approximately 68% of the total number of measurements of repeated experiments lie within $\pm\sigma$. This is a probabilistic statement, in the sense that for a series of identical experiments there is a 68% chance of obtaining the parameters within $\pm\sigma$. Similarly, one can report the values with $\pm 2\sigma$ or $\pm 3\sigma$ confidence levels, with corresponding probabilities approximately 95% and 99% respectively. Uncertainties in the measurements may not always be symmetrically distributed around the mean.

However, for multi-parametric cases with the parameters exhibiting some correlation among them, the confidence level cannot be determined in a straightforward way. In such cases in order to determine confidence levels for two model parameters, other fitted parameters need to be frozen at their best fit values and then the fit is allowed to run to obtain the best-fit parameters corresponding to a minimum reduced χ^2 value (Bevington 1969). This exercise produces closed contours in the 2D parameter subspace and the contours indicate the parameter values for 1,2 and 3σ confidence levels. The tilt of the contours is indicative of the parametric correlations. In the ideal case for two parameters with no correlations, the contours should trace out concentric circles.

2.4.3 Analysis Using XRONOS Package XSPEC

In order to obtain all our spectral results, we have extensively used XRONOS package XSPEC, which is a command-driven, interactive, detector non-specific X-ray spectral analysis program dedicated to the X-ray astrophysics community. It has compatible versions for Linux, MACOSX, and Cygwin. Recently, a python interface PyXSPEC has been launched as well. It enables the user to calculate fit statistics, introduce new models, and study spectral features using external models, and to visualize data features using inbuilt visualization capabilities. Taken together, it is an extremely efficient, user-friendly, multipurpose spectral analysis software that has made X-ray analysis quite convenient.

The tcl user interface of XSPEC provides an interactive platform between the user and XSPEC. A tcl interpreter is initialized with the opening

of XSPEC and successive XSPEC commands are added to it. Tcl being a comprehensive scripting language by itself enables the user to write task-specific scripts using loops and branching involving XSPEC commands and execute to generate desired outputs. The tcl interpreter accepts short, unambiguous versions of any XSPEC command in an interactive session. However, in an interactive script, such abbreviations are not recognized. The XSPEC interactive session also accepts operating system commands. In case wild cards (like ls *.lc) are required for file globbing, the operating system command has to be preceded by *syscall*, which executes commands in the user's current shell.

In order to perform the spectral analysis, XSPEC requires recorded spectra ($D(I)$), background file ($B(I)$), the instrument response ($R(I, E)$) and a collection of model spectra ($M(I)$). The data file contains the number of registered photons per channel, and XSPEC then uses the background spectra to obtain the observed spectra by calculating the background-subtracted count using

$$C(I) = \frac{D(I)}{a_{D(I)}t_D} - \frac{b_D(I)}{b_B(I)}\frac{B(I)}{a_B(I)t_B}, \tag{2.5}$$

where t_D and t_B are the exposure times of data and background respectively, $b_D(I)$ and $b_B(I)$ are background scaling factors, $a_D(I)$ and $a_B(I)$ are area scaling factors from the data and background respectively. This method normalizes the source and background flux over an equal area. Before XSPEC can infer anything about the spectral features, the instrument information in the form of response function $R(I, E)$ must be fed into the software. This is a continuous function of energy but can be converted to discretized form for the purpose of generation of response matrix by

$$R_D(I, J) = \frac{\int_{E_{J-1}}^{E_J} R(I, E)dE}{E_J - E_{J-1}}. \tag{2.6}$$

This response matrix is stored in the response file in a compressed format and is read by XSPEC. Sometimes another array $A_J(I)$ is also used alongside the standard response matrix. This array represents the detector efficiency as a function of channels and

$$\bar{R}_D(I, J) = R_D(I, J) \times A_J(I), \tag{2.7}$$

is known to be the Redistribution Matrix Function (RMF). XSPEC calculates the model spectra internally using the corresponding energy blocks via

$$M_D(J) = \int_{E_{J-1}}^{E_J} M(E)dE \tag{2.8}$$

in the unit of photons per unit area per unit time. XSPEC provides the flexibility of using additive and multiplicative models both. The additive components are used for different X-ray sources within the system, and multiplicative models are used in case some particular X-ray component is modulated by some energy-dependent factors (like in the case of absorption by the intervening medium) or modulation of one X-ray source by some other source. This addition and convolution models together can be employed to examine complex physical processes.

After the data is loaded in XSPEC and models are defined, XSPEC runs suitable fitting algorithms in order to determine the best fit values of underlying model parameters. In case the best fit parameter values are being searched in a multidimensional parameter space using a complicated nonlinear model, the convergence time towards the minimum of χ^2 value depends upon the choice of searching algorithm, the step size, and the numerical values of the initial guess parameters. For convenient and feasible starting parameter values, synthetic spectra for different ranges of model parameters could be plotted and through visual inspection and comparison with the source spectrum, initial values could be taken. Alternatively, model parameters and excursions of simple models can guide the rough parameter ranges to be used for complicated model fits. In our case of fitting the spectra using TCAF, we came up with the relative variations of accretion rates and shock location, which we have explained in Chapter (3,4).

There can be local minima and valleys in the parameter space which can produce feasible χ^2 values but unreasonable fits. In such cases, a collection of initial parameter values could be tried and fit can be rerun. Tighter convergence requirements can be imposed (reduced $\chi^2 < 0.5\%$) in the expectation that the program will escape from the problematic parameter space domain and proceed towards global minima. With a collection of similar parameter values, if the fitting procedure proceeds towards a common set of fitted parameters, that can as well be considered to be a reliable fit corresponding to the observation. Small perturbations of the parameters relative to the minima should not alter the fitted parameters altogether and the parameters should converge to the same ballpark values.

The measure of the goodness of fit, namely the *likelihood function* for k

number of parameters is defined as

$$P(a_1, ..., a_k) = \prod_i \left[\frac{1}{\sigma_i\sqrt{2\pi}}\right] \exp\left(-\frac{1}{2}\sum_i \left[\frac{y_i - y(x_i)}{\sigma_i}\right]^2\right). \quad (2.9)$$

This likelihood function is maximized when the exponent is minimum. Here x_i and y_i are the measured values of the corresponding variables, $y(x_i)$ is the actual value of the function at x_i and σ_i is the uncertainty in the measurement. As seen from Equation (9), χ^2 depends quadratically on the distance from the minimum. This is also seen if we expand χ^2 relative to its true minimum

$$\chi^2(a_1, ..., a_n) \simeq \chi_0^2 + \sum_k \frac{\partial\chi_0^2}{\partial a_k}(a_k - a_k') + \frac{1}{2}\sum_k\sum_j \frac{\partial^2\chi_0^2}{\partial a_k \partial a_j}(a_k - a_k')(a_j - a_j'). \quad (2.10)$$

Since minimization of χ_2 requires the first partial derivative to vanish, near a local minimum or valley in the parameter space spanned by $a_1, ..., a_n$ the χ^2 value is expected to quadratically depend on the parameters. The method of expansion of the fitting function about its minima enables to find the minima quite rapidly but does not guarantee reliable performance in case the starting points are beyond the parabolic region around the valley. On the other hand, one can search for the steepest descent in the parameter space and make the iteration go in that direction, but this process becomes slower and slower near the minima. For this reason, XSPEC employs the Levenberg-Marquardt algorithm for best-fit search, which behaves like gradient descent as the search starts and then slowly behaves like an analytical expansion method as the minimum is approached. At the end of the search, XSPEC prints out the best fit values along with the confidence levels. However, these are 1σ confidence intervals and are calculated from the second derivative of χ^2 with respect to the fitted parameters. Therefore, they are not helpful as such and can only be used for a first-order approach of inferring the feasibility of fits. XSPEC provides `error` command to find the confidence intervals and uncertainties of individual parameters by fixing a parameter at the best fit value and fitting the other parameters to obtain the best fit values of the other parameters at the end of confidence intervals using a cubic spline interpolation method. Parameters can be stepped from one particular value to another with user-specified step sizes using `steppar` command. This procedure is instrumental in defining a grid on these pa-

rameters and using the visualization tools, confidence contours of concerned parameters on 2D parameter subspace can be displayed.

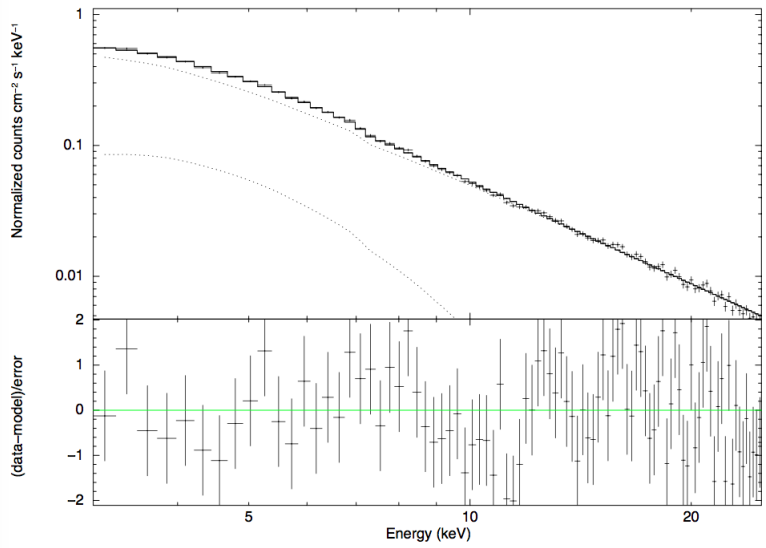

Figure 2.3: Data with unfolded model and the χ^2 pattern is depiced after GRS 1915+105 spectrum is fitted with *diskbb+power-law*. The fitting has been done in 3.0-25.0 keV. A 2% systematic has been used to obtain the spectral fit.

While choosing the step sizes during spectral fitting, one needs to consider that too small a step size would take a long time to converge and produce desirable fits; on the other hand, with too big step size, the search process can skip the minima. For this reason, the step size should be proportional to the parameter values and can often be decided on a trial and error basis. In our case, we found a step size of $\sim 0.1\%$ to be convenient for all our fitting exercises.

While employing the χ^2 statistics it is normally assumed that the photon counts in all the channels are distributed in Gaussian and the variance is uncorrelated with the observed photon intensity. In case the count in the channels is low for a faint source or in the higher energy domain, then one can alternatively use C-statistic. This can be activated using `statistic cstat` command prompt in XSPEC interface. However, in our case, the photon intensity in all the channels was sufficient ($\sim$ few thousands/s), which implies only χ^2 was found to be useful.

In case the user is not interested in the default resolution of the spectrum because of the low signal-to-noise ratio, XSPEC allows the modulation of resolution by its default functionalities. Two FTOOL commands are quite helpful for this purpose. The `rbnpha` command helps to bin the output file in a non-reversible manner and this is used to ensure that the binning of the output file is the same as that of the response file or source spectrum. This we have employed in the analysis of RXTE as we attempted to bin the background file. On the other hand `grppha` command is used to sum the proper channels corresponding to the user-specified flag to enhance the S/N ratio. In the case of both RXTE and AstroSat, since we are working with a bright source in a moderate X-ray domain, the photon intensity is sufficient for spectral analysis and we did not have to worry about the S/N ratio.

In order to fit the observational data, XSPEC includes a large assortment of models. The XSPEC models can be broadly divided into three categories: additive, multiplicative, and convolution model. In the case of the additive model, the counts in different channels corresponding to the simulated spectra are added. In the case of the multiplicative model, on the other hand, the bin-wise multiplicative factor is applied before producing the output. However, the convolution model allows this transformation to occur across energy bins so that the final product is the integrated effect across all the channels.

Sometimes it becomes important to introduce user-specified models to explain some specific physical scenario. For this purpose, XSPEC allows the user to define three types of curated models: *atable* for additive models, *mtable* for multiplicative models, and *etable* for exponential multiplicative models. The customary process is to define an N-dimensional grid of simulated spectra generated out of different combinations of N number of model parameters defined by the user. The grid spacing corresponding to different parameters in the model is decided based upon the requirement and the context of the problem. The tabulated values of all the parameters have to be in ascending order. Once this grid is provided, XSPEC runs linear interpolation to obtain the parameter values required for the fits.

Running table model components can be computationally more expensive compared to a simple algebraic model, especially in case they have a large number of parameters. The memory requirement for the linear interpolation process runs as 2^N, where N is the number of model parameters. Since the interpolation scheme, in this case, is linear, the second derivative of the underlying Levenberg-Marquardt algorithm may not always be accurate.

For this reason, a significant number of grid points for all those parameters is necessary. One simplification and some reduction of execution time are realized if one model parameter is decoupled from the other parameters and adds to the spectral distribution in a linear fashion. With 'M' such additive parameters, each such grid point contains 'M+1' model spectra. This reduces the size of the matrix.

For our purpose, we have used 'atable' model to include TCAF, which requires the flux of synthetic spectra to be recorded in photons/cm/s. This model has been used with other additive and multiplicative models for the purpose of explanation of the complete physical scenario.

Once the spectra are fitted using some model, it is very important to study the residual χ^2 pattern to understand what fraction of flux across energy bins is being explained by the applied model. In case it is observed that the residual pattern shows a hump-like behavior in some energy domain, it may be indicative of excess emission and other model components would be necessary to compensate for that flux. This is also important to prompt the user to look for plausible line emission or absorption profiles at specific energies and include them in the model. This way the complete set of models fitting for some particular spectrum may be incrementally come up with and this method has been predominantly followed in the literature to explain a wide assortment of physical scenarios pertaining to astrophysical systems.

Chapter 3

Spectral Analysis of the χ Class Data of GRS 1915+105

3.1 Introduction

Galactic black hole source GRS 1915+105 is extensively studied owing to its vast array of time variabilities across different wavelengths and time-scales. Unlike the standard transient sources, this source has never been found to be in the usual 'hard state' since detection until June 2018, when GRS 1915+105 entered into an unusually extended phase of low X-ray and radio intensity (Negoro et al. 2018; Motta et al. 2019). Subsequently, after 2019 March further decline in the X-ray flux followed by renewed flaring activity in different wavelengths have been detected (Koljonen et al. 2019; Trushkin et al. 2019; Motta et al. 2019, 2021). Using near-infrared spectroscopic observations, the companion of this source was found to be a Low Mass X-ray Binary (LMXB) of mass $1.2 \pm 0.2\ M_{\odot}$ (Greiner et al. 2001). It was further established to be a Galactic microquasar after the detection of powerful superluminal ejections for the first time in any Galactic source (Mirabel & Rodriguez 1994).

Apart from these powerful ejections, investigations over the past few decades have reported the occurrences of radio oscillation events (Pooley & Fender 1997) as well as extended periods of the so-called 'radio plateau' states as well (Fender et al. 1999). Such plateau states are found to be associated with energetic radio flare events (Fender et al. 1999; Klein-Wolt et al. 2002). Different groups have come up with their respective interpretations regarding these associations.

Among the different intensity patterns of this source denoted by different classes and sub-classes, the χ classes are characterized by negligible variability over extended periods of observation (Belloni et al. 2000). Depending upon the color-color diagram and the hardness ratio, χ class was further sub-divided into four sub-classes: $\chi_{1,2,3,4}$. Even though the absolute photon intensity can vary from one χ class to another, the intensity fluctuation within a particular observation remains within 3σ. Further, two sub-classes ($\chi_{1,3}$) are particularly interesting for the simultaneous manifestation of ejection in radio/IR band (Pooley & Fender 1997; Eikenberry et al. 1998). It had further been shown by Naik & Rao (2000) that the radio association is strongest in β, θ and $\chi_{1,3}$ classes. It was clearly shown that radio emissions are associated with soft X-ray dips.

Since the hardness ratio or the color-color diagram depends on the choice of energy bands for the soft and hard photons, and therefore, on the mass of the black hole (BH), an alternate mass-independent description regarding the emergence of these classes was given (Pal, Chakrabarti & Nandi, 2013) in terms of the Comptonization efficiency (CE) which, in reality, is a dynamic hardness ratio, given by the instantaneous ratio of the number of photons under the power-law (N_p) and the number of photons under multi-color black body (N_b) component of the composite spectra. All the variable and non-variable classes were arranged in ascending order of CE ($=N_p/N_b$). Since N_p is nothing but a fraction of N_b which are intercepted by the Compton cloud, CE also gives an idea of the flow configuration - a large CE would mean a large Compton cloud, which will necessarily yield a hard state. In this sequence, χ naturally appeared at the end, where the spectra are the hardest. In this scheme, similar 'looking' classes as far as the light curves are considered, have similar CEs and the sequence is also the same for other objects (e.g., IGR 17091-3624) which exhibit variability classes (Pal & Chakrabarti, 2015). This sequence is found to be independent of the mass of the black hole.

Even though GRS 1915+105 is of recurrent interest in the scientific community in the context of plausible disk-jet connection (Vadawale et al., 2003; Fender, Belloni & Gallo, 2004), a complete picture in terms of accretion flow components is still lacking. However, some conjectures have been floated regarding the accretion flow configuration in relation to the nature of ejection. The radio flares were subdivided into two categories on the basis of the properties of accretion disk evolution: (1) Persistent radio flares where the accretion disk remains steady. In this case, the inflow and the outflow are in equilibrium and there is no sudden change in either soft or hard com-

ponents. (2) Other types of flares which are associated with changes in the accretion disk. Here the hard and soft components are affected and the object proceeds towards a state transition (Yadav 2001, 2006). Pal et al., (2013, 2015) studied mainly with the spectral fits using phenomenological power-law (PL) and disk blackbody (DBB) models and also to obtain the hardness of the object in different timing classes. However, flow parameters have not been computed earlier by fitting the spectra using physical models like TCAF. Therefore, we have made an attempt to extract the accretion flow properties corresponding to the different sub-classes of χ and provide a plausible accretion flow configuration to explain the characteristics of these sub-classes.

3.2 Data Selection and the Method of analysis

For the spectral analysis, RXTE science data from NASA HEASARC data archive are used. We consider one observational data from each of $\chi_1, \chi_2, \chi_3, \chi_4$ classes as identified in Pal et al. (2013), and continuous observation span is divided into several slices to carry out spectral analysis over each one of the segments separately in order to have a better statistics on fitted parameters. HEASARC's spectra generating software package HEASOFT version HEADAS 6.18 and XSPEC version 12.8.2 has been used for the extraction and analysis of the spectra. For the generation of '.pha' files and fitting of the spectra using TCAF solution, the procedure described by Debnath et al. (2013, 2014) has been employed. The *standard2* mode Science Data of the PCA instrument was used for spectral analysis. For each observation ID, the spectrum was extracted from all the Xenon layers of PCU2 containing 128 channels, without any grouping. The PCA background was extracted by 'runpcabackest' command. In order to model the background, the latest bright source background model file was used. In order to exclude the data during the South Atlantic Anomaly (SAA) passage, PCA SAA History file was incorporated. The data acquired for elevation less than 10° and offset less than 0.02° has been excluded as well for the purpose of our analysis. The $2.5 - 25.0$ keV background-subtracted spectra were fitted by TCAF based local model fits file. We have checked that the spectral fitting over a wider energy band (2.5-150.0 keV) does not qualitatively change the conclusion we

draw from our analysis. Therefore, we have done our spectral analysis within the low energy domain (2.5-25.0 keV) only. The 'err' command was used to determine the 90% confidence error values of the corresponding model fitted parameters.

In order to take care of the interstellar absorption, the multiplicative model *phabs* was employed. While in Muno et al. (1999) the hydrogen column density was kept fixed at 6.0×10^{22} atoms/cm^2, it was kept frozen at 5.0×10^{22} atoms/cm^2 in the process of fitting the steady-state spectra by other observers (Lee et al., 2002; Peris et al., 2016). The column density was also kept in the range $(4.5 - 7.0) \times 10^{22}$ atoms/cm^2 by Peris et al. (2016), but no significant departure of the fitted parameters was noticed. While analyzing the low/hard state of GRS 1915+105 to measure the spin, Blum et al. (2009) considered the absorption column density to be 4.0×10^{22}. On the other hand, while measuring the correlation between disk parameters and superluminal jet parameters, N_H had been considered to be at a higher value of $(10.0 - 15.0) \times 10^{22}$ (Yadav 2006). Throughout our analysis, we have found N_H to be in the range $(4.5 - 7.5) \times 10^{22}$.

The PCA data IDs chosen for the analysis of χ_2 and χ_4 class data respectively are 20402-01-16-00 (MJD=50501) and 10408-01-33-00 (MJD=50333). For χ_1 and χ_3 classes, we used PCA data of observation IDS 10408-01-23-00 (MJD=50278) and 20402-01-50-00 (MJD=50735) respectively. The $\chi_{2,4}$ class data are fitted with the TCAF solution-based model *fits* file only, for which four input parameters other than normalization (N) are supplied: (i) Keplerian disk rate ($\dot{m}_d$ in $\dot{M}_{Edd}$), (ii) sub-Keplerian halo rate ($\dot{m}_h$ in $\dot{M}_{Edd}$), (iii) location of the shock front (X_s in Schwarzschild radius $r_s = 2GM/c^2$), (iv) compression ratio R ($=\rho_+/\rho_-$, i.e. ratio of post-shock density to pre-shock density). In the TCAF model, two auxiliary parameters, namely, the mass of the black hole (in solar mass $M_\odot$) and normalization (N) (it scales up or down the entire model spectra to match the observed spectra) are generally found to be constant. N depends on the intrinsic source parameters: mass of the black hole, distance and disk inclination angle. So, in general, N does not vary for a particular source (in observations with the same satellite instrument). But, one may require higher N values to fit spectra if there are significant effects of jet or other physical processes, whose effects are not included in the present model fits file. To obtain the best model fits, a Gaussian emission line of peak energy at around 6.5 keV is used to take care of the iron line emission.

Although $\chi_{2,4}$ are radio-quiet, $\chi_{1,3}$ classes are radio-loud i.e., there is a

significant flux contribution from jets or outflows. In the case of $\chi_{1,3}$, the TCAF model was not sufficient to fit spectra due to the presence of outflows that could be emitting non-thermal X-rays (see, Chakrabarti 1999; Jana et al. 2016b, 2017). Thus, in order to achieve the best fit in these two classes, we used an additional *Cutoffpl* model. The cutoff power-law profile is given by the equation $A(E) = KE^{-\alpha}\exp(-E/\beta)$, where α is the power-law photon index, β is the exponential roll-off in keV and K is the normalization in the unit of photons/keV/cm^2/s. The strength of α and β parameters will indicate relative dominance of the outflow in χ_1 and χ_3 classes. These *Cutoffpl* parameters, together with TCAF fitted parameters enable us to draw the connection between the spectro-temporal aspects of the source with the accretion flow features. In order to disentangle the contributions from the TCAF configuration and the outflow, we allowed the normalization parameter N to vary. Variation of the peak flux would be dependent on the variation of the accretion rates, and therefore, any error in determining the accretion rates would be reflected in the error of normalization. There are statistical errors in the observational data as well. Keeping these in mind, we first determined the energy range up to which the spectra could be fitted using TCAF solution alone, and no additional model component was needed. This allows us to determine the average normalization which was kept frozen to obtain spectral fits in the $2.5 - 25.0$ keV energy range.

3.3 Theoretical Background

It is now generally understood that two components (Keplerian and sub-Keplerian) are essential to explain the spectral and timing features of the black holes. It has also been demonstrated subsequently that jets and outflows are launched from within the CENBOL region (Chakrabarti 1999a). The strength of the outflow as a function of the inflow parameters has been discussed in Chakrabarti et al. (2000) and Chakrabarti & Nandi (2000).

In Fig. 3.1(a,b), adopted from Chakrabarti et al. (2000), two possible accretion flow configurations pertaining to $\chi_{2,4}$ and $\chi_{1,3}$ sub-classes are shown respectively. In Fig. 3.1(a), we have shown the standard flow configuration around the black hole consisting of Keplerian and sub-Keplerian matter both. If the conditions for shock formation are satisfied and the viscosity is small enough to maintain a low Keplerian disk rate, the outflow may be launched from close to the black hole. In case the average optical depth within the

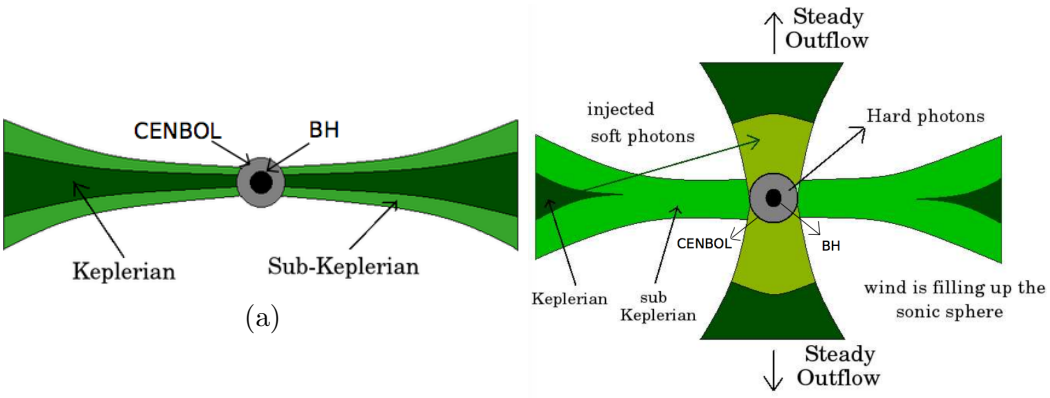

Figure 3.1: (a) The accretion flow consisting of Keplerian and sub-Keplerian components. Their relative abundance dictates the hardness or softness of the state. This configuration corresponds to $\chi_{2,4}$ class. (b) The shock produced due to satisfaction of Rankine-Hugoniot conditions. In both of the Figures, the grey shaded region around the black hole represents the CENBOL. Since within the sonic sphere the average optical depth is smaller than unity, a steady outflow rate is maintained because of inefficient cooling of the outflow base. This corresponds to $\chi_{1,3}$ class (adopted from Chakrabarti et al., 2000).

base of the outflow is low such that the inverse-Compton cooling is inefficient, the outflow does not collapse and a steady mass ejection rate is maintained. This configuration is presented in Fig. 3.1(b) (also see, Chakrabarti 1999a). Initially, as the shock strength increases from unity, the outflow rate also goes up (Chakrabarti 1999a). With the gradual enhancement of matter density within the sonic sphere, the optical depth also rises, which leads to more efficient inverse Compton cooling. The outflowing matter beyond the sonic sphere is separated out as a blob and the cooler matter returns back to the inflow, creating the so-called 'burst-on' state. (Chakrabarti & Nandi, 2000). A further rise in the shock strength reduces the outflow rate. If the viscosity is high enough to enhance the Keplerian disk rate, the spectra become softer. The CENBOL region is cooled down catastrophically, which leads to the complete quenching of the outflow.

Muno et al. (1999) and McClintock et al. (2006) reported that classes with quasi-stable flux profiles often resemble the hard states of persistent sources. In the spectral and temporal study of GRS 1915+105 by Rao et

Table 3.1: TCAF Model Fitted Parameters of χ_2 and χ_4 class data in the 2.5-25.0 keV energy band with the normalization kept free. Variations of TCAF flow parameters, viz. disk accretion rate ($\dot{m}_d$), halo rate ($\dot{m}_h$), shock location (X_s), the shock strength (R) and model normalization (N) with the chosen time segments along with the respective error bars are listed. Reduced χ^2 of the spectral fits are listed in the last column.

Variability class	$\dot{m}_{\rm d}$ (in $\dot{M}_{Edd}$)	$\dot{m}_h$ (in $\dot{M}_{Edd}$)	X_s (in $M_\odot$)	R (in r_s)	N	χ^2/dof
χ_2	$0.797^{+0.02}_{-0.02}$	$0.161^{+0.001}_{-0.001}$	$47.302^{+0.07}_{-0.07}$	$1.233^{+0.001}_{-0.001}$	$22.125^{+0.016}_{-0.015}$	55.08/45
χ_4	$4.470^{+0.06}_{-0.06}$	$1.132^{+0.001}_{-0.001}$	$38.635^{+0.06}_{-0.06}$	$1.080^{+0.001}_{-0.001}$	$23.448^{+0.093}_{-0.092}$	46.84/44

al. (2000) to anchor the origin of the hard photons, the spectral fitting of χ_3 class was performed using *diskbb+CompST+Cutoffpl* model combination. In TCAF paradigm, the contribution from the thermal flux and its inverse Compton scattering from the hot CENBOL region are self-consistently accounted for by solving the radiative transfer equation, there is no requirement for separate phenomenological models. However, in order to account for the additional Comptonization of seed photons from the outflow base as well as possible synchrotron emission from the outflow, additional models like Cutoff power-law (*Cutoffpl*) might be required.

Since mass is the intrinsic property of the black hole and not a flow parameter. Therefore, for the purpose of our analysis, we have kept the mass of the black hole frozen at $14M_\odot$, while fitting spectra with the TCAF model fits file.

3.3.1 Analysis of χ_2 and χ_4 Class data

A comparison of the spectral natures of χ_2 class (Obs. Id. 20402-01-16-00) and χ_4 class (Obs. Id. 10408-01-33-00) is indicative of the fact that the soft flux is higher in χ_4 across the entire energy band of our analysis (Fig. 2). Since the spectral features carry the signatures of the accretion flow dynamics and the flow parameters, the salient features of the observed spectra of $\chi_{2,4}$ classes are expected to be corroborated by the spectral fitted parameters.

In the case of χ_2 class, the uninterrupted observation span of 3000 seconds has been selected and spectral fitting has been carried out using the *TCAF+Gaussian* model. The flow parameters, namely, the disk accretion

rate ($\dot{m}_d$), the halo rate ($\dot{m}_h$), the shock location (X_s) and the strength of the shock (R) have been determined. The same task has been performed in the case of χ_4 class data as well over the 800-second continuous observation span. The spectral fitted parameters corresponding to the two classes are listed in Table 3.1.

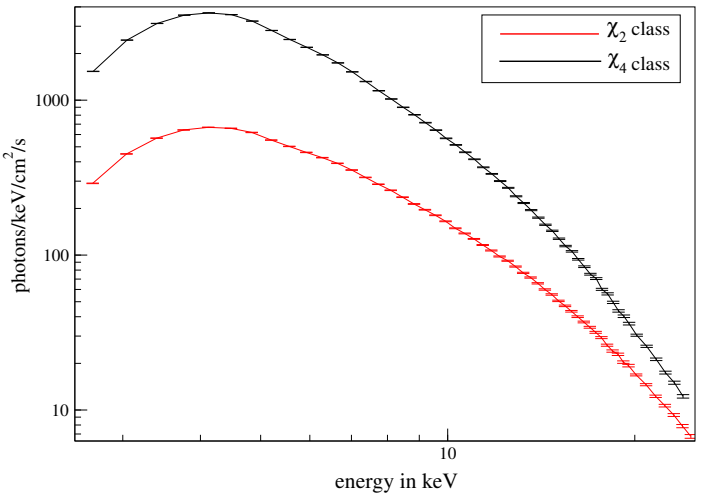

Figure 3.2: Comparison of the observed spectra for χ_2 and χ_4 class data. The low energy flux in case of χ_4 class is greater than that of χ_2 class.

It is also quite evident that in the case of χ_4 class, the disk accretion rate is significantly larger compared to that of χ_2 class. This commensurate with the higher thermal flux of χ_4 class data. However, since $\chi_{2,4}$ classes are devoid of any outflow, the normalization does not change significantly between the two classes ($\sim$ 20). In the case of χ_4 class, the shock location moves inwards with the enhancement of the disk accretion rate. Fig. 3.5(a) features the data to model ratio for the fitted spectrum in χ_2 class. In Fig. 3.6(a), we provide the 66-90-99% contours for Keplerian and sub-Keplerian rates in the case of χ_2 class.

3.3.2 Analysis of χ_1 and χ_3 Class data

We now summarize our observations from the spectral analysis of χ_1 and χ_3 class data. Unlike $\chi_{2,4}$ classes, substantial activity in the radio domain has

Table 3.2:TCAF Model Fitted Parameters of χ_1 and χ_3 class PCA spectra in the 2.5-25.0 keV energy band with model normalization kept free. We have listed the variations of TCAF parameters, viz. disk accretion rate ($\dot{m}_d$), halo rate ($\dot{m}_h$), shock location (X_s), the shock strength (R) and model normalization (N) and the *Cutoffpl* parameters with the chosen time segments along with the respective error bars. The reduced χ^2 of the spectral fits are also listed in the last column.

variability class	$\dot{m}_d$ (in $\dot{M}_{Edd}$)	$\dot{m}_h$ (in $\dot{M}_{Edd}$)	X_s (in r_s)	R	N	α	β (in keV)	Cutoffpl Norm	χ^2/dof
χ_1	$1.750^{+0.02}_{-0.02}$	$0.362^{+0.001}_{-0.001}$	$27.5^{+0.31}_{-0.27}$	$1.052^{+0.001}_{-0.001}$	$17.56^{+0.16}_{-0.16}$	$2.082^{+0.003}_{-0.002}$	$15.9^{+0.09}_{-0.09}$	$9.10^{+0.039}_{-0.038}$	35.92/41
χ_3	$1.131^{+0.01}_{-0.01}$	$0.182^{+0.003}_{-0.002}$	$20.1^{+0.03}_{-0.02}$	$1.438^{+0.002}_{-0.002}$	$2.85^{+0.06}_{-0.06}$	$1.563^{+0.01}_{-0.01}$	$15.7^{+0.08}_{-0.08}$	$3.23^{+0.003}_{-0.003}$	42.63/40

been detected, implying the presence of an outflow. In order to account for the inverse-Comptonization from the base of the outflow, we used *Cutoffpl* model in addition to TCAF to for the purpose of our spectral fitting in $2.5-25.0$ keV. A qualitative comparison of the observed spectra of χ_1 class (Obs Id. 10408-01-23-00) and χ_3 class (Obs Id. 20402-01-50-00) suggests that the thermal flux is more dominant in the case of χ_1 class.

Owing to the presence of an outflow, the spectral fitting exclusively with TCAF could not be accomplished over the entire range, but over only a limited energy band. The relative hardness of χ_3 implies the difference in outflow contribution in χ_1 and χ_3 classes. For this reason, the energy range of feasible TCAF fitting in these two classes was different.

Our next objective is to examine whether the contribution from TCAF and *Cutoffpl* could be segregated. In that case, there is a possibility that the accretion and outflow characteristics are explainable independently without the interference of one on another. For that purpose, after fitting the spectra using TCAF in the limited energy range, the obtained normalization was kept frozen in the *TCAF+Cutoffpl* fitting over the entire $2.5-25.0$ keV energy range.

• **Spectral fitting using *TCAF+Cutoffpl* model for χ_1 class:** The continuous 3000-second observation was chosen for spectral fitting in the $2.5-25.0$ keV energy range. The disk rate and the TCAF normalization over the entire $2.5-25.0$ keV range were found to be around 1.75 $\dot{M}_{Edd}$ and 17.5 respectively. The spectral fitted parameters using *TCAF+Cutoffpl* model in

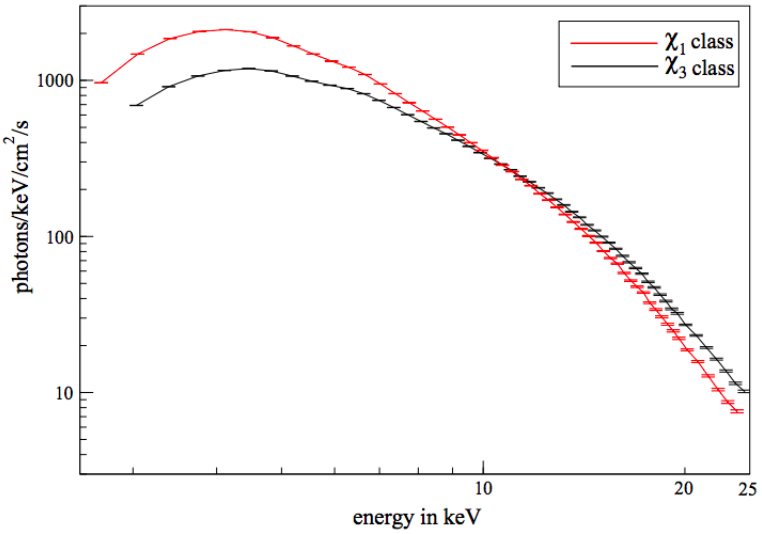

Figure 3.3: Comparison of the spectra between χ_1 and χ_3 class. The energy flux at lower energy is greater in the case of χ_1 class. The relative hardness of χ_3 class is evident from the spectral slopes.

the 2.5-25.0 keV have been given in Table 3.2. The α and β parameters in *Cutoffpl* model have been found to be around 2.08 and 15.95 keV respectively. However, as stated earlier, because of the presence of outflow, the entire range could not be fitted with TCAF solely. In the case of χ_1 class, only in the range 2.5-16.5 keV, the spectral fitting could be accomplished using TCAF only. The normalization was found to be around 27.46.

The spectral fitting using *TCAF+Cutoffpl* is repeated by keeping TCAF normalization frozen at $N = 27.46$ and the flow parameters are extracted. The parameters do not change significantly from those reported in Table 3.2. The fitted parameters are listed in Table 3.3. In Fig. 3.5(b), the data to model ratio along with the individual components is provided.

• **Spectral fitting using *TCAF+Cutoffpl* model for χ_3 class:** We wanted to study the relative behavior of χ_1 and χ_3 class in terms of flow parameters. For that purpose, the same kind of spectral analysis as that of χ_1 class is accomplished in χ_3 class as well. In this case, a continuous 2000 second observation interval was chosen for spectral fitting using *TCAF+Cutoffpl*

Table 3.3:TCAF Model Fitted Parameters for χ_1 and χ_3 class PCA spectra in the $2.5-25.0$ keV energy band with the normalization for TCAF frozen at the values as obtained from solely TCAF model fits over a smaller energy range. We have listed the variations of TCAF model parameters, viz. disk accretion rate ($\dot{m}_d$), halo rate ($\dot{m}_h$), shock location (X_s), the shock strength (R) and the additional *Cutoffpl* model parameters with the chosen time segments along with the respective error bars. The reduced χ^2 of the spectral fits are also listed in the last column.

Variability class	$\dot{m}_d$ (in $\dot{M}_{Edd}$)	$\dot{m}_h$ (in $\dot{M}_{Edd}$)	X_s (in r_s)	R	α	β (in keV)	Cutoffpl Norm	χ^2/dof
χ_1	$2.494^{+0.04}_{-0.02}$	$0.367^{+0.002}_{-0.002}$	$32.434^{+0.11}_{-0.10}$	$1.052^{+0.006}_{-0.005}$	$1.871^{+0.04}_{-0.04}$	$13.674^{+0.02}_{-0.02}$	$6.323^{+0.04}_{-0.04}$	35.66/42
χ_3	$1.131^{+0.02}_{-0.01}$	$0.172^{+0.002}_{-0.002}$	$21.064^{+0.14}_{-0.14}$	$1.373^{+0.005}_{-0.004}$	$1.500^{+0.02}_{-0.02}$	$15.064^{+0.08}_{-0.08}$	$2.744^{+0.01}_{-0.01}$	40.48/41

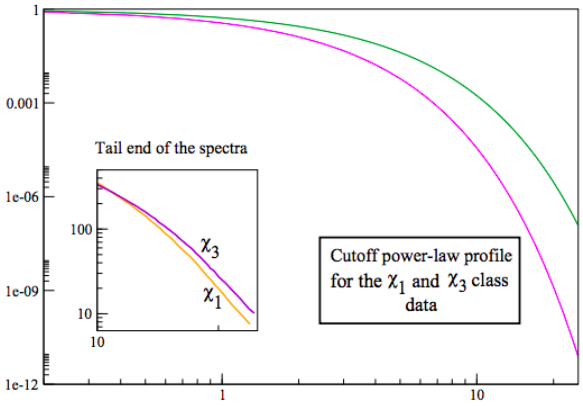

Figure 3.4: Comparison of the *Cutoffpl* profiles as obtained from the fitted parameters and tail end of the actual spectra. The relative hardness of χ_3 class as found from the fitted parameters is in agreement with the actual observation.

model in the $2.5-25.0$ keV. The disk accretion rate and the TCAF normalization over the entire $2.5-25.0$ keV range are observed to be 1.13 $\dot{M}_{Edd}$ and 2.85 respectively. These parameters are relatively lower than that of χ_1 class, which is in agreement with the higher disk flux in the case of χ_1

class (Fig. 3). However, corresponding to χ_3 class, since the sub-Keplerian accretion rate is reduced relative to the χ_1 class, the shock location moves inwards. Compared to χ_1 class, the lower α and higher β in case of χ_3 class are in conjunction with the relative hardness of χ_3 class. The spectral fitted parameters are tabulated in Table 3.2.

However, χ_3 class being spectrally harder, the spectral fitting using only TCAF could be accomplished in the $2.5 - 14.0$ keV range. The disk rate obtained in this case was found to be lower relative to χ_1 class. The normalization was obtained to be around 5.55. The normalization for TCAF was frozen at this value and the spectral fitting was repeated over the entire 2.5-25.0 band. The rest of the parameters were not found to be changing significantly from those obtained from the parameters with normalization kept free. The *Cutoffpl* parameters are in agreement with the relative hardness of χ_3 class. The lower disk rate for χ_3 class to account for the lower soft flux was ensured in this case as well. The fitted parameters are listed in Table 3.3. In Fig. 3.6(b), we provide the 1, 2 and 3σ contours of the parameters $\dot{m}_d$ and $\dot{m}_h$.

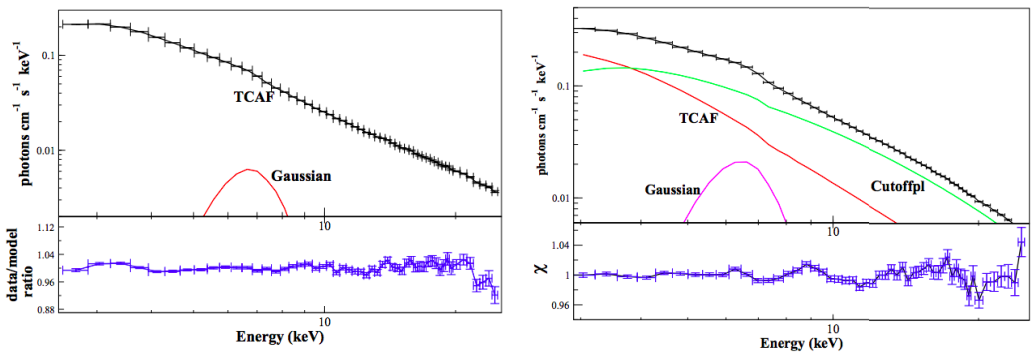

(a) (b)

Figure 3.5: (a) The data to model ratio for a fit in the χ_2 class data using *TCAF* model. A Gaussian profile is added to account for the iron line emission ~ 6.5 keV. (b) The data to model ratio corresponding to the fitted spectrum of χ_1 class using *TCAF+Cutoffpl* model. The Gaussian profile for iron Kα line emission is included.

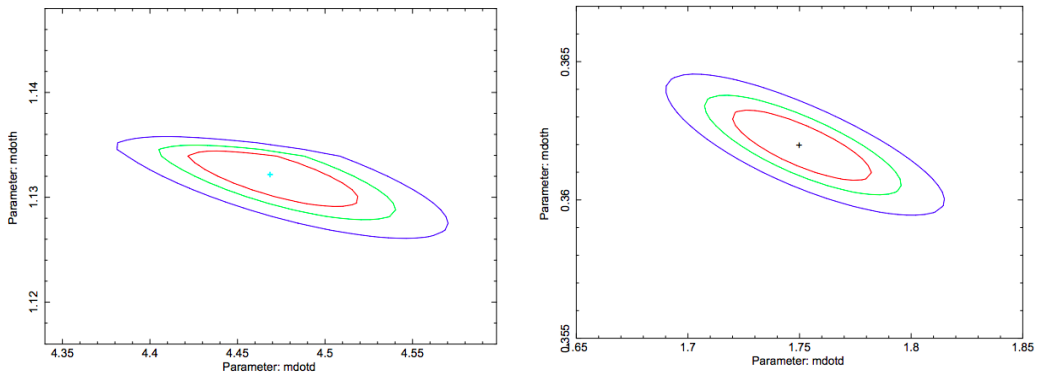

(a) (b)

Figure 3.6: The 66-90-99% confidence contours for the fitted parameters $\dot{m}_d$ and $\dot{m}_h$ in case of χ_4 and χ_1 classes respectively are shown in (a) and (b).

3.4 Summary and Discussions

In the case of $\chi_{2,4}$ classes where the outflow is not detected, acceptable spectral fitting is achieved by *TCAF+Gaussian* model only. Here, an additive Gaussian model is included to account for the Iron emission line ~ 6.5 keV. Throughout the analysis, the mass of the black hole has been kept to be a free parameter, because the mass is an intrinsic property of the black hole and can not be considered to be a flow parameter. Since we are interested to examine the evolution of flow parameters across different sub-classes, the mass is kept pegged at $14M_{\odot}$ as estimated in Greiner et al. (2001). This falls within the ballpark of a more recent estimation of $12.4^{+2.0}_{-1.8}$ $M_{\odot}$ by Reid et al (2014). We observe that flow parameters vary within a very narrow range even if the mass is changed by $\sim 15\%$. Therefore, if we fix the mass $\sim 12.4M_{\odot}$, the accretion rates change only $\sim 0.5\%$ - 0.8%. Therefore, it does not alter our conclusions.

The thermal flux (< 10 keV) in the case of χ_4 class is observed to be significantly greater. Since the thermal photons primarily contribute to the low energy end of the spectra, the disk accretion rate corresponding to χ_4 class is also found to be significantly greater. However, since the outflow is not present, normalization remains almost the same across these classes (see, Table 3.1).

Comparison of the spectral characteristics of χ_2 and χ_4 classes implies

that soft and hard fluxes are larger in the case of χ_4 class (Fig. 2). The ratio of hard (10.0-25.0 keV) to soft (2.5-10.0 keV) fluxes turns out to be ~ 0.32 and 0.63 in the case of χ_2 and χ_4 class respectively, implying larger high energy flux in the case of χ_2 class. However, the ratio of halo accretion rate and disk accretion rate in the case of χ_2 and χ_4 turns out to be 0.20 and 0.25 respectively. This apparent paradox is resolved when it is observed that the flux does not depend only on the accretion rates but on all the flow parameters, such as the shock location and shock strength. Therefore, the flux-ratios corresponding to the two classes can not be correlated with the accretion rate ratios only. In the case of a controlled system where one can change just the accretion rates keeping other parameters unaffected, such comparisons would have made sense. In our case, the shock location decreases from $\sim 47\ r_s$ to $\sim 38\ r_s$ as the source moves from χ_2 to χ_4 class. Shock strength also does not remain constant. Higher shock location and stronger shock in case of χ_2 class naturally intercepts elevated number of soft photons and consequently produce more hard photons through inverse Compton scattering. All such factors contribute to the broadband flux and hardness of the spectra. However, If we compute the contribution of TCAF in 2.5-25.0 keV, we observe that in the case of χ_4 class the flux is greater by a factor of ~ 4.8 as compared to χ_2 class. This result is in agreement with Fig. 3.2.

The spectral features of the radio-loud χ class of GRS 1915+105 have been found to be contributed by the Comptonization by a 'coronal' region of the average temperature of a few keV and optical depths of a few units (Rao et al. 2000; Trudolyubov 2001; Vadawale et al. 2003). The work done by Rao et al. (2000) resolved the χ_3 class data into multi-color disk blackbody (*diskbb*), a Comptonized component (*CompST*), and a cutoff power-law (*Cutoffpl*) by fitting the spectra with *diskbb+CompST+Cutoffpl* model. Different competing models have been proposed to account for the simultaneous presence of thermal Comptonization and an additional power-law feature. The Comptonization on the thermal and non-thermal population of electrons have also been proposed as a potential scenario (Poutanen & Svensson 1996). Such models have been applied earlier to model the spectral features in the steep power-law state of GRS 1915+105 (Hannikainen et al. 2005). It has been argued by Trudolyubov (2001) that the essential difference between the radio-loud and radio-quiet sub-classes of the χ class of GRS 1015+105 lies in the accretion flow configuration, specifically in the presence or absence of compact outflows. The simultaneous increase of the power-law flux and the

radio flux from the compact jet apparently establishes a correlation between these two. The Pearson correlation coefficient between these two fluxes had been found to be as high as 0.93 (Rodriguez et al. 2008). In Vadawale et al. (2003), it had also been suggested, based on a simple outflow model, that the additional power-law could be contributed by the synchrotron emission from the jet as well. All such findings point towards a common accretion flow configuration that is compatible with the observational findings. The high energy tail of an X-ray emitting source thus encompasses the contribution from the two different emission processes: thermal Comptonization and additional power-law emission by the physical processes associated with the jet. The final spectral energy distribution would thus be the representative of the sum of all these different emission components.

As mentioned earlier, in TCAF solution, the presence of an outflow has a natural context. In case the CENBOL region is hot enough to push the incoming matter in the direction transverse to the accretion disk, the outflow can be launched from within the CENBOL region. The launching of outflow from within the CENBOL region would be sensitive to the flow parameters. It has been shown in Chakrabarti (1999a) that outflows from CENBOL are possible in harder states and intermediate states. The process is not sensitive to the total accretion rate, but the location of the shock and the compression ratio R at the CENBOL boundary. Often high accretion rates quench the jet base and reduce the thermal pressure required for the launching of jets. In the case of $\chi_{1,3}$ class, the outflow is collimated and steady. Consequently, the inverse Comptonization of the seed photons from the base of the outflow is present and that is manifested as an additional power-law. We had to employ *Cutoffpl* model in addition to TCAF for the best spectral fitting. The two parameters α (the power-law photon index) and β (the exponential roll-off factor) dictates the strength of the outflow. From the comparison of the spectral nature of the two classes, the relative dominance of low energy flux for the χ_1 class data and also its overall relative hardness is apparent. These two features must be reflected in the spectral fitted parameters. In the $\chi_{1,3}$ class data, since the cooling within the sonic sphere is not catastrophic and there is no fallback of the outflow on the initial accreting matter, the fitted parameters must not also change over the period of observation. These are the features that were actually obtained as has been reported earlier. The disk rate as obtained in the case of χ_1 class data was dominating over χ_3 class. The lower α and higher β of χ_3 class data accounted for the relative hardness of that class.

Since the disk and Comptonized component from the CENBOL have been already incorporated in the TCAF solution, therefore only the addition of *Cutoffpl* model along with the TCAF solution should be sufficient to account for the contribution from the outflow. The result we have obtained thus vindicated our expectation. However, in order to segregate the contributions from the two components, we did the spectral fitting in two phases. Using TCAF solely, the spectra were fitted in a smaller energy range. Subsequently, the spectral analysis was repeated in the entire $2.5 - 25.0$ keV energy range with *TCAF+Cutoffpl* model keeping the TCAF normalization frozen at the average value from the earlier fitting. The values of the fitted parameters did not change significantly, and the essential relative features between the spectra of χ_1 and χ_3 class data still remained. Thus the one-to-one correspondence of the $\chi_{1,3}$ class of the object with the accretion flow configuration as depicted in Fig. 1(a,b) is justified, with the effect of Comptonization being absorbed in the *Cutoffpl* model. The relative dominance of outflow in the case of χ_3 class data is well corroborated from the α and β parameters.

From Fig. 3.5(b), we observe the *Cutoffpl* contribution starts dominating over TCAF above ~ 4 keV. However, this does not make TCAF redundant anyway. *Cutoffpl* is added to account for the power-law contributed by inverse Comptonized photons from the outflow base. The outflow, on the other hand, is launched from within the CENBOL region, which, in turn, is produced because of the interplay of accretion rates. Therefore, the accretion flow and outflow together form a complete system and the description of the system can be complete only if both of these segments are described by self-consistent models. The break in the spectral energy distribution, beyond which *Cutoffpl* starts dominating, is only representative of the relative dominance of TCAF and *Cutoffpl*. Beyond the break, the Comptonization from the outflow base or the synchrotron emission would be the dominant contributing component to the overall spectrum. Higher the contribution from these components lower would be the break energy, which we have found in χ_3 class. This is the reason why χ_3 class is associated with relative hardness.

Earlier, all the classes of this interesting source GRS 1915+105 were characterized by the Comptonizing Efficiency (CE), which is nothing but the ratio of power-law and black body photons (Pal, Chakrabarti & Nandi 2013). This is different from the standard hardness ratio because the energy domains corresponding to soft and hard photons dynamically vary from one class to another. This is a measure of geometry variation and how the CENBOL is evolving as the source transits from one class to another. Therefore, the

sequencing of CE in ascending order provides us a plausible sequence of the transition of the source from one variability class to another. On the other hand, fitting of the observed spectra using TCAF provides us a description of the accretion flow around the source in different classes in terms of basic flow parameters. In the case of TCAF, the soft and hard fluxes are not calculated separately. Rather, all the flow parameters contribute to fit the observed spectral energy distribution. For this reason, the individual flow parameters or their ratios cannot be connected to the CE of respective classes. Rather, all the flow parameters are important for a meaningful description of each individual sub-classes. Also, the incorporation of associated phenomenological models like cutoff power-law can provide us information regarding the strength of the outflow present in different sub-classes. Therefore, spectral fit using physical models TCAF provides us a deeper understanding of the characteristics of different sub-classes in terms of accretion flow dynamics.

Chapter 4

Spectral and Timing Analysis of the θ Class Data of GRS 1915+105

4.1 Introduction

In Chapter 3, we presented our analysis regarding the spectral and temporal properties of χ class data, which is non-variable. It was observed that even within such a non-variable class, there could be huge intensity variations from one sub-class to another sub-class and some of the spectro-temporal features could be explained by invoking the idea of the accretion-ejection mechanism in the inner region of the accretion flow. However, as we have mentioned earlier, GRS 1915+105 is well known for its large varieties of structured variabilities of different time-scales, and embarking on the spectro-temporal analysis of such variable classes is particularly important to obtain a comprehensive understanding of the accretion flow dynamics around this spectacular object.

It was suggested by Belloni et al. (2000) that in the case of GRS 1915+105, the transition between all the different variability classes may be thought to be due to the transition among three basic states — A, B and C. The states A and B are identified by spectral softness, the only difference being the inner disk temperature of B is comparatively higher than that of A. In the case of C, the spectrum is dominated by a hard power-law component and the inner disk region is practically non-existent. The description of the

spectral and temporal behavior of GRS 1915+105 as a transition between these three fundamental classes is a unique feature of this object itself and is markedly different from the standard transient source behaviors (Tanaka & Lewin 1995b). Qualitative physical pictures of these states and other possible states of the variability class transitions were presented immediately (Chakrabarti & Nandi, 2000; Nandi, Manickam & Chakrabarti 2000b).

The state C or harder state is characterized by the appearance of 1–15 Hz QPOs. The in-depth investigation regarding the genesis of these mid-frequency QPOs of GRS 1915+105 by Markwardt et al. (1999) yielded that QPOs are generally present during hard dips in the flaring states. The frequency of oscillation is also found to be strongly correlated with the soft flux. With the reduction of power-law flux and the steepening of the spectral slope towards the end of the hard dips, the QPO disappears as well, suggesting the presence of two spectral components in interaction. Chakrabarti & Manickam (2000) showed that the QPO frequency can be explained by the radial oscillation of the post-shock region. The oscillation between the soft X-ray domain (burst-on states) to spectrally hard dips (burst-off states) as well as the meantime of residence in those states could be explained by consideration of outflow from the post-shock region. It had been further observed that QPOs are prominent for non-thermal photons (4.0-13.0 keV), but remain undetected for thermal photons (0-4.0 keV). This observation is clearly indicative of the fact that the QPO phenomenon is predominantly manifested by Comptonized photons (Rao et al. 2000). Energy resolved analysis on the low-frequency QPOs of GRS 1915+105 using RXTE data further establishes the fact that inverse Comptonized photons by the 'corona' contribute to the QPO generation and its frequency variation is strongly correlated with thermal flux (2.0-5.0 keV) (Rodriguez et al., 2002). However, it was observed during the analysis of α and β classes of GRS 1915+105 that QPO frequency changes during the transition through hard dips, where the soft X-ray flux remains unchanged (Mikles, Eikenberry & Rothstein, 2006). This further establishes the broad correlation of QPO frequency and power-law flux indicated by Markwardt et al. (1999) as well, which gradually weakens towards the latter half of the dip. It had, however, been argued that the two spectral components cannot really be disentangled. This was concluded by the spectro-temporal analysis on GRS 1915+105 by Rodriguez et al. (2008) to study the energy dependence of Low-Frequency QPO (LFQPO) in the hard intermediate state. The importance of both of the components had also been highlighted during energy-resolved LFQPO analysis to pinpoint the origin of

QPO as well (Vadawale et al. 2001; Rao et al. 2000).

Several attempts have been made so far by different groups to determine the origin of QPOs in general. The proposed mechanisms include relativistic precessions of encircling matter due to misalignment of the black hole spin axis and the inner edge of the accretion disk (Stella & Vietri 1998; Ingram et al. 2009) as well as instability in the inner disk region (Tagger & Pellat 1999). Fitting the phase-resolved spectra using Comptonization, edge smearing, and Gaussian equivalent width model, Ingram & van der Klis (2015) suggested the geometric origin of the QPOs.

All of these features, however, come naturally if one considers the presence of two accretion flow components: high angular momentum Keplerian flow and low angular momentum sub-Keplerian flow as incorporated in TCAF (Chakrabarti 1995; Chakrabarti & Titarchuk 1995, Chakrabarti 1996). It was shown by Chakrabarti and his collaborators that the resonance oscillation of the shocked surface can produce the observed low-frequency QPOs (Molteni et al. 1996; Chakrabarti et al. 2015). If the cooling time-scale in the CENBOL roughly matches with the infall (i.e., compressional heating) time-scale from the shock front, the resonance oscillation of the shock-surface is triggered. The frequency of oscillation depends on the shock distance from the black hole and the shock strength (Chakrabarti & Manickam 2000), which in turn, is determined by the viscosity in the sub-Keplerian flow. Therefore, the intensity variation corresponding to the source would be a manifestation of the accretion rate evolution and the relative dominance of the two accretion rates (Keplerian disk rate and sub-Keplerian halo rate) would dictate the spectral state of the source.

Satellites having broadband coverage play an important role in providing an opportunity to perform both the spectral and the temporal analysis over a wide frequency interval to gather a comprehensive understanding regarding the accretion flow mechanisms around accreting objects. The Indian satellite *AstroSat* offers such simultaneous observational facility in 0.3-100.0 keV owing to its co-aligned instruments: Large Area X-ray Proportional Counter (LAXPC) (Yadav et al. 2016a,b; Antia et al. 2017), Soft X-ray Telescope (SXT) (Singh et al. 2017) and Cadmium Zinc Telluride Imager (CZTI) (Vadawale et al. 2015). The spectral and timing analysis on θ class using LAXPC provided us some very important clues regarding the connection between spectral and temporal phenomena and the underlying accretion flow mechanism.

We will be describing in this chapter the spectro-temporal analysis on

the θ class data from a small subset of *AstroSat* Target of Opportunity (ToO) observation on March 4, 2016 by on-board LAXPC instrument. We investigate the evolution of the spectral and temporal behavior and the QPOs (if observed), and derive the underlying accretion flow parameters to explain the observed evolution. In the next section, we present some of the techniques employed in the analysis of our data. The detailed results of timing and spectral analysis would be discussed subsequently.

4.2 Observation and Data Reduction

The spectro-temporal studies on transient X-ray sources using the AstroSat LAXPC data have been performed earlier. (Yadav et al. 2016a, Misra et al. 2017, Pahari et al. 2017, 2018). LAXPC instrument consists of three identical but independent X-ray Proportional Counters which gather photons in 3.0–80.0 keV with a time resolution of 10μs (Yadav et al. 2016a, 2016b; Agrawal et al. 2017). We have carried out our analysis on the basis of instructions provided in the LAXPC analysis software `LaxpcSoft` released on May 16, 2019[1]. The details of the data analysis procedure using background and response matrices are provided by Antia et al. (2017).

Notwithstanding the wealth of data of RXTE on GRS which are available for general usage, there are certain advantages in using AstroSat data. The effective area of RXTE PCA falls quickly with increasing energies. Around 30 keV, the effective area of LAXPC ($\sim$ 4500 cm^2) is significantly higher as compared to RXTE PCA ($\sim$ 1000 cm^2) (Yadav et al. 2016b, Table 1). Further, the time resolution of the standard 2 mode data in RXTE (used for spectral analysis) is 16 seconds, while LAXPC gathers event mode data at high time resolution (10μs) which is very useful in the analysis of highly variable sources. For the purpose of our analysis, ToO level 1 data was obtained from the ISSDC data distribution archive [2]. Only the data from LAXPC10 among the three LAXPC detectors were used in our analysis. LAXPC20 had a gas leakage and consequent abrupt gain changes and therefore it was not used in our analysis. This unit had ultimately been switched off on March 8, 2018. GRS 1915+105 being a luminous source, we are getting normalized photon counts few thousands/s. Therefore, statistically significant results could be obtained using one LAXPC instrument only. There are certain dif-

[1]https://www.tifr.res.in/ astrosat_laxpc/archived.html

[2]https://astrobrowse.issdc.gov.in/astro_archive/archive/Home.jsp

ferences between the two detectors (LAXPC10 and LAXPC20) as well. The number of consecutive channels to be added to extract the raw data (to account for the even-odd fluctuations) are different (2 for LAXPC10 and 4 for LAXPC20). This implies that the total number of channels to be considered in LAXPC10 and LAXPC20 are 512 and 256 respectively (Anita et al. 2017). Further, there is also a small gain mismatch between the two instruments.

For the spectral analysis, the source and background spectra have been produced separately using standard procedure. The corrections for South Atlantic Anomaly (SAA), the Earth occultation, and the dead time are carried out using LAXPC software. In order to avoid the undesirable contribution from the instrumental artifact, namely, a bump at $\sim$ 33 keV (Antia et al. 2017), only the data in 4.0-25.0 keV has been considered for our analysis. Data from all the anodes in the detector have been used to enhance the signal component.

In the entire $\sim$ 67 ks of LAXPC10 exposure, the accumulated data were spread over nine consecutive satellite orbits (02345–02354) starting from 04 March 2016, 11:22:15 to 05 March 2016, 04:54:23. All the lightcurves in θ class (Belloni et al. 2000) repeatedly exhibit an 'M' shape of a few hundred seconds duration, such that the photon intensity follows the fast decay and exponential increase profile. We have selected 'U'-shaped regions in the 'M' shaped θ class data of two initial AstroSat orbits, i.e., 02345 and 02346 (Fig. 4.1(a,b)). In orbit no. 02345, this phase spans over 460s starting from the onset of observation (Fig. 4.1(a)), and in the following orbit, this steady rising phase spans over a wider time interval of $\sim$ 800 s (Fig. 4.1(b)). The start times of observation in the first and the second orbit correspond to UT 12:01:26 and UT 13:42:14 on the 04 March 2016 (MJD = 57451.501 and 57451.571 respectively). In our analysis we treat these times as $t_0 = 0$.

For the first orbit, the photon flux in the entire interval varied from $\sim$ 2700 counts/s to $\sim$ 7000 counts/s (Fig 1(a)). In the case of the second orbit, the same thing varies from $\sim$ 2000 counts/s to $\sim$ 9000 counts/s (Fig 1(b)). Dynamic power spectra were produced in order to detect any continuous systematic variation of the timing behavior of the source during its evolution from low-intensity dips to high-intensity flares. The individual power-density spectrum (PDS) in the 4.0–25.0 keV for 100-second time span is generated using the standard FTOOLS task "powspec" with a suitable normalization (equals to -2) to eliminate the white-noise background. For the purpose of the analysis, we extracted lightcurves of 0.01 second time resolution, which corresponds to the Nyquist frequency of 50 Hz. Each lightcurve was divided

into 4096 time bin intervals, and then PDS was created for each interval. Final PDS was obtained by averaging over all these individual PDS. The average PDS was binned with bin size increasing by the geometric factor of 1.03 in frequency space. In the generation of dynamic PDS, the origin of each successive PDS is shifted by 1 second compared to its previous one. The PDSs are plotted in 3D color map with a suitable color palette.

In the dynamic PDS, a significant concentration of power is observed within a narrow frequency band for a certain span of observation. Individual PDS were extracted with suitable time resolution and time bin intervals in order to search for the plausible peaked component on top of the broadband noise. The details are provided in Section 3.2. The PDS were fitted using Lorentzian and power-law components in order to take care of the peaked component and the broadband component of the noise respectively. Specific attributes corresponding to the peaked component, viz. the centroid frequency, Q factor, and contributed RMS power were determined from the fitted parameters. The error values were determined using the built-in 'fit err' method.

Within the region of our interest in both orbits, the photon count increased significantly. During the spectral analysis, the entire domain is split into sub-domains depending on the intensity variation. In the case of the first orbit, the domain of analysis is split into five sub-domains: the first one is the 60 seconds interval containing the declining phase, and the other four are 100 seconds intervals in the subsequent rising phase of 400 seconds. In the case of the second orbit, the rising phase of $\sim$ 700 seconds is split into equal sub-intervals of 100 seconds each. In order to connect this spectral variation with the accretion flow dynamics, individual spectra had been fitted using phenomenological and physical models and fitted parameters are extracted. During the entire span of observation, the hydrogen column density (N_H) is kept fixed at 6.0×10^{22} cm^{-2} (Muno et al. 1999) and is modeled using the absorption model *phabs*. In order to obtain a quantitative measure of the shift in spectral hardness, each background subtracted spectrum is fitted using *phabs*(diskbb+power-law)* model. Subsequently, in order to have a physical picture of the accretion flow, we analyze the same spectra using *phabs*TCAF* as well. For this purpose, TCAF based model *fits* file is used (`TCAF_v0.3.2_R1.fits`). Four flow parameters (a–d) and one system parameter (e) were used to achieve the best fit: (a) Keplerian disk accretion rate, $\dot{m}_d$ (in units of $\dot{M}_{\rm Edd}$), (b) sub-Keplerian halo accretion rate, $\dot{m}_h$ (in units of $\dot{M}_{\rm Edd}$), (c) location of the shock front X_s (in unit of Schwarzschild

radius $r_g = 2GM/c^2$), (d) the compression ratio of the shock R and (e) mass of the black hole (in unit of solar mass $M_\odot$). In order to obtain the best fit, we used a broad Gaussian profile as well to take care of Iron line emission. A 2% systematic error is applied for achieving the best fit (see, Pahari et al. 2017), and XSPEC command 'err' is used to obtain 90% confidence error values for the spectral model fitted parameters.

4.3 Results

4.3.1 Nature of the Lightcurve

The intensity variations corresponding to the orbit nos. 02345 and 02346 are shown in Figures 1(a) and 1(b) respectively, where the respective domains of our timing analysis are clearly marked. In the case of the first orbit, the left-hand side of the vertical line indicates the domain within which we have done timing analysis. For $\sim$ 60 seconds after the beginning of the observation, the photon count rate decreases. Subsequently, for $\sim$ 100 seconds, the count rate remains almost steady, and then it monotonically increases for $\sim$ 300 seconds. In the following orbit, we have chosen only the declining and subsequent rising phases from the middle segment of the observation. Within a span of $\sim$ 700 seconds, the photon count rate varied between $\sim$ 2000 counts/s and $\sim$ 7000 counts/s.

4.3.2 Timing Analysis

For the timing analysis, we have generated the dynamic PDS for different domains of observation in both of the orbits. The dynamic PDS has been generated by staggering individual PDS of 100 seconds each, such that the origin of each successive time-series advances by one second. In Fig. 4.2(a), we show the dynamic PDS for the first 460 seconds of observation in orbit no. 02345 to investigate the presence of some frequency domain where the power is concentrated. The x-labels stand for the mid-point of the respective time windows chosen for the generation of dynamic PDS. We observe two modes of oscillation contributing significantly to the overall power. The strongest mode of oscillation is observed $\sim$ 4–5 Hz, which is the key focus of our paper, though there is another low-powered and lower frequency mode of oscillation at $\sim$ 2 Hz in the first $\sim$ 250 seconds as well. With the passage of

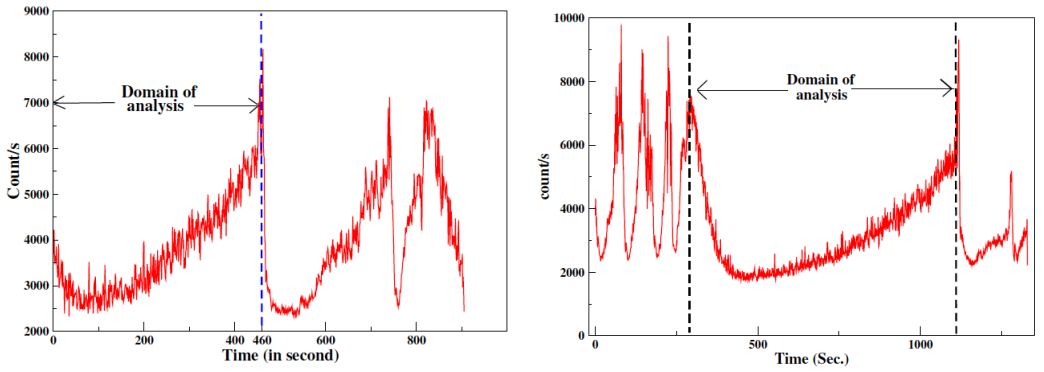

(a) (b)

Figure 4.1: (a) In the left panel, the domain of analysis corresponding to the orbit no. 02345 is indicated. For the purpose of our spectral and timing analysis, we took the first 460 sec of data, namely the U-shaped curve of θ class. In the first 60 seconds, the photon count is declining, after which it is monotonically increasing. All the time-stamps are relative to t_0 (MJD = 57451.501).(b) In the right panel, the domain of analysis corresponding to orbit no. 02346 is indicated. The time-stamps are relative to $t_0 = 57451.571$.

time, we observe a slight drift in this peaked component. The dynamic PDS generated using the same procedure from the data marked in Fig. 4.1(b), is shown in Fig. 4.2(b). The upward trend in the peaked component is apparent here as well.

In order to observe the behavior of the peaked components in the PDS during the sharp declining phases of the two orbits more closely, we generated the dynamic PDS corresponding to that domain separately. The presence of only 60 seconds long duration of the declining phase in case of orbit no. 02345 and sharp decline within $\sim$ 100 seconds in case of the the following orbit required the generation of individual PDS for shorter time intervals to detect peaked components on top of the broad-band noise. With 100 seconds intervals, the PDS is not statistically significant for making any conclusion. Therefore, shorter individual data blocks had been considered for dynamic analysis with a larger number of 'newbin' intervals to prune unwanted noise components. The data corresponding to this declining phase was extracted with the time resolution of 0.001 seconds for the purpose of generation of dynamic PDS. Each individual data block was considered to be of 16 seconds

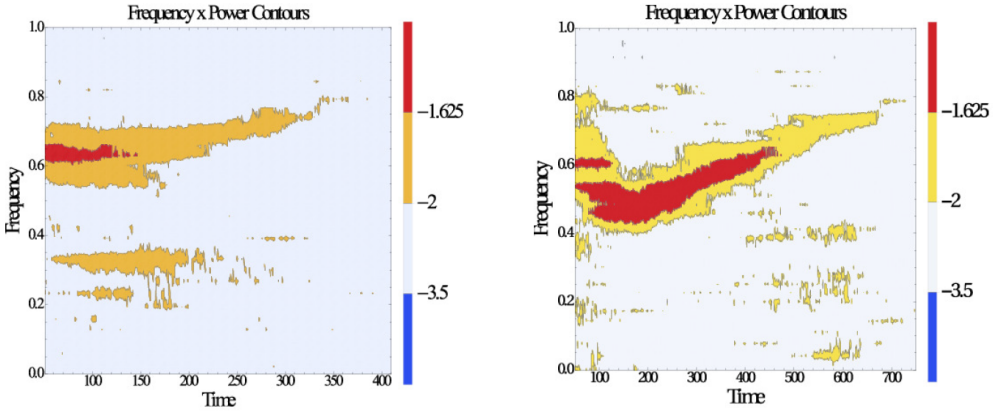

(a) (b)

Figure 4.2: (a) Power Density Spectra (PDS) for the first 460 seconds of observation in the orbit no. 02345. x-axis is observation time in second (with t_0 at MJD = 57451.501), y-axis is Fourier transformed frequency (in Hz) and color bars represent the logarithm of frequency multiplied by power. y-axis and color bar are depicted in $\log_{10}$ unit. The strongest mode of oscillation has been found to be around 4 Hz and that mode is conspicuous for about the first 225 seconds. This domain has been chosen for spectral analysis. Apart from that, the low-frequency oscillation at $\sim 2Hz$ is also obtained. (b) Corresponding to orbit no. 02346, we have shown the dynamic PDS for the entire domain of our analysis as indicated in Figure 1(b). The origin stands for 300 seconds after the initiation of observation for the orbit no. 02346 (MJD 57451.574). The low-frequency oscillation mode is absent and the strongest mode of oscillation lies around $3 - 4$Hz.

duration, and the origin of each successive data-segment was advanced by 1 second. The time resolution and the number of newbins per sub-interval are kept to be respectively 0.008 second and 512 so that the final PDS generated on one frame is averaged over four consecutive realizations. Fig. 4.3(a,b) features the dynamic PDS for the declining arm corresponding to the two orbits 02345 and 02346 respectively. For 02345, the power is concentrated between 4-5 Hz during this entire phase. In the case of 02346, however, we observe a conspicuous downward trend in the peaked component in frequency space. We investigated individual PDS to search for the presence of a strong peaked component over the broadband noise. For orbit no. 02345, a closer

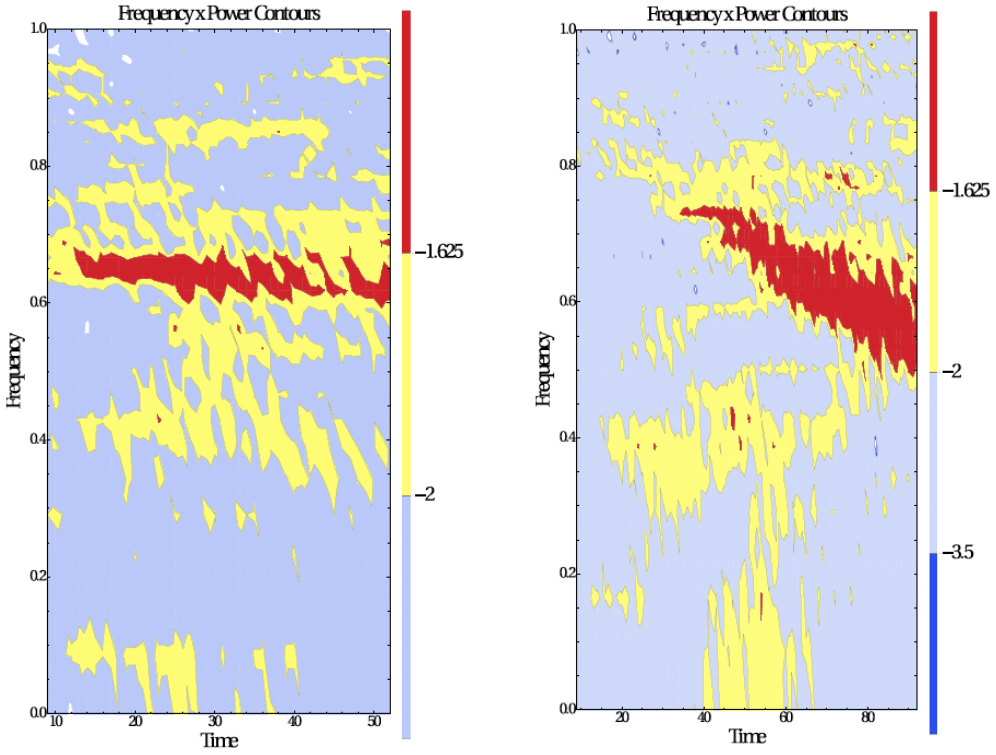

(a) (b)

Figure 4.3: (a) Power Density Spectra (PDS) for the first 64 seconds of observation corresponding to the orbit no. 02345. x-axis represents the observation time in second (with t_0 at MJD = 57451.501), y-axis is Fourier transformed frequency (in Hz). The color bar represents frequency multiplied by power. Both y-axis and color bar is provided in $\log_{10}$ unit. The x-labels stand for the midpoint of corresponding data-blocks. The strongest mode of oscillation has been found to be within 4-5 Hz. (b) The dynamic PDS corresponding to the fast declining phase in the domain of our analysis as indicated in figure 1(b) is shown. The time-stamps are relative to the t_0 of orbit 02346 (= MJD 57451.571), i.e. MJD 57451.574. The declining trend in the peaked component from 30 seconds onward is apparent.

look at the individual PDS yields the presence of such peaked components in the first 225 seconds of observation, starting from the onset of the rising arm of the U-shaped curve of our interest. In the case of the following orbit, the

Table 1

Orbit no.	Time segment (Second)	QPO frequency (Hz)	Q Value	RMS (%)
	50-150	4.22 ± 0.05	10.0 ± 0.2	7.3 ± 0.2
02345	75-175	4.27 ± 0.05	12.7 ± 0.2	6.7 ± 0.3
	100-200	4.41 ± 0.04	7.6 ± 0.1	7.3 ± 0.2
	125-225	4.51 ± 0.09	11.3 ± 0.1	5.6 ± 0.3
	332-348	5.39 ± 0.04	6.0 ± 0.1	6.5 ± 0.3
	348-364	4.87 ± 0.03	3.8 ± 0.1	8.9 ± 0.3
	364-380	4.20 ± 0.04	7.9 ± 0.1	11.5 ± 0.3
	380-396	3.69 ± 0.05	3.7 ± 0.2	11.9 ± 0.2
	400-500	2.90 ± 0.05	7.8 ± 0.2	9.4 ± 0.3
	425-525	2.98 ± 0.03	8.3 ± 0.1	11.4 ± 0.3
	450-550	3.02 ± 0.05	6.7 ± 0.2	11.0 ± 0.3
	475-575	3.11 ± 0.03	8.7 ± 0.1	9.5 ± 0.3
	500-600	3.25 ± 0.04	5.7 ± 0.2	10.8 ± 0.2
02346	525-625	3.38 ± 0.04	6.0 ± 0.1	9.4 ± 0.2
	550-650	3.56 ± 0.05	5.9 ± 0.1	9.2 ± 0.2
	575-675	3.77 ± 0.06	5.7 ± 0.1	9.2 ± 0.2
	600-700	3.81 ± 0.06	6.2 ± 0.1	10.1 ± 0.3
	625-725	3.92 ± 0.05	6.2 ± 0.1	9.4 ± 0.2
	650-750	4.05 ± 0.07	8.6 ± 0.2	7.7 ± 0.2
	675-775	4.28 ± 0.09	8.1 ± 0.1	5.8 ± 0.3
	700-800	4.33 ± 0.06	5.2 ± 0.1	6.3 ± 0.3

peaked component is observed in the first 400 seconds of observation during the monotonic increase of the photon flux in the rising arm.

The PDS are fitted with the combined Lorentzian and power-law models to account for the peaked (QPO) component and broadband noise respectively. The corresponding parameters quantifying the peaks, namely the centroid frequency, the RMS power and Q-factor (= centroid frequency/FWHM) are determined. In the case of the first orbit, during the declining phase, the centroid frequency was found to be around 4.3 Hz, with RMS power varying in the range 7.5% - 9.2%. Q factor was found to be more than 5 during the entire transition. During the rising phase, centroid frequency drifted from 4.22 Hz to 4.51 Hz. The Q factor was observed to be varying between 7.6 and 12.7. This high Q factor indicates that those peaks can be qualified as

QPOs. The RMS power dropped from 7.3% to 5.6%. Details of the analysis are provided in Table 1. A typical Lorentzian model fit around QPO frequency is shown in Fig. 4.4(a). We fit the lower frequency QPOs using

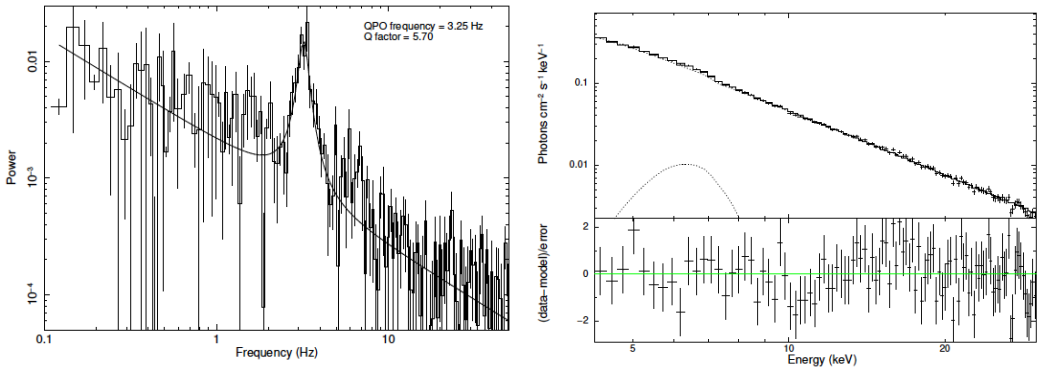

(a) (b)

Figure 4.4: (a) Power density spectrum obtained during 500–600 seconds interval in orbit no. 02346. From the Lorentzian fitting, the QPO frequency turned out to be 3.25 Hz and Q factor was found to be 5.70. The RMS power contributed was 10.79%. (b) 4.0–25.0 keV *phabs*(TCAF+Gaussian)* fitted unfolded spectrum with residue for the 0–60 second observation for orbit no. 02345.

Lorentzian profiles as well. The centroid frequency varied within the range 2.05 Hz - 2.13 Hz, with the Q-factor in the range 6.5 - 7.0. The RMS power contribution was found to be $\sim$ 7%. Apart from the principal contribution at around 4 Hz, the presence of another mode of oscillation at a lower frequency is also detected in our observation. The 4 Hz QPO appears not to be a harmonic of the 2 Hz QPO. The 4 Hz QPO is more prominent, sharper and the normalization is higher. The dynamic PDS also suggests that power is predominantly concentrated around 4 Hz. However, detailed exploration regarding the characteristics and the physical origin behind the subdominant peaked components merits more extensive investigation altogether and falls outside the scope of the present discussion.

In the following orbit, the QPO frequency during the declining phase is reduced from 5.39 Hz to 2.90 Hz in a span of $\sim$ 100 seconds. Q value resides between 3.8 and 7.9 during this period, with RMS power varying from 6.51% to 11.87%. In the rising arm, on the other hand, centroid frequency increases

from 2.90 Hz to 4.33 Hz during the domain of investigation. We did not obtain any consistent trend either in the Q value or RMS power. The Q factor resides in the range of 5.2 to 8.7 and the RMS power is observed to vary between 5.8% and 11.4%. The details of the parameters, i.e., the QPO frequency, Q-value, and RMS power are noted in Table 1.

4.3.3 Spectral Analysis

The dynamic spectra for both the orbits in their entire observation span are shown in Fig. 4.5(a,b). In order to produce the dynamic spectrum, the individual spectra of 25 seconds duration are produced and the origin of each successive data block has been advanced by one second. The constant intensity contours repeatedly showed the same pattern across different U-shaped intervals. Therefore, spectral variation within one U shape could be considered to be representative of the variation across the orbit. Hence, in order to extract a quantitative estimate of the dynamics of flow parameters with the evolution of time, fitting of individual spectra using empirical and physical models have been performed only within the first U-shaped curve in the first orbit and the prominent U-shaped curve in the second segment of the second orbit. For the orbit no. 02345, for the first ~ 60 seconds, the count rate gradually goes down and becomes steady for ~ 100 seconds. In order to determine the flow parameters in all these different domains, the data have been split into five segments. The first segment comprises of $0 - 60$ seconds data where the count rate is decreasing. Within 160–460 seconds interval where the photon count rate is almost monotonically increasing. The entire observation span has been split into four segments and analysis has been carried out on individual segments.

The power-law photon index changes from 2.60 ± 0.06 to 2.54 ± 0.07, indicating gradual spectral hardening during this short interval. Subsequently, the spectra softened as the photon index rose up to as high as 3.014. In order to derive a quantitative estimation of this transition in terms of physical accretion flow parameters like accretion rate and shock location, we further undertook the spectral analysis using *TCAF+Gaussian* model. The variation of flow parameters in *TCAF+Gaussian* model in 4.0–25.0 keV, namely disk rate ($\dot{m}_d$), halo rate ($\dot{m}_h$) and shock location (X_s) corroborate with the results obtained from the empirical results. With the softening of the spectra, the disk rate increases and the shock location moves towards the black hole as depicted in Table 2. During our spectral fitting using TCAF,

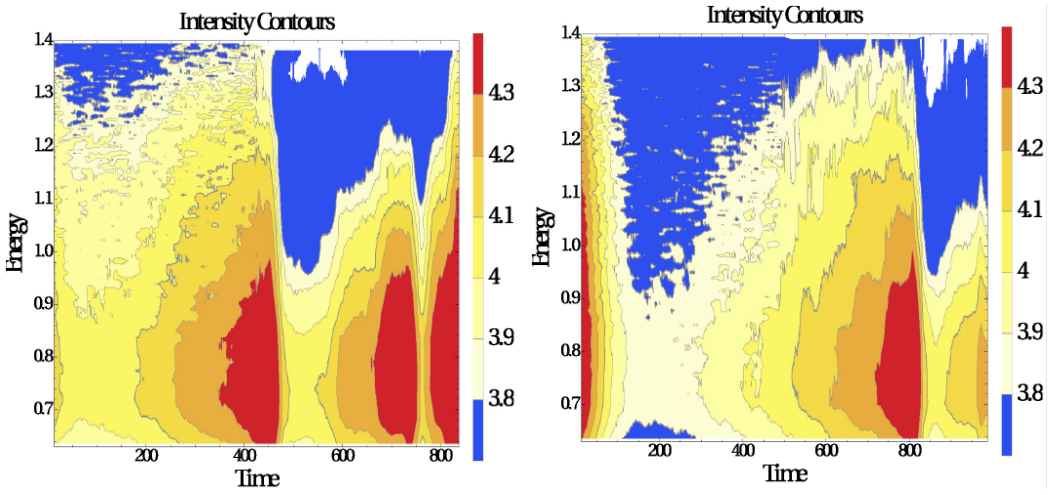

(a) (b)

Figure 4.5: (a) The dynamic spectrum for the entire range of the orbit no. 02345 is shown. The contours of constant intensity show similar patterns in different U-shaped branches of θ class. (b) Dynamic spectra for $\sim$ 1000 seconds starting from the onset of the U-shaped region as indicated in Figure 1(b). Within the domain of analysis, the constant intensity contours indicate the gradual softening of the spectra.

the mass is kept frozen at $14.0 M_{\odot}$. Within the first 60 seconds, the disk accretion rate goes down from 0.79 $\dot{M}_{\rm Edd}$ to 0.77 $\dot{M}_{\rm Edd}$, and consequently the shock location also recedes from 33.8 r_s to 38.9 r_s. For the next 400 seconds, the disk accretion rate steadily increases from 0.77 $\dot{M}_{\rm Edd}$ to 0.84 $\dot{M}_{\rm Edd}$. The shock location also decreases from 38.9 r_s to 16.9 r_s within this time span, which is as per our expectation. This corresponds to the shock velocity of $\sim$ 2200 m/s. This agrees with our finding of the rapid increase of the accretion rate in the disk. This is possible only if the effect is local and the supply at the outer edge remains unaffected. The details of the analysis are provided in Table 2. TCAF model fitted unfolded spectrum for 0–60 seconds of observation is given in Fig. 4.4(b). In Fig. 4.6, we show the default 68-90-99 percent confidence contours of TCAF fitted parameters $\dot{m}_d$ with $\dot{m}_h$ and $\dot{m}_d$ with X_s.

In the case of the second orbit, we have done the spectral fitting only in the U-shaped region where the photon count rate first decreases very

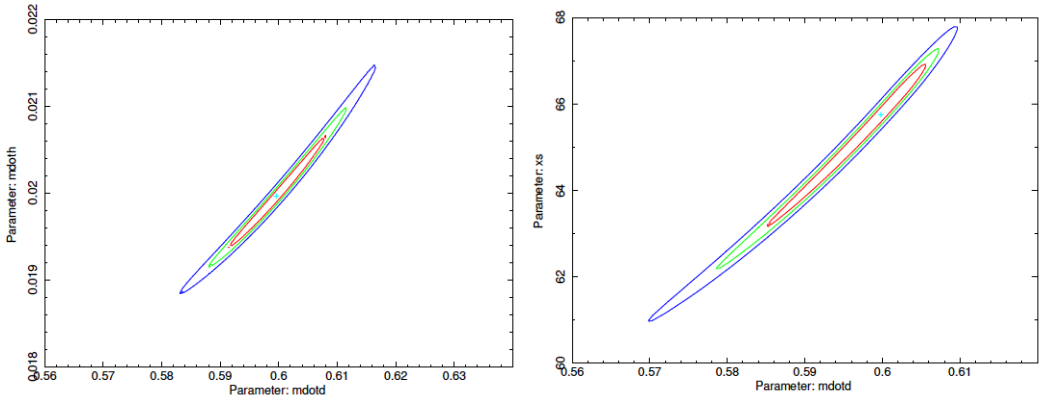

(a) (b)

Figure 4.6: (a) Default 68-90-99 percent confidence contours for TCAF fitted parameters $\dot{m}_d$ and $\dot{m}_h$ are shown for the 400-500 second interval in orbit no. 02346. (b) Confidence contours for the same observation shown for $\dot{m}_d$ and X_s.

Table 2

Orbit no.	**Time segment (Second)**	$\dot{m}_d$ $(\dot{M}_{Edd})$	$\dot{m}_h$ $(\dot{M}_{Edd})$	X_s (r_s)	**R**	Γ	χ^2/DOF
	0-60	$0.787^{+0.047}_{-0.044}$	$0.082^{+0.005}_{-0.004}$	$33.754^{+0.096}_{-0.048}$	$1.457^{+0.002}_{-0.001}$	$2.602^{+0.044}_{-0.044}$	74.59/79
	60-160	$0.772^{+0.027}_{-0.028}$	$0.074^{+0.003}_{-0.003}$	$38.884^{+0.314}_{-0.117}$	$1.496^{+0.002}_{-0.001}$	$2.546^{+0.038}_{-0.038}$	79.09/79
02345	160-260	$0.779^{+0.054}_{-0.053}$	$0.077^{+0.001}_{-0.004}$	$33.903^{+0.140}_{-0.058}$	$1.487^{+0.001}_{-0.001}$	$2.605^{+0.037}_{-0.037}$	57.49/79
	260-360	$0.793^{+0.039}_{-0.038}$	$0.108^{+0.002}_{-0.002}$	$24.151^{+0.065}_{-0.064}$	$1.372^{+0.001}_{-0.002}$	$2.539^{+0.034}_{-0.034}$	58.32/79
	360-460	$0.839^{+0.058}_{-0.058}$	$0.107^{+0.002}_{-0.001}$	$16.939^{+0.048}_{-0.047}$	$1.503^{+0.001}_{-0.001}$	$3.014^{+0.033}_{-0.033}$	68.11/79
	400-500	$0.599^{+0.034}_{-0.033}$	$0.020^{+0.002}_{-0.001}$	$65.837^{+0.061}_{-0.062}$	$1.222^{+0.002}_{-0.002}$	$2.475^{+0.034}_{-0.038}$	95.71/79
	500-600	$0.658^{+0.043}_{-0.047}$	$0.020^{+0.001}_{-0.002}$	$61.390^{+0.070}_{-0.072}$	$1.231^{+0.002}_{-0.001}$	$2.542^{+0.055}_{-0.051}$	103.52/79
	600-700	$0.676^{+0.055}_{-0.054}$	$0.020^{+0.001}_{-0.001}$	$60.351^{+0.088}_{-0.084}$	$1.232^{+0.001}_{-0.001}$	$2.516^{+0.044}_{-0.047}$	103.97/79
02346	700-800	$0.750^{+0.067}_{-0.062}$	$0.021^{+0.001}_{-0.001}$	$58.378^{+0.076}_{-0.071}$	$1.264^{+0.001}_{-0.001}$	$2.652^{+0.057}_{-0.058}$	100.38/79
	800-900	$0.766^{+0.077}_{-0.075}$	$0.022^{+0.002}_{-0.001}$	$56.031^{+0.084}_{-0.081}$	$1.285^{+0.001}_{-0.001}$	$2.707^{+0.039}_{-0.041}$	75.30/79
	900-1000	$0.767^{+0.047}_{-0.045}$	$0.023^{+0.001}_{-0.001}$	$55.671^{+0.067}_{-0.061}$	$1.543^{+0.001}_{-0.001}$	$2.759^{+0.049}_{-0.045}$	82.72/79

rapidly and then increases slowly. The *diskbb+power-law* fit in a span of 500 seconds, shows a monotonic increase in the power-law slope, indicating a possible transition towards the softer state. The disk rate increases from 0.60 $\dot{M}_{\rm Edd}$ to 0.77 $\dot{M}_{\rm Edd}$, and consequently the shock location goes down from 65.8 r_s to 55.7 r_s during this period. The corresponding shock velocity turns out to be $\sim$ 900 m/s. The details of the fitted parameters are shown in Table 2.

4.4 Summary and Discussions

So far, we have discussed our analysis of the spectral and timing properties of GRS 1915+105 in its θ class under the TCAF paradigm. The archival data of the source has been obtained by the LAXPC instrument of AstroSat satellite. In order to explain the emergence of different spectral states, as well as the QPOs resulting from resonance oscillation of the Compton cloud, the concept of the interplay between two types of accretion rates, namely, the Keplerian disk rate ($\dot{m}_d$) and the sub-Keplerian halo rate ($\dot{m}_h$) was found to be crucial. The shocks in the sub-Keplerian flow are formed depending upon the satisfaction of the Rankine-Hugoniot condition (Chakrabarti 1989, 1996; Chakrabarti & Das 2004). If the Keplerian disk rate increases, it increases the soft seed photons and the post-shock region (CENBOL, which acts as a 'Compton cloud') is cooled down rapidly, causing the shock to proceed towards the black hole. This has indeed been obtained in our spectral analysis. In the process, both the compressional heating time scale and the cooling time scale of the CENBOL go down and become comparable (Chakrabarti et al. 2015), triggering the resonance oscillations which manifests as a QPO in the light curve. We first obtained the state of the system by estimating the photon index using *phabs*(diskbb+power-law)* model. Throughout the span of our analysis, the photon index (Γ) was found to be above 2.4, implying that the source was either in the soft intermediate state (SIMS) or soft state (SS). In the case of both of the orbits, the monotonic increase pf Γ with the increase of photon flux indicates the transition from SS to SIMS. In the first orbit, Γ made an excursion from 2.5 to 3.0 during the 400 seconds span of spectral analysis, indicating the transition of the source from SIMS to SS. The gradual enhancement of disk accretion rate and the consequent decline of shock location were also obtained from TCAF model fitting. The shock location moves from $39r_s$ to $17r_s$ while the disk accretion rate increases from

0.77 to 0.84 $\dot{M}_{\rm Edd}$. A similar trend was followed in the second orbit as well (Table 2). In the two orbits (02345 & 02346) we have analyzed, within a span of 400–500 seconds, the total flux changes by a factor of 3–5. The corresponding shock velocity turns out to be $\sim$ 2200 and 900 m/s respectively. This is significantly larger compared to the shock velocity obtained earlier in the case of transient sources, which reside in the ballpark of $10 - 20$ m/s (Chakrabarti et al. 2008; Nandi et al. 2012; Debnath et al. 2013). This suggests the possibility of the local modulation of accretion rate due to feedback from the outflow (Chakrabarti & Manickam, 2000; Chakrabarti & Nandi, 2000). All these results indicate that GRS 1915+105 went through repeated micro-flares when it is in a θ-class.

As the shock location moves closer and becomes weaker, the QPO frequency increases since the frequency is inversely proportional to the infall time scale from the shock front. This behavior is common in the rising phase of transient BHCs (see, Debnath et al. 2013 and references therein). Therefore, as the source transits from SIMS to SS, the QPO frequency should increase. This has been corroborated by our timing analysis. As shown in Fig. 4.2(a,b), the QPO frequency shifts towards the higher frequency domain with the evolution of time. Within the first 225 seconds of observation where QPO is relatively prominent, the QPO frequency moves from 4.22 Hz to 4.51 Hz in the first orbit. In the second orbit, the QPO frequency monotonically increases from 2.90 Hz to 4.33 Hz within a span of 400 seconds (Table 1). During this period, shock location also decreases from 65.8 r_s to 55.7 r_s (Table 2). These findings further suggest that an interplay of two accretion rates is at the root of the manifestation of the spectral and the timing behaviors and their coupling. We have further observed the lower frequency QPO at $\sim$ 2 Hz in the first orbit. The integrated fractional RMS turned out to be $\sim 6\%$.

GRS 1915+105 and IGR 17091-3624 exhibit several classes that can be well differentiated by the Comptonizing efficiency (Pal & Chakrabarti 2015). As the variability class moves from the harder states (HS, HIMS) to the softer (SIMS, SS) states, the cooling time-scale is reduced with the increase of soft photon influx. This shrinks the CENBOL, resulting inward movement of the shock to raise the frequency of the low-frequency QPOs. In the previous chapter, it has been discussed that in the case of χ class of GRS 1915+105 where X-ray flux is steady, accretion flow could be explained in the light of TCAF paradigm (Banerjee et al., 2020). Presently, it has been demonstrated that even inside a single variable class, there are considerable

changes in the shock properties and accretion rates. Inferences regarding the flow from our analysis agree with the TCAF paradigm which explains the spectral and timing properties of GRS 1915+105 to be due to the interplay between the Keplerian and sub-Keplerian flows, the launching of outflows from the CENBOL region, and the effects of radiative transfer within the sonic sphere of the outflow (Nandi, Manickam and Chakrabarti 2000b). The outflow rate depends upon the spectral state (Chakrabarti 1999) as the outflow is cooled via inverse Comptonization of the intercepted soft seed photons from the disk. This makes part of the outflow from the sonic sphere to fall back upon the accreting flow and modulate the accretion rate locally. The effects of Compton cooling on the outflow formation have been thoroughly investigated by Garain et al. (2012) using time-dependent Monte Carlo simulation and the reduction of outflow rate with the increased thermal flux has been established. This accretion flow feedback could explain the rapid variation in accretion rates and consequent shock location in a few tens to a few hundreds of seconds, with a shock velocity ($\sim$ few hundred m/s) significantly higher as compared to usual transient sources during their outbursts ($\sim$ few tens m/s). Gradual increase of mainly the Keplerian disk accretion rate with the gradual rise in spectral softness in the U-shaped domain is suggested by Fig. 4.5(a,b). With the increase of the disk rate, the shock location moves inwards, causing the QPO frequency to go upwards. However, as the spectral states grow softer with increasing disk rate, the strength of QPOs gradually diminishes. The upward trend of the dominant power with the photon intensity in Fig. 4.2(a,b) and an explicit downward trend in Fig. 4.3(a,b) are in agreement with the aforementioned QPO behavior. This interconnected nature of spectral and timing properties manifested in Fig. 4.2, 4.3, and 4.5 are indicative of both effects being of the same origin as suggested in TCAF paradigm. For the first time, we are able to see how the TCAF fitted parameters such as the accretion rates and the shock location change during rapid intensity variations in the count rate of the θ class of GRS 1915+105.

Theoretical investigation on the behavior of magnetic flux tubes under the influence of various competing forces in TCAF configuration had been carried out by Nandi et al. (2001b). It was observed that the collapse of the flux tubes under magnetic tension would be the dominant phenomena in hot plasma (temperature $\geq 10^{10}$K), which would expel the matter in the transverse direction. This evacuation of disk matter explains the origin of 'baby jets'. However, the estimation of the mass contained in the baby jets was found to be one order of magnitude smaller than the earlier

estimation (Mirabel et al 1998), which implies that the sub-Keplerian flow can contribute to such evacuations as well. This picture is aligned with the qualitative scenario of the ejection of the Comptonizing region presented by Vadawale et al. (2001, 2003) to explain the association of large radio flares and soft dips. The importance of disk-jet interaction and the nature of ejecta in determining the X-ray variability patterns was highlighted by Klein-Wolt et al. (2002) as well. In the present paper, we focus our attention on the U-shaped variability of longer duration ($\sim$ few hundred seconds). We find QPOs during the hard intermediate state (bottom part of the U-shaped light curve) and their gradual disappearance in the regions of softer states. This implies that the CENBOL is present in the hard intermediate state, though it may gradually form and weaken inside one U-shaped part of the light curve. Our proposition of the collapse of the base of the outflow and the modulation of the accretion rate due to the return flow, which is a natural consequence of the TCAF paradigm, is one plausible way to explain this observation. More extensive spectro-temporal analysis to test this hypothesis for various other classes would be an interesting exercise.

Chapter 5

Is GRS 1915+105 Truly Unique?

5.1 Introduction

In Chapter 1, Section 1.6, it was mentioned that the identification of IGR J17091-3624 showing high amplitude and structured variability like GRS 1915+105 offers an unique opportunity to comprehend the underlying physical mechanism and its relationship with much faster (sub-second) variability. Right from the beginning of the outburst in 2011 February, IGR J17091–3624 has been monitored with the Proportional Counter Array (PCA; Jahoda et al. 2006) onboard RXTE almost on a daily basis. In order to perform our comparative study on the basis of detailed spectro-temporal analysis, we have select pointed RXTE observations of GRS 1915+105 and IGR J17091–3624 both, which show significant and rapid variability. The variability patterns corresponding to some of these observations of IGR J17091–3624 were pointed to be similar to those observed in the case of GRS 1915+105.

The IGR J17091–3624 observation 96420-01-05-00 (MJD 55648) and GRS 1915+105 observation 10408-01-40-00 (MJD 50369) pertain to the ν class, as identified by Altamirano et al. (2011d). This class is characterized by the slow variability over a span of few tens of seconds, followed by short duration flares and subsequent sharp dips. In the case of IGR J17091-3624, the dip-to-dip duration is $\sim$ 50 seconds and the photon intensity recovers gradually from dip to flare. In the case of GRS 1915+105, on the other hand, the flares are sharper, single-peaked and the dip-to-dip duration is

$\sim$100 seconds. From dip to flare, the photon count remains nearly constant for a few tens of seconds, and then during the immediate prior to the flare the intensity sharply increases.

On the other hand, IGR J17091-3624 observation 96420-01-31-05 (MJD 55832) is marked by the recurrent appearance of nearly non-variable followed by highly variable sub-states and such variability is hitherto undetected in the case of GRS 1915+105 (Pahari et al. 2012). This variability class is known to be the C2 class. Following the persistence of the variable sub-state for a few hundred seconds, the source makes a transition into the non-variable sub-state in a few tens of seconds. The mean intensities of the two sub-states are observed to be similar.

5.2 Class Variable Source IGR J17091-3624: Observation and Data Reduction

We have selected these publicly available RXTE pointed observations for the purpose of the spectral and temporal analysis. In order to undertake the spectral analysis, standard-2 mode data from the PCA had been considered. The 2.5-25.0 keV background-subtracted spectra from all layers of individual Proportional Counter Units (PCUs) corresponding to all the available PCUs are co-added to enhance the photon intensity within an observation span. The 1% systematic error has been employed to achieve the best-fit parameters. Photoelectric absorption model PHABS has been employed to account for the interstellar absorption and the hydrogen column density pertaining to GRS 1915+105 and IGR J17091-3624 are kept fixed at 6.0×10^{22} cm^{-2} (Muno et al. 1999) and 1.1×10^{22} cm^{-2} (Krimm & Kennea 2011) respectively. Mass of GRS 1915+105 is pegged at 14 $M_{\odot}$, and mass of IGR J17091-3624 is kept frozen at 10 $M_{\odot}$.

For the performance of timing analysis, RXTE/PCA Good Xenon mode data with $\sim$ 0.953-microsecond time resolution has been employed. If the Good Xenon file containing the data from all the channels is unavailable, the time series obtained from event mode and binned mode data are combined. The binned mode data corresponding to 0-35 channels are extracted using FTOOLS task SAEXTRCT. These are combined with the event mode data for the rest of the channels after extraction using SEEXTRCT task. The addition of the lightcurves is carried out using 'lcmath' task. The Power

Density Spectra (PDS) are generated using FTOOLS task POWSPEC. The normalization parameter has been chosen to be -2 to subtract the expected white noise background to provide the squared *rms* variability per unit frequency interval. The lightcurves are re-binned to 0.01 second in order to obtain the Nyquist frequency of 50 Hz. FTOOLS task TIMETRANS is employed to select a time segment of interest to produce the lightcurves and corresponding PDS over that specific time interval. The PDSs are rebinned by a geometric rebinning factor of 1.03 in the frequency space in order to improve the signal-to-noise ratio.

In the case of the rapidly varying classes of our interest, sometimes it becomes difficult to perform the spectral fit or obtain statistically significant PDS during the individual dip and flaring events. In such cases, we follow the intensity ratio method used in Vadawale et al. (2001, 2003). The full intensity of the source is obtained from a 2.0-60.0 keV background-subtracted lightcurve produced from raw science files. In order to investigate the presence/absence of the soft/hard components during individual dip/flare events, the lightcurve has been further sub-divided into the soft, intermediate and hard energy intervals defined as 2.0-6.0 keV (band A, 0-14 channels), 6.0-15.0 keV (band B, 15-35 channels) and 15.0-60.0 keV (band C, 36-100 channels). The source characteristics during the dips/flares are monitored in terms of the ratios of individual bands with broadband intensity (2.0-60.0 keV). In case the quasi-stable intensity variation over extended time intervals (few tens of seconds) is observed in either of the sources, the appearance/disappearance of QPOs in different energy bands are investigated and QPO properties are measured. The dynamic PDS are also produced to monitor the time evolution of peaked components in PDS with the intensity variations.

We have also used the methodology followed by (Ghosh, Banerjee & Chakrabarti 2018) employing dynamic photon index (Θ) to understand the source behavior during transition regions. If the photon counts in A, B & C energy bands are denoted as a, b and c respectively, then Θ is defined as

$$\Theta = \tan^{-1}[\frac{c-b}{E_C - E_B}], \tag{5.1}$$

where $E_A(= 4\text{keV}), E_B(= 10.5\text{keV})$ & $E_C(= 37.5\text{keV})$ are the mean energies corresponding to A, B and C blocks. Therefore, Θ effectively denotes the spectral slope of the hard energy domain drawn on a linear scale. The mathematical domain of excursion of Θ is $-1.57 < \Theta < +1.57$, even though $\tan\Theta$ would assume mostly the negative values since in most of the cases c is ex-

pected to be lesser compared to b. Therefore, in the softest states $\Theta \to -1.57$, while in harder states $\Theta \to 0$. Since the C block covers a wider energy interval compared to B, it is also possible to obtain positive $\tan\Theta$ values in harder states. Therefore, the temporal evolution of Θ becomes instrumental in inferring the spectral state evolution with the intensity variation of the source Ghosh, Banerjee & Chakrabarti 2018, Ghosh & Chakrabarti 2019).

5.3 Results

We describe below the results obtained from the spectral and temporal analysis on all the different variability classes. Since all the classes differ in their morphologies and intensity patterns, the strategy of the analysis differ from one class to another as well.

5.3.1 The ν Class

Figure 5.1(a,b) features the ν class lightcurves corresponding to GRS 1915+105 and IGR J17091-3624 respectively. In the case of GRS 1915+105, the photon count remains almost steady for $\sim$ 70-80 second, and then short duration ($\sim$ 10 second) flare is observed where the photon count increases by a factor $\sim$ 2 (Fig. 5.1a). Subsequently, a sharp dip is followed where the intensity decreases by a factor $\sim$ 3. Subsequent to the dip, the photon count recovers within a few tens of seconds when the second flare of magnitude comparable to the previous one is detected, after which the steady intensity phase is followed. In the case of IGR J17091-3624, however, the flaring events are much more repetitive ($\sim$ 40-50 second) and in between the flares, the intensity steadily increases. The post-flare intensity dip is also observed in the case of IGR J17091-3624, although the post-dip recovery of photon intensity is quicker in this case. The steady photon intensity phase is almost unobserved in IGR J17091-3624.

In order to investigate the energy dependence of the source evolution, we plot the photon counts of the two sources in 2.0-60.0 keV as well as A, B and C bands in Fig. 5.2(a,b). In the case of GRS 1915+105, the intensity in A and B bands evolve almost in the same way as the total intensity in 2.0-60.0 keV evolves (Fig. 5.2a, panel a, b and c). However, in the C band, the sharp spikes during flaring events are absent and sharp reductions of photon intensity are observed during the overall intensity dips. This confirms the

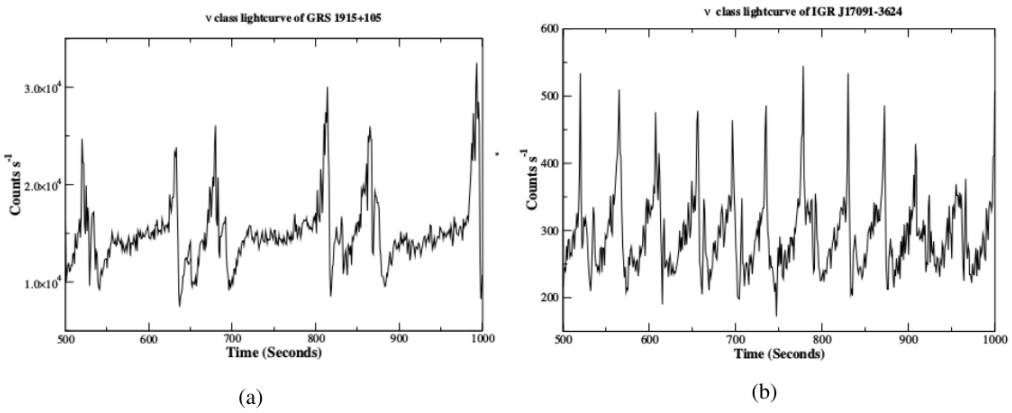

Figure 5.1: Comparison of lightcurves of (a) GRS 1915+105 and (b) IGR J17091-3624 in their ν class. The recurrence time of micro flares is shorter in the case of IGR J17091-3624. In case of GRS 1915+105 the photon count remains steady for $\sim$ 50 sec. in between the flares, but in IGR J17091-3624 such steady phase is not detected.

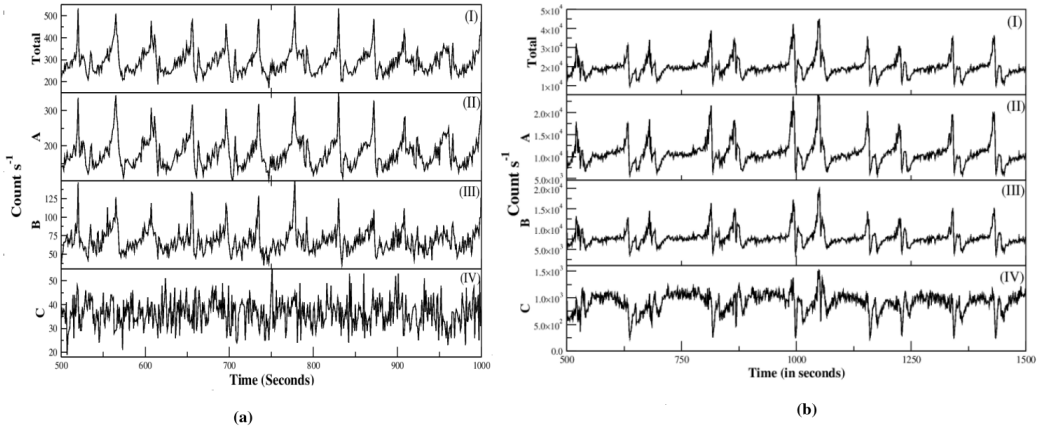

Figure 5.2: (a) Panel (I) contains broadband (2.0 -60.0 keV) lightcurve of IGR J17091-3624 in its ν class. In panels (II-IV), the lightcurves pertaining to A (2.0 -6.0 keV), B (6.0 - 15.0 keV) and C (15.0 - 60.0 keV) are provided. (b) Same sequence of lightcurves corresponding to GRS 1915+105.

evolution of the intensity across all three energy bands. However, in the case of IGR J17091-3624, the intensity in the C band does not show any rising or

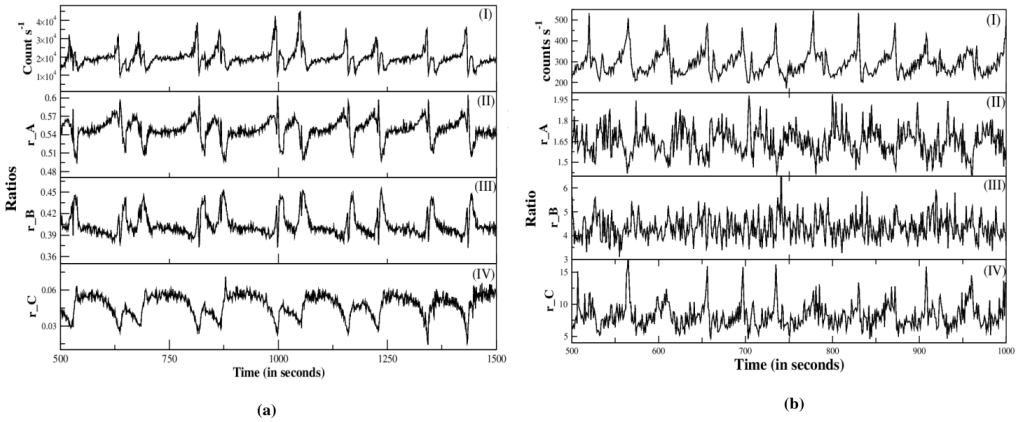

Figure 5.3: (a) The panel (I) contains the broadband lightcurve (2.0 -60.0 keV) of GRS 1915+105. In panels (II-IV), the ratios of A (2.0 - 6.0 keV), B (6.0 - 15.0 keV) and C (15.0 - 60.0 keV) band intensities with the broadband intensity (i.e. r_A, r_B and r_C respectively) are plotted. (b) Same sequence of broadband lightcurves and intensity ratios are plotted corresponding to IGR J17091-3624.

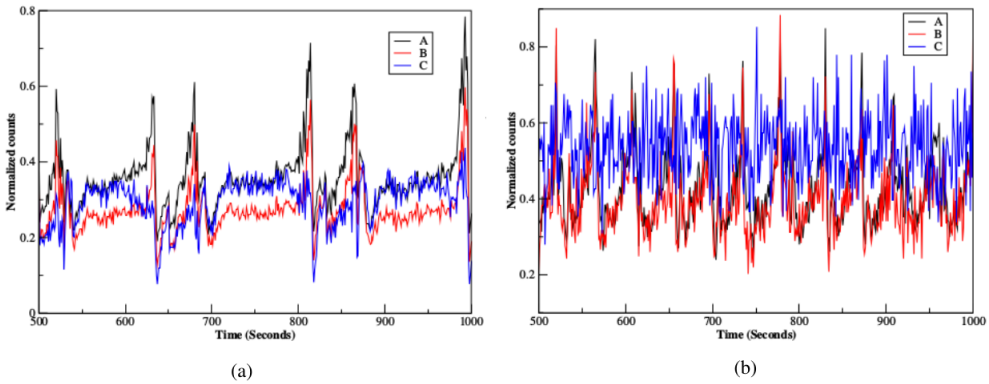

Figure 5.4: (a) The normalized counts of GRS 1915+105 in A (2.0 - 6.0 keV), B (6.0 - 15.0 keV) and C (15.0 - 60.0 keV) band are plotted together. We observe the preferential decrease in C-band count during the sharp intensity dips. During the flares, C band intensity does not increase at all. (b) Same normalized counts for IGR J17091-3624. We observe quasi variable C band intensity across the dips and flares.

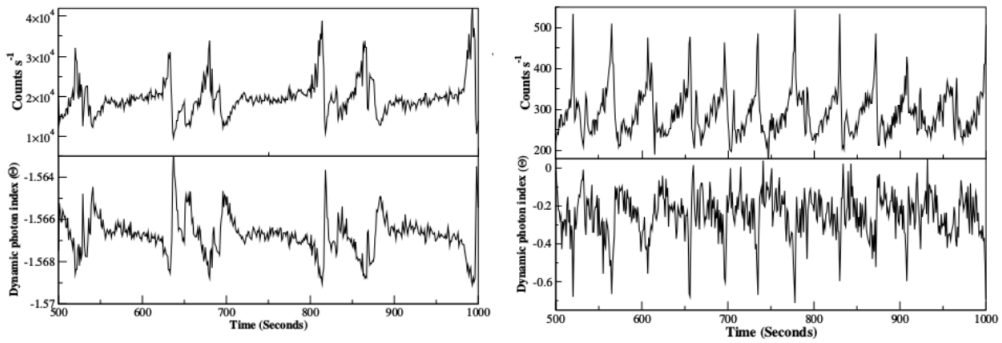

Figure 5.5: (a) The top and the bottom panels contain the variation of broadband intensity (2.0 - 60.0 keV) and the variation of dynamic photon index (Θ) respectively for GRS 1915+105 in its ν class. (b) Same sequence of plots for IGR J17091-3624. In this case, $\Theta \sim 0$ during the dips.

declining pattern, although distinguishable intensity variation is detected in the other two bands (Fig. 5.2b).

In order to obtain the relative changes of photons in different energy bands, we plot the ratio of photon counts A, B and C bands with the total number of photons (Cnt) in full 2.0-60.0 keV energy range (Fig. 5.3(a,b)). From Fig 5.3(a), it is observed that in the case of GRS 1915+105, the ratio of A band intensity and cnt ($r\_A = A/\text{cnt}$) gradually increases as the source evolves from dip to flare, but the ratio of B band intensity and cnt ($r\_B = B/\text{cnt}$) increases during the dips. The inverted shapes of r_B and r_C, on the other hand, imply that the intensity in C-band preferentially decreases during the dips and does not increase significantly during the flares as well. However, the absolute values of photon intensities in these three energy bands are significantly different. From Fig. 5.2(a), we observe the intensity in the C band is almost one order of magnitude smaller compared to the A or B band in the case of GRS 1915+105. Therefore, in order to further consolidate our observation, the normalized counts in all the energy bands are plotted and their evolution has been observed as a function of time (Fig. 5.4(a,b)). From Fig. 5.4(a), it is further observed that the C band intensity does not change during the flares, but gets preferentially decreased during the dip intervals. Although the intensity variation during the flares is the most prominent in the soft energy domain (A band), the B band intensity also changes by ~ 1.5 during these intervals. The preferential decrease of the C band during

intensity dips suggests the plausible disappearance of a hard tail during those dips.

In the case of IGR J17091-3624, on the other hand, both the A and B band intensities change significantly (by a factor $\sim 2-3$), but the C band intensity fluctuates around a mean value ~ 40 counts s^{-1} (Fig. 5.2(b)). In Fig 5.3(b), we observe the occurrence of peaks in r_A during the same instants at which broadband peaks are observed. This indicates the dominance of disk flux during the individual micro-flares. The r_B does not show sharp peaks, suggesting that the preferential increase of B-band intensity is potentially lesser compared to A-band. The dips in the C-band, on the other hand, are merely a consequence of nearly steady intensity across the temporal evolution of the source. Fig. 5.4(b) shows that the A and B band normalized counts evolve almost the same way from dip to flare, but the C band normalized counts do not show recurrent dips and flares.

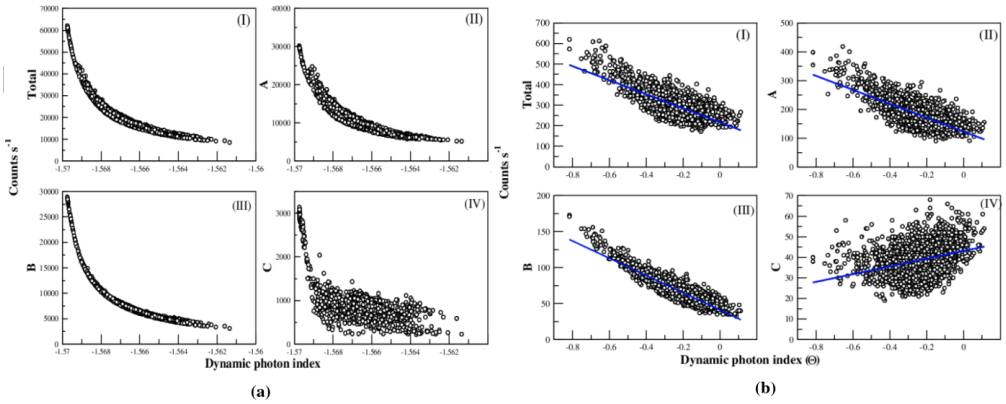

Figure 5.6: (a) Variation of Θ with broadband intensity (2.0 keV - 60.0 keV) as well as A (2.0 - 6.0 keV), B (6.0 - 15.0 keV) and C (15.0 - 60.0 keV) intensities are plotted in panels (I-IV) respectively. (b) Same sequence of plots for IGR J17091-3624. In this case weak positive correlation is observed for C-band intensity.

In order to further check the softness/hardness of the respective sources during their time evolution, the dynamic photon index (Θ) has been plotted along with the total intensity variation (2.0-60.0 keV) of the sources (Fig. 5.5(a,b)). In the case of GRS 1915+105, the photon count in the C-band is smaller than B-band by almost one order of magnitude (Fig. 5.4a), and this leads to $\Theta < -1.5$. In this case, Θ does not make large excursions, but the

relative hardness of the source during the intensity dips and gradual softness towards the flaring events is quite conspicuous (Fig. 5.5(a)). In the case of IGR J17091-3624, however, Θ makes sharp jumps from ~ 0 to ~ -0.5 during the flares. In this case, the proportion of the C-band count is substantially larger compared to GRS 1915+105. Therefore, while the variation of the hard component can play a crucial role in the ν class evolution of GRS 1915+105, in the case of IGR 17091-3624, this harder component is stable and dominant. This observation is further strengthened by the intensity vs. Θ plots (Fig. 5.6(a,b)). In Fig. 5.6(a), panels b and c, we observe that in the case of GRS 1915+105, the increase in photon intensity in A and B bands both lead to marginally lower Θ values, namely increase in 'softness'. In panel d, such a relationship is not so apparent, but we observe clustering of the majority of observations within a narrow range of Θ. However, in the case of IGR 17091-3624, the photon count in C-band and Θ values are positively correlated, as depicted in Fig. 5.6(b), panel (d). The best-fitted line in panels (b,c) suggests softening of the source with the intensity of counts in A and B bands both, but in panel (d), the best-fitted line suggests that the source 'hardens' as count increases in band C.

In order to investigate the presence of QPOs during the different phases of the source evolution, we have produced the dynamic PDS corresponding to the time series in the entire 2.0-60.0 keV domain, as well as the A, B and C bands. The dynamic PDS has been generated by producing individual PDS corresponding to the time series of 50-second intervals and making the origin of each successive interval advance by 1 second. Corresponding to a 150-second long segment containing flaring events and successive relaxation to steady intensity phase, we provide the dynamic PDS in Fig. 5.7(a-d). During the initial flaring phase, we observe no signature of the peaked component in the dynamic PDS, but during the steady phase, a prominent peaked component at around ~ 7 Hz is observed. This peaked component is present in all A, B and C energy bands around the same frequency, suggesting the oscillation of the Comptonizing component and additional power-law component simultaneously. We have examined the individual PDS corresponding to the time series in full 2.0-60.0 energy range as well as all the energy bands A, B and C. Sharp QPOs are observed in all the cases. In order to quantify the QPOs, the PDS are fitted using two Lorentzians and one power-law profile. Corresponding to the full 2.0-60.0 keV lightcurve, the centroid frequency of the fundamental QPO has been found to be 7.19 ± 0.03 Hz, with the fractional rms power to be $4.55 \pm 0.13\%$ (Fig. 5.8(a)). We observe that in the case of

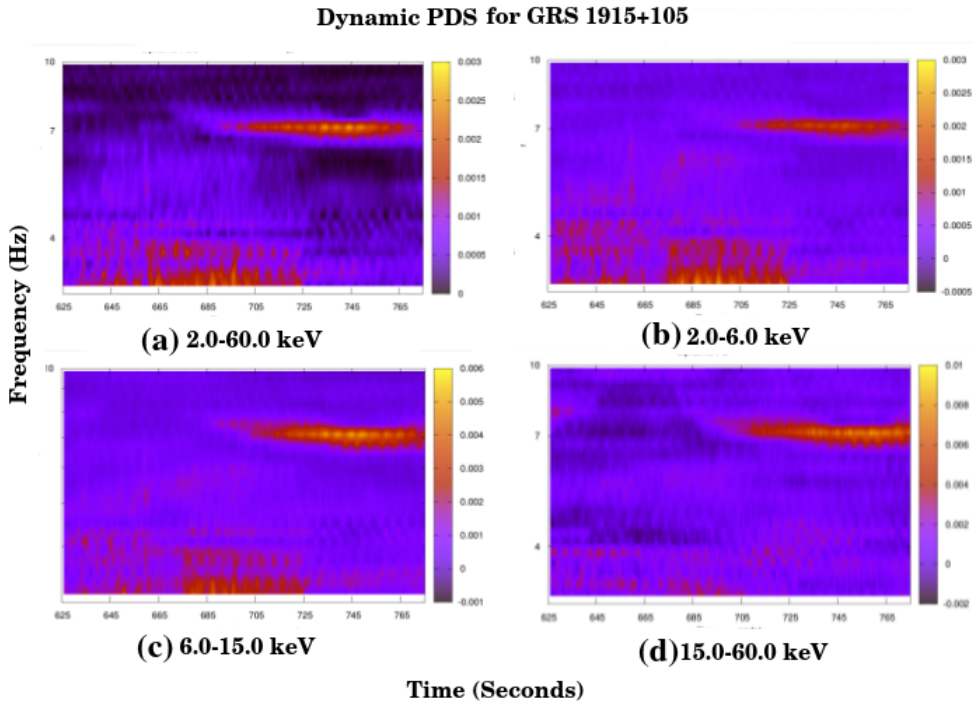

Figure 5.7: Dynamic power-density spectra for quasi-steady phase of GRS 1915+105 ν class data. Panel (a) contains dynamic PDS for broadband intensity (2.0 keV - 60.0 keV) and (b-d) contains dynamic PDS for A (2.0 - 6.0 keV), B (6.0 - 15.0 keV) and C (15.0 - 60.0 keV) band respectively.

band-A, the fractional rms power corresponding to the fundamental QPO is $\sim 3.2\%$, but in band B and C the rms amplitude increases to $\sim 5.2\%$ and $\sim 9.0\%$ respectively. Such energy dependence of rms power contained in QPO has been reported in the case of GRS 1915+105 earlier as well (Chakrabarti & Manickam 2000). The QPO normalization also increases from softer domain (A band) to harder domain (C band). Table 1 contains a full list of fitted parameters.

In the case of IGR J17091-3624, on the other hand, we observe a very sharp QPO in the PDS at around 23 mHz. We fit the fundamental QPO using the Lorentzian profile. The fundamental QPO frequency turns out to be 23.08$\pm$0.04 mHz, corresponding to which the fractional rms power was $\sim 14\%$ (Fig. 5.9(a)). Similar to GRS 1915+105, we attempt to observe the signature

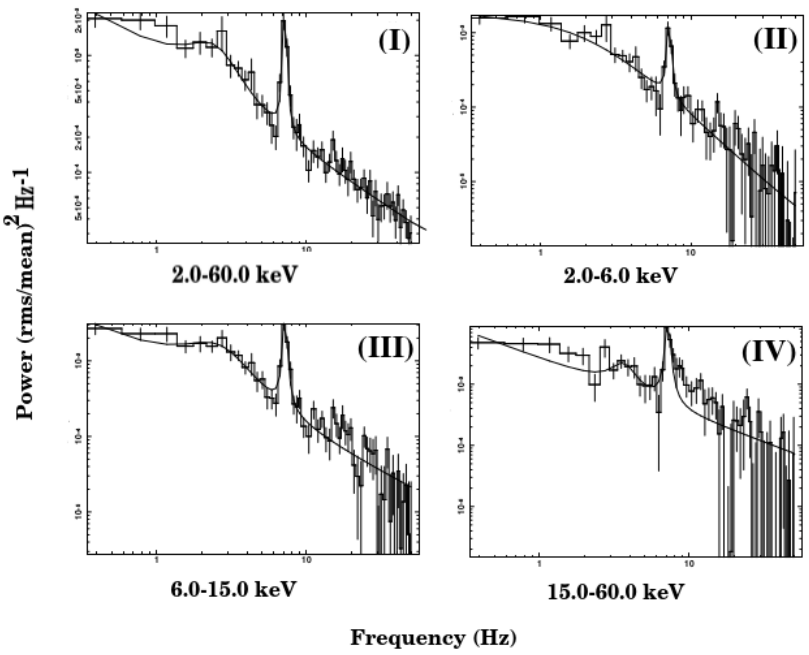

Figure 5.8: Power density spectra, fitted with two Lorentzians and one power-law profile. Panel (I) contains PDS fit corresponding to the full 2.0 - 60.0 keV energy range, and panels (II-IV) contain PDS fit for A, B and C band. In all cases, sharp QPOs $\sim$ 7.1 Hz are detected.

Table 1: QPO parameters of the fundamental QPO obtained from Lorentzian fitting.

Data Specification[a]	$v^b_{\rm QPO}$ (Hz)	FWHM[c]	RMS[d] (%)
full[e]	7.19 ± 0.04	0.42 ± 0.03	4.55 ± 0.13
A	7.19 ± 0.03	0.20 ± 0.03	3.27 ± 0.11
B	7.19 ± 0.05	0.25 ± 0.05	5.24 ± 0.16
C	7.20 ± 0.04	0.37 ± 0.07	9.01 ± 0.18

Note: [a] The QPO parameters in different energy bands. [b] The centroid frequency of QPO. [c] Full width at half maxima. [d] The fractional rms power corresponding to QPO. [e] corresponds to 2.0-60.0 keV.

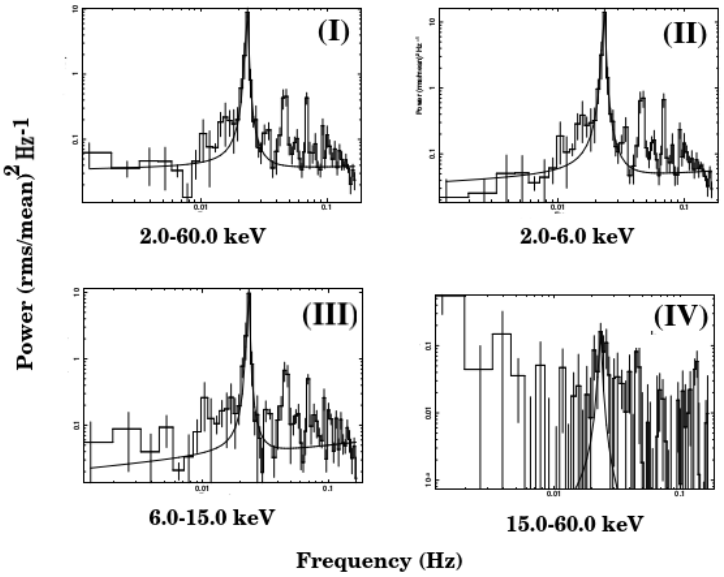

Figure 5.9: The centroid frequency fitted with Lorentzian profile. Panel (I) contains PDS fit corresponding to the full 2.0 - 60.0 keV energy range, and panels (II-IV) contain PDS fit for A, B and C band. In all cases, sharp QPOs $\sim$ 23 mHz are detected.

of this prominent mHz QPO in different energy segments. Prominent mHz QPO in the same frequency is observed in band A and B (Fig. 5.9(b,c)), but in band C the QPO appears to be less prominent and the broadband noise component becomes dominant (Fig. 5.9(d)). This energy dependence of QPO is different from the observed variation in GRS 1915+105, where sharp QPOs in all A, B and C bands are detected. Lower QPO frequency in IGR J17091-3624 suggests a higher length scale of oscillation, which in the context of accretion flow happens to be the inner edge of the disk and the boundary of the Comptonizing region.

In order to understand the similarities/differences of these two objects in terms of their spectral characteristics, we first attempted the fitting of the spectra using empirical models like multicolor disc blackbody component (MCD, model as DISKBB in XSPEC; Mitsuda et al. 1984) and POWER-LAW. In the case of GRS 1915+105, the DISKBB+POWER-LAW fitted does not yield acceptable spectral fit for $\sim$ 200 second long quasi-steady intensity intervals

Table 2: Best-fit parameters obtained from the spectral fits corresponding to the ν class of GRS 1915+105 and IGR J17091-3624.

Model parameters	GRS 1915+105		IGR J17091-3624	
	TCAF+CUTOFFPL +PEXRAV	DISKBB+NTHCOMP +GAUSSIAN	TCAF+PEXRAV	DISKBB+POWER-LAW +GAUSSIAN
$T_{\rm in}$	–	$1.20^{+0.03}_{-0.04}$	–	$1.11^{+0.04}_{-0.05}$
$\Gamma_{\rm po}$	–	–	–	$2.15^{+0.05}_{-0.04}$
$\Gamma_{\rm nth}$	–	$2.69^{+0.12}_{-0.10}$	–	–
kT_e	–	$24.33^{+1.10}_{-1.25}$	–	–
$\dot{m}_d$	$1.02^{+0.06}_{-0.07}$	–	$0.12^{+0.01}_{-0.01}$	–
$\dot{m}_h$	$0.30^{+0.03}_{-0.03}$	–	$0.25^{+0.01}_{-0.02}$	–
X_s	$19.68^{+1.20}_{-1.40}$	–	$35.41^{+1.64}_{-1.70}$	–
R	$1.09^{+0.02}_{-0.03}$	–	$2.21^{+0.04}_{-0.03}$	–
α	$0.66^{+0.03}_{-0.02}$	–	–	–
β	$2.28^{+0.12}_{-0.13}$	–	–	–
$\Gamma_{\rm refl}$	$1.09^{+0.04}_{-0.03}$	–	$1.10^{+0.03}_{-0.04}$	–
E_c	$8.31^{+0.09}_{-0.08}$	–	$1.79^{+0.04}_{-0.02}$	–
${\rm rel}_{\rm refl}$	$2.34^{+0.08}_{-0.07}$	–	$5.77^{+0.06}_{-0.08}$	–
$\chi^2_{\rm DOF}$	31.31/41	41.30/43	53.37/43	47.92/43

Note: $T_{\rm in}$: inner disk temperature in keV. $\Gamma_{\rm po}$: photon index from DISKBB model. $\Gamma_{\rm nth}$: photon index from NTHCOMP model. $kT_{\rm in}$: electron temperature from NTHCOMP model. $\dot{m}_d$: disk rate in Eddington unit. $\dot{m}_h$: halo rate in Eddington unit. X_s: Shock location in r_g. R: Shock strength. $\Gamma_{\rm refl}$: photon index from PEXRAV. E_c: cutoff energy from PEXRAV. ${\rm rel}_{\rm refl}$: reflection fraction. In NTHCOMP, the seed photon temperature has been tied to $T_{\rm in}$.

between dip and flare events. The χ^2/DOF turns out to be 156.70/49. The profile was unable to account for the higher energy tail of the spectra (> 20 keV) and excess emission is observed ~ 6.5 keV. The addition of a Gaussian line does not bring reduced χ^2 below 2.0. The replacement of the power-law model with the Comptonization model NTHCOMP leads to a significant improvement of the quality of the spectral fit (χ^2/DOF = 48.35/45). During this spectral fitting, we tie the disk blackbody temperature ($T_{\rm in} = 1.20 \pm 0.03$ keV) of DISKBB model with the input soft seed photon temperature of NTHCOMP. The electron temperature of NTHCOMP model turns out to be 24.3 ± 4.0 keV. We have calculated the energy flux contributed by the disk and the Comptonizing component separately using the XSPEC convolution model CFLUX. The DISKBB flux (4.89×10^{-8} ergs s^{-1}cm^{-2}) turns out to be greater compared to the Comptonized flux contributed by NTHCOMP (2.69×10^{-8} ergs s^{-1}cm^{-2}). However, the energy flux of IGR J17091-3624 is one order of magnitude smaller than that of GRS 1915+105.

In case of IGR 17091-3624 the spectra were well fitted with DISKBB+PO along with a gaussian at 6.5 keV (χ^2/DOF = 47.92/43) to account for the Iron line emission. The energy flux pertaining to DISKBB (2.43×10^{-9} ergs s^{-1}cm^{-2})

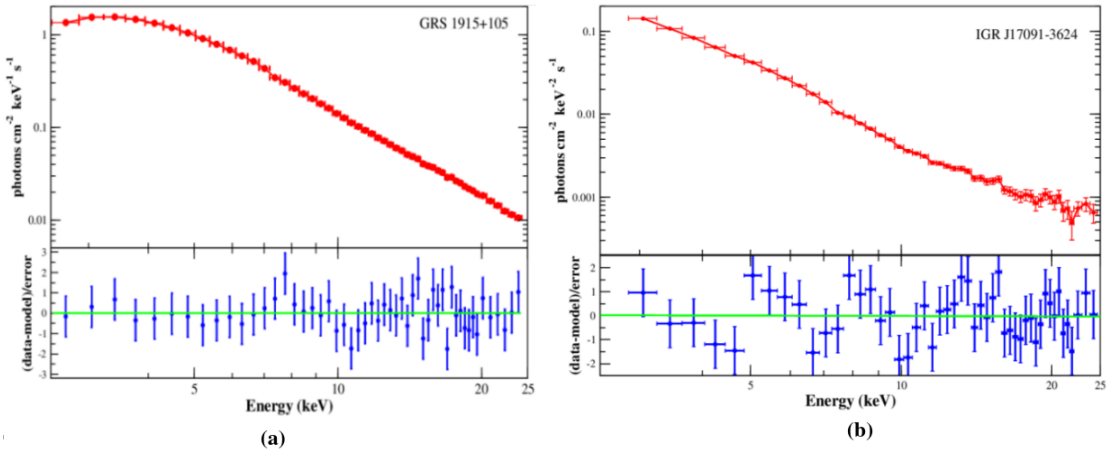

Figure 5.10: (a) The 2.5 - 25.0 keV energy spectra fitted with TCAF+CUTOFFPL+PEXRAV model in the case of the ν class data of GRS 1915+105. The residuals are shown in the bottom panel. (b) Energy spectra of the same energy range corresponding to the ν class data of IGR J17091-3624 fitted with TCAF+PEXRAV model. Bottom panel contains the residuals.

and POWER-LAW (2.48×10^{-9} ergs s^{-1}cm^{-2}) are separately calculated and are found to be almost equal. This implies that the proportion of high energy flux in case of IGR J17091-3624 is greater compared to GRS 1915+105 and this makes IGR J17091-3624 spectrally harder; a conclusion that is further supported from the ratio plots and Θ-intensity correlations.

In order to derive further insights regarding the accretion flow geometry and investigate the presence of different spectral components, we have attempted spectral fitting using TCAF and extract the underlying accretion flow parameters. The spectral fitting using TCAF as the only model provided unacceptable fits (χ^2/DOF = 419.36/45). Both in the low and high energy domain the spectra were not well fitted. The addition of a Gaussian at 6.5 keV did not provide statistically viable fits either. This leads us to investigate the presence of the Compton reflection component to account for the fluorescence line emission and its Comptonization. The spectral model employed for this purpose is the reflection of the exponentially cut-off power-law spectrum from neutral disk medium (PEXRAV model, Magdziarz & Zdziarski 1995). The Iron abundance had been taken to be that of solar value, considering the presence of the source in the Galactic bulge. The spectral fit was found to be statistically viable (χ^2/DOF = 45.13/41). Among the TCAF

fitted parameters, the sub-Keplerain halo rate (0.25 $\dot{M}_{Edd}$) was found to be more compared to the disk rate (0.12 $\dot{M}_{Edd}$), which is in agreement with the 'harder' nature of the source in this class. Table 2 features the full list of spectral fitted parameters.

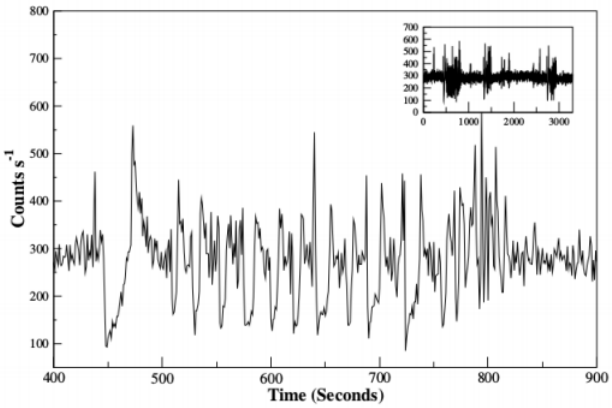

Figure 5.11: The C2 class lightcurve pertaining to IGR J17091-3624. The source transitions from highly variable phase spanning over a few hundred seconds to nearly non-variable phase. The inset contains the full extent of the time series which shows a few variable and non-variable intervals together.

In case of GRS 1915+105, however, TCAF+PEXRAV model was not sufficient to bring χ^2_{red} below 2. A few of the parameters could not be constrained and the fit was unacceptable (χ^2/DOF = 764.29/44). In order to obtain a reliable fit, we added an additional power-law component arising out of secondary Comptonization/synchrotron emission from micro ejections. Since the standard power-law component does not reproduce the high energy tail of the spectra reliably, we added the CUTOFFPL component which contains the power-law photon index (α) and an exponential roll-over factor (β). Low α and high β implies relative hardening of the spectra. With this additive CUTOFFPL model, very good reduced χ^2 value could be achieved (χ^2/DOF = 30.44/42). In order to make a comparison with the spectral parameters arising out of the spectral fitting of IGR J17091-3624, we froze the TCAF normalization value at the one obtained from IGR J17091-3624 fitting. The disk accretion rate 1.02 $\dot{M}_{Edd}$ and sub-Keplerian halo rate 0.30 $\dot{M}_{Edd}$ both turned out to be significantly greater compared to IGR J17091-3624. These relative changes are in tune with the observed luminosity differences between

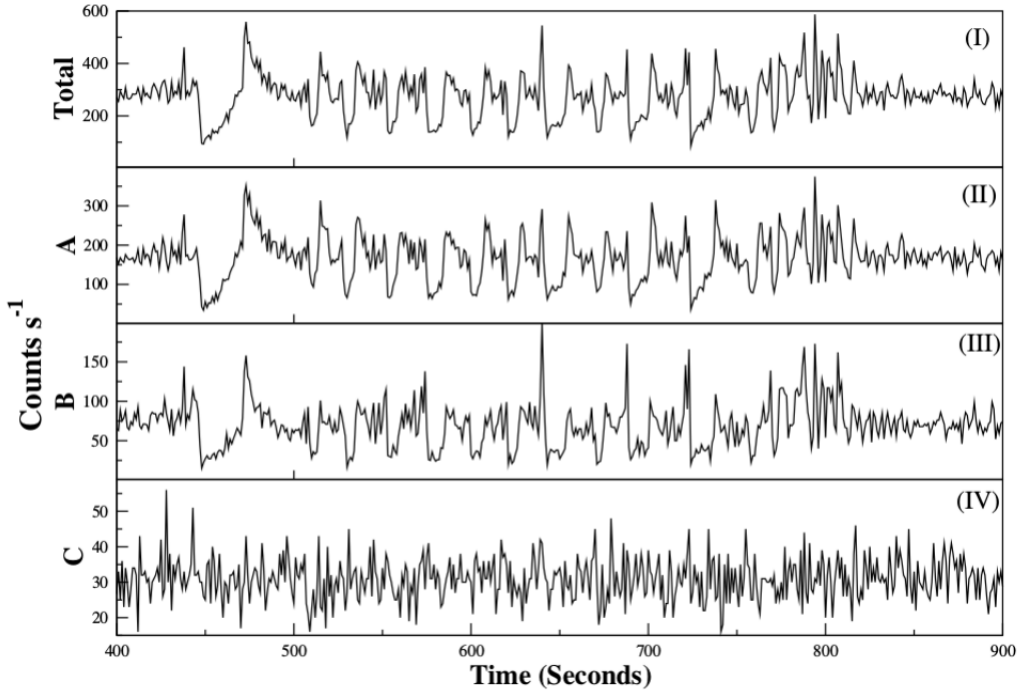

Figure 5.12: The 2.0-60.0 keV lightcurve of C2 class of IGR J17091-3624 (top panel) as well as the lightcurves corresponding to A (2.0-6.0 keV), B (6.0-15.0 keV) and C (15.0-60.0 keV) bands (panels b-d). The C-band lightcurve remains nearly steady across dip and flare events.

these two sources. In the case of GRS 1915+105, the relative accretion rates further confirm the softness of GRS 1915+105 during ν class, during which the shock location moves considerably inwards; a result that has earlier been observed for many black hole transients (see Bhattacharjee et al. 2017 for an example) as well as for χ and θ classes of GRS 1915+105 (Banerjee et al. 2020a,b). The reflection fraction is smaller in GRS 1915+105, as the spectral fits suggest. In Table 2, the spectral fitted parameters along with 90% confidence ranges corresponding to each parameter have been provided. Fig. 5.10(a,b) features the 2.5-25.0 keV RXTE PCA unfolded spectra of GRS 1915+105 and IGR J17091-3624 respectively as well as the residuals after spectral fitting.

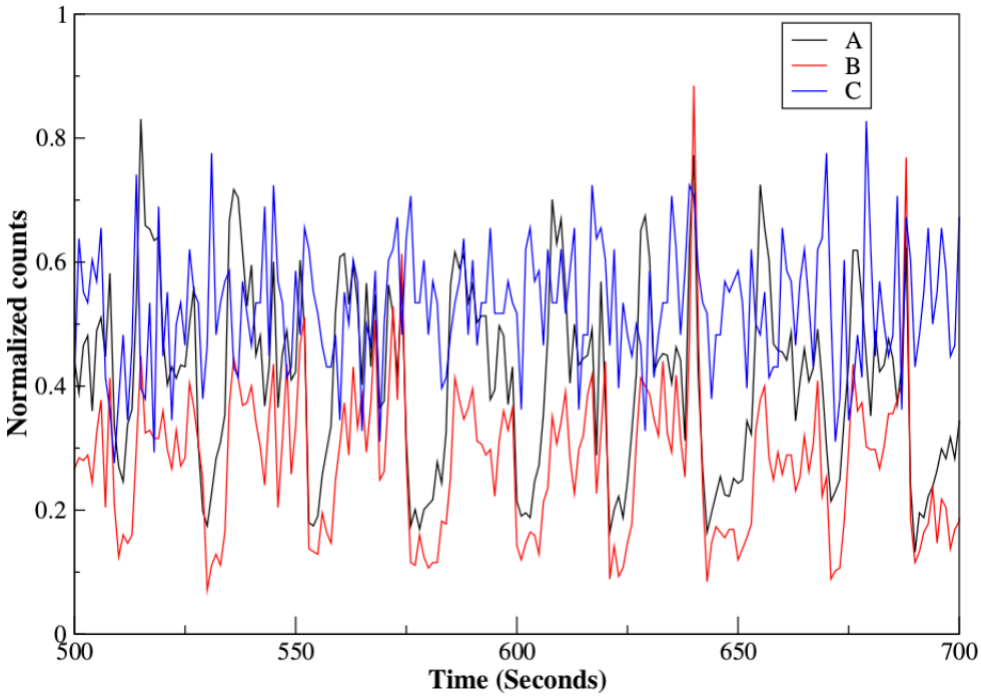

Figure 5.13: The time variation of the normalized photon count for C2 class of IGR J17091-3624 in A, B and C bands. The B band intensity preferentially decreases during the dips, while the C band intensity remains nearly constant throughout the time interval.

5.3.2 The C2 class

Having examined the spectro-temporal characteristics in ν variability class of these two sources, we attempted to explore the plausible signatures of these findings in the C2 class of IGR J17091-3624, which has no morphological counterpart corresponding to GRS 1915+105 (Pahari et al. 2012). This was performed to identify the extent to which the subtle features of GRS 1915+105 is detected in similar sources as well. The C2 class is distinguished by the repeated appearance of quasi-variable and rapidly variable sub-state, each of which is of $\sim$ a few hundred seconds duration (Fig. 5.11). The transition from the highly variable sub-state to the quasi variable sub-state happens within $\sim$ few tens of seconds. Even though within one variable sub-state the intensity excursions can be within a factor $\sim$ 4-5, the average intensities of these two sub-states remain almost the same, such that they

have similar mean Hard color (Pahari et al. 2012). In order to explore the contribution of the photons from different energy bands during the small dips and flares during the variable sub-state as well as the dominance of different energy bands during the sub-state transition, we produced the energy-resolved lightcurves as done previously for ν variability class (Fig 5.12). The lightcurves pertaining to A and B bands show correlated behavior in terms of the appearance of dip and flare events observed in the lightcurve over the full PCA energy range (2.0-60.0 keV). However, the C-band lightcurve does not show any prominent variability and the count remains quasi-steady during the entire passage of the highly variable sub-state. The relative dominance of these three bands is further clarified in Fig. 5.13, where the temporal variation of the normalized counts in all three bands A, B and C are plotted. The preferential decrease in B-band count during the dip events as observed (Fig. 5.13) implies the plausible evacuation of the Comptonizing region during these events. However, the C-band count remains almost non-variable and the mean normalized intensity of C-band appears to be more as compared to the mean normalized intensity of A and B. This observation is indicative of the fact that there is almost no sign of the preferential changes of C-band intensity during this class.

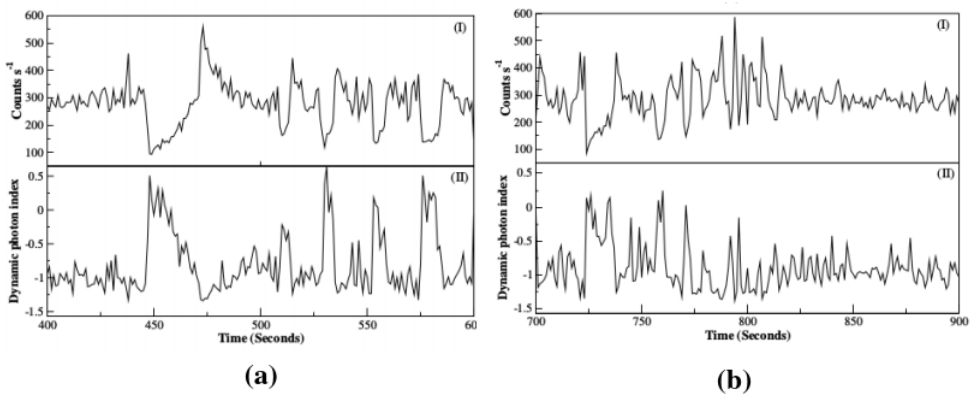

Figure 5.14: (a) Time variation of photon intensity (panel I) and dynamic photon index (panel II) in C2 class as the source transits from non-variable phase to highly variable phase. (b) Same variation as the source leaves the variable phase and moves again into non-variable phase.

In order to further test the changes in Hardness of the source during the variable to non-variable transition, we plot the dynamic photon index

as a function of time (Fig 5.14(a,b)). During the dips, the Θ value becomes > 0, which was not observed in the case of ν class (Fig. 5.14(a)). This is in alignment with the finding that the C band intensity remains almost unaltered during the dips while B-band experiences a preferential intensity decline. However, we observe that as the source makes a transition from variable to non-variable sub-state, there is no sharp change in Θ value (Fig. 5.14(b), panel (b)). This observation is in consonance with the conclusion by Pahari et al. (2012) that the sharp Hard color change is unobserved during the sub-state transition. The energy-resolved intensity dependence with Θ is shown in Fig. 5.15, where the variation of Θ with the full broadband intensity (2.0-60.0 keV) with the A, B and C band intensities are plotted. We observe negative correlations of Θ with photon intensity in A and B bands, but a weakly positive correlation in the C band. This further reinforces the previous observation of the dominant normalized count in C bands across dips and flares.

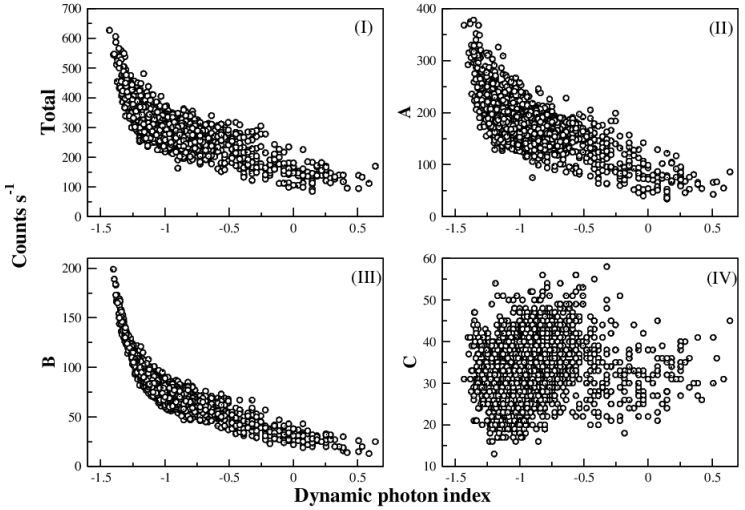

Figure 5.15: (a) Photon intensity vs. dynamic photon index (Θ) plot in broadband energy (2.0-60.0 keV, panel I) as well as the sub-bands (2.0-6.0 keV, panel II; 6.0-15.0 keV, panel III and 15.0-60.0 keV, panel IV).

Like in the case of ν class of GRS 1915+105, we have investigated the presence of low-frequency QPOs in PDS as well. The QPO observed, in this case, does not appear to be as sharp as observed there. The Lorentzian fit of the peaked component yields the frequency of the fundamental QPO to be

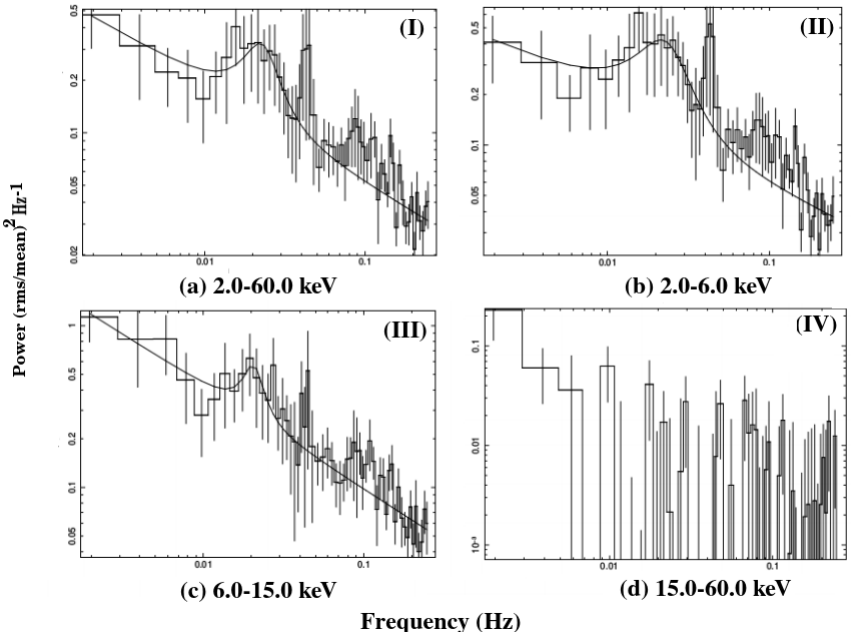

Figure 5.16: Power density spectra in broadband energy (2.0-60.0 keV, panel I) as well as in the sub-bands (2.0-6.0 keV, panel II; 6.0-15.0 keV, panel III and 15.0-60.0 keV, panel IV). The distinct peak is fitted with the Lorentzian profile. The rms amplitude corresponding to $\sim$ 22 mHz QPO is $\sim$ 6.5%. In C-band, any signature of QPO is not detected.

22.34 mHz, and the fractional rms power corresponding to the QPO happens to be $\sim$ 6.5% (Fig. 5.16(a)). Prominent QPOs are observed in A and B bands (2.0-6.0 keV and 6.0-15.0 keV respectively) as well (Fig. 5.16(b,c)), but in the C band we do not observe QPOs (Fig. 5.16(d)). This low-frequency QPO again suggests the larger length scale of oscillation.

In order to connect these temporal features with spectral characteristics and compare them with the spectral results from ν class analysis, we have undertaken the spectral analysis of steady and variable sub-states separately. In both of the cases, the combination of DISKBB and POWER-LAW models along with the Gaussian emission line at 6.5 keV produced acceptable spectral fits ($\chi^2_{\rm red} \sim 1$). The blackbody and power-law fluxes are found to be comparable ($\sim 1.4 \times 10^{-9}$ erg cm^{-2}s^{-1}) in both of the sub-states. In order to derive further insights regarding the accretion flow configuration, we attempted to fit the spectra using TCAF as well, with additional models to achieve the

Table 3: Best-fit parameters obtained from the spectral fits corresponding to the steady and variable phase in the C2 class of IGR J17091-3624.

Model parameters	steady phase		variable phase	
	TCAF+PEXRAV	DISKBB+PO +GAUSSIAN	TCAF+PEXRAV	DISKBB+PO +GAUSSIAN
$T_{\rm in}$	–	$1.65^{+0.07}_{-0.07}$	–	$1.51^{+0.05}_{-0.06}$
$\Gamma_{\rm po}$	–	$2.86^{+0.07}_{-0.06}$	–	$2.73^{+0.05}_{-0.06}$
$\dot{m}_d$	$0.57^{+0.05}_{-0.06}$	–	$0.54^{+0.02}_{-0.01}$	–
$\dot{m}_h$	$0.25^{+0.04}_{-0.05}$	–	$0.23^{+0.01}_{-0.02}$	–
X_s	$15.37^{+1.10}_{-1.15}$	–	$27.15^{+1.55}_{-1.60}$	–
R	$1.39^{+0.02}_{-0.01}$	–	$2.87^{+0.05}_{-0.04}$	–
$\Gamma_{\rm refl}$	$1.23^{+0.02}_{-0.02}$	–	$1.01^{+0.04}_{-0.05}$	–
E_c	$2.64^{+0.07}_{-0.06}$	–	$2.28^{+0.03}_{-0.03}$	–
$\rm rel_{refl}$	$6.36^{+0.08}_{-0.07}$	–	$5.08^{+0.06}_{-0.08}$	–
$\chi^2_{\rm DOF}$	40.99/41	41.30/43	58.91/41	53.37/43

Note: $T_{\rm in}$: inner disk temperature in keV. $\Gamma_{\rm po}$: photon index from DISKBB model. $\dot{m}_d$: disk rate in Eddington unit. $\dot{m}_h$: halo rate in Eddington unit. X_s: Shock location in r_g. R: Shock strength. $\Gamma_{\rm refl}$: photon index from PEXRAV. E_c: cutoff energy from PEXRAV. $\rm rel_{refl}$: reflection fraction.

statistically significant spectral fits. In the non-variable state the spectral fit solely using TCAF rendered unacceptable results (χ^2/DOF = 535.20/45). However, with the addition of the reflection model PEXRAV as before, viable spectral fit could be achieved (χ^2/DOF = 40.99/41). The disk accretion rate (0.57 $\dot{M}_{\rm Edd}$) was found to be considerably greater compared to the halo rate (0.25 $\dot{M}_{\rm Edd}$), which makes the shock location move close to the black hole ($15r_S$). In the case of variable phase, the spectral fit could again be achieved using TCAF+PEXRAV combination (χ^2/DOF = 58.91/41). The disk rate again dominates over the halo rate ($0.54\dot{M}_{\rm Edd}$ and $0.23\dot{M}_{\rm Edd}$ respectively) and the shock location moves slightly outwards (27.15 r_S) as compared to the steady case. Table 3 contains a full list of spectral fitted parameters.

5.4 Summary and Discussions

In this analysis, we have attempted to undertake a case study to compare the variability properties of GRS 1915+105 and IGR J17091-3624. For this purpose, spectro-temporal analysis has been performed on ν class data of

these two sources, as well as the C2 class of IGR J17091-3624 which contains both variable and non-variable phases and which has no counterpart in GRS 1915+105 morphology. From the analysis, we can draw the following conjectures regarding the underlying accretion flow scenario corresponding to these two classes.

1. The ν class data of IGR J17091-3624 show quasi-periodic occurrences of intensity dips and flares. The rising profile shows an exponential rise and is followed by a fast decay. However, a closer examination of the time evolution of ν variability class across different energy bands (A, B and C) shows that the C-band intensity remains nearly unchanged, while the A and B bands show dips and flares in tune with the broadband lightcurve (2.0-60.0 keV) of the source (Fig. 5.2(b)). Since the accretion flow components contributing to the A and B band photons are mostly variable, this could be attributed to the rapid evacuation and successive replenishment of the disk matter as well as a portion of the Comptonizing region. Such dynamic removal and refilling of the inner disk matter could be attributed to, as envisaged by Capitanio et al. (2012), the thermal-viscous instability driven by the radiation pressure in the hot inner disk region (Lightman & Eardley 1974; Nayakshin & Rappaport 2000). It could also be connected to the so-called 'magnetic rubber-band effect', where the blobby evacuations of the hot inner disk material are attributed to the catastrophic collapse of the stochastic magnetic flux tubes (Nandi et al. 2001a). This conjecture is further strengthened from the time variation of the dynamic photon index (Θ) (Fig. 5.5(b)) as well as the intensity vs. Θ plots (Fig. 5.6(b)), where the signature of 'hardening' is observed during the soft dips. The broadband intensity (2.0-60.0 keV) pattern is anti-correlated with Θ (Fig. 5.5(b)), and the C-band intensity shows weak positive correlation with Θ (Fig. 5.6(b)).

2. From the spectral analysis, we observe that the normalized fluxes of the empirical DISKBB and POWER-LAW models are comparable. The spectra can also be well fitted by invoking the reflection component coupled with the two-component model (TCAF). Therefore, the presence of two accretion flow components and the reflection of the Comptonized component from the disk seems to be well suited to explain the underlying flow properties.

3. In the case of ν class data of GRS 1915+105, the lightcurve is characterized by flaring activities, which is immediately followed by sharp dips and successive quasi-steady photon intensity over a few tens of seconds. The energy-resolved lightcurves in A, B and C bands show different patterns compared to IGR J17091-3624. While the C-band lightcurve of IGR J17091-3624 remained nearly non-variable, in the case of GRS 1915+105 the C-band intensity significantly diminishes during soft dips. It is also observed that the increase in intensity during flaring events is most prominent for the A band (soft energy domain), while in the C band, any signature of increase in photon count is undetected (Fig. 5.2(a)). The intensity ratio plot as well as the normalized count plot corresponding to A, B and C bands also depict preferential decrease of C-band intensity during soft dips for GRS 1915+105 (Fig. 5.3(a) and 5.4(a)). This is a crucial difference between the timing properties of these two sources in their ν class. This strongly suggests that the ν class morphology of GRS 1915+105 may not be just because of the inter-conversion of the existing flow components in their brief persistent phase, but the disappearance of a third component may be required to explain the spectro-temporal features.

4. Apart from the disk evacuation as a result of thermal-viscous instability or 'magnetic rubber band' effect as envisaged, we propose the presence of micro-flare events and the additional Compton emission from the flares to explain the observed energy-resolved temporal features of GRS 1915+105. If a fraction of the seed photons is intercepted by the micro-flares, that could cause the seed photons to up-scatter and an additional power-law component would be produced. This phenomenon would lead to the cooling of the flares and subsequent feedback on the accreting material. This rapid feedback loop can be one possible mechanism to explain the observed temporal characteristics. Short duration intensity variation during the flaring events is indicative of the local accretion flow modulation triggered by this feedback loop of accreting material. This mechanism has been previously suggested in the case of χ and θ class variability as well (Banerjee et al. 2020a,b). Additional power-law components could also be attributed to the high energy tail of the synchrotron emission from the micro-ejections (Vadawale et al. 2001).

5. In the case of GRS 1915+105, we also detect a sharp QPO at around 7 Hz during the nearly steady phase of its lightcurve in all A, B and C bands. The radial oscillation of the shock front causes the Comptonized component to oscillate, which is manifested as the sharp QPO corresponding to the PDS. The oscillation of the Comptonizing region causes the additional power-law component to oscillate as well. Since the movement of the inner edge of the disk is governed by the viscous time-scale, it can not oscillate in tune with the shock boundary. Therefore, the fraction of the Comptonized photons within 2.0-6.0 keV range contributes to the A-band QPO. However, once the accretion flow modulation because of the local feedback loop happens, the cooling becomes more efficient which makes the cooling time scale go down. This leads to the disappearance of QPOs, as observed during the transition of the source from the quasi-variable phase to the flaring phase.

   We report the presence of prominent QPO around 23 mHz in the case of IGR J17091-3624 in its ν class. We also examine the energy dependence of this QPO and observe that QPO is prominent in A and B bands, but any signs of QPO is not observed in C-band. This sharp QPO at a lower frequency in A and B bands is indicative of the larger length scale of oscillation of the source in that particular variability class. The oscillation of the inner edge of the disk, as well as the Compton cloud, is attributed to this oscillation as before; however, lower QPO frequency is suggestive of higher shock location. Such energy dependence of QPO is also observed in C2 class, but the QPO happens to be broader in C2 class.

6. The notion regarding the presence of a possible third component is further reinforced from the spectral fitting as well. In the case of ν class of GRS 1915+105, statistically acceptable spectral fits could not be achieved by adding the reflection component with TCAF only. We had to invoke an additional CUTOFF POWER-LAW model to incorporate the additional emission from the ejections as envisaged previously. However, during the spectral fitting of IGR J17091-3624, such an additional power-law was not necessary and the high energy Comptonized component remained persistent. This connection between the third additive component and the emission from the ejected material has earlier been drawn as well to explain the soft X-ray dips in GRS 1915+105 (Vadawale 2001a,b).

7. Finally, the nearly steady C-band intensity is detected in the case of C2 class observation as well. Like ν class data of IGR J17091-3624, the normalized count in C-band remains nearly non-variable across the sharp dips and flares (Fig. 5.12). However, $\Theta > 0$ values are obtained during soft dips, implying quick and brief hardening of the source during the dips (Fig. 5.13(a,b)). The transition from variable to non-variable phase is not marked by any abrupt changes in Θ, rather there is a gradual transition from rapidly fluctuating to quasi-variable Θ value. The weak positive correlation between the C-band intensity with Θ as well as the satisfactory spectral fits using TCAF+PEXRAV model are quite resembling with the ν class of IGR J17091-3624. Therefore, the existence of two components, the inner disk instability and the evacuation of the disk matter, like in the case of ν class, can be invoked in this case as well to explain the underlying accretion flow scenario.

Further long-term and continuous observation across other variability classes of these two sources and their comparative spectro-temporal studies are warranted to reveal further crucial information and to enable us to gain a holistic understanding regarding the underlying accretion flow properties triggering all these classes.

Chapter 6

Conclusions and Future Plans

In this Chapter, we will summarize the broad conclusions of the present thesis and also lay out some of the works that are ongoing / will be taken up in near future.

6.1 Conclusions

In Chapter 1, we have discussed at length the accretion mechanism around black holes and some of the radiative processes associated with the accretion which enable us to detect those black holes. We have also discussed some of the accretion flow models that have been proposed so far on the basis of the hydrodynamics and the radiative properties of the accreting matter, and the endeavors to connect the theoretical aspects with the observational findings. We have found several merits of the Two-Component Advective Flow (TCAF) paradigm which appears to play a crucial role in this context. It is found to be remarkably successful in self-consistently explaining the spectral and the timing features of the transient sources (including neutron stars). Subsequently, we have discussed in detail why GRS 1915+105 is such an important and intriguing source to study and why the proposition of two accretion flow components would be instrumental in explaining its spectacular timing and spectral features.

In Chapter 2, we have discussed the data acquisition procedure and analysis methodology that we have adopted in our analysis. The technical aspects of the X-ray satellites have been described in detail. The detector specifications, scopes and limitations have been discussed. We have broadly divided

our analysis into two sub-categories: timing and spectral analysis. We have described the analysis tools and specific requirements corresponding to the spectral and timing analysis both. In particular, a separate subsection has been dedicated to the discussion of the spectral analysis package that has been employed extensively in our analysis.

In Chapter 3, we have focused our discussion on the spectral features of the non-variable χ class data of GRS 1915+105 and its analysis under the TCAF paradigm. We have discussed the similarities and differences among different sub-classes under the umbrella of χ class, some of the observational findings regarding the presence of outflow in radio-plateau states as concluded in previous studies and previous attempts to understand the spectral features using phenomenological models. We have then described in detail the results obtained from spectral analysis using TCAF, and proposed a physical picture that can explain the accretion flow dynamics around GRS 1915+105 in χ class. We have also explained how this physical picture connects with other flow scenarios proposed earlier by several authors, and why the solution proposed by us fills a gap in the literature.

In Chapter 4, we extended our discussion to a highly variable θ class observation of this source. We described the characteristic features of this class, the time-scale of intensity variation in this class and how this is at variance with the time-scale involved in canonical transient sources. We discuss the variation of the Power Density Spectra with the evolution of the source and how it correlates with the spectral variations. We then conjecture the presence of a common underlying accretion flow mechanism that can explain both spectral and timing properties in θ class. We propose an underlying accretion flow mechanism that can explain the variabilities in θ class and can also be employed to explain the flow dynamics corresponding to other variable classes as well. This accretion flow mechanism proposed by us has been in alignment with earlier propositions made from spectro-temporal analysis previously.

In Chapter 5, we asked the pertinent and quite interesting question: why such large varieties of structured variabilities are observed in this source, which is absent in other normal X-ray binaries? One approach to address this question is to compare the spectro-temporal properties of GRS 1915+105 with another interesting source IGR J17091-3624, which has also shown some of the structured large-amplitude variabilities reported in GRS 1915+105, as well as some other variable classes which had not been previously reported in case of GRS 1915+105. This comparative study has been undertaken

in this Chapter. The ν variability class which shows the recurrent appearance of large-amplitude oscillation, together with C2 variability class in IGR J17091-3624 showing alternating non-variable and variable phases hitherto unobserved in GRS 1915+105 has been analyzed. Since photon intensity corresponding to IGR J17091-3624 is one order of magnitude lower compared to GRS 1915+105 and also the intensity variation happens at a shorter scale in the former case, there are inherent challenges in this exercise in terms of statistical limitations. However, some important clues regarding the accretion flow dynamics could be derived from the overall spectral fits using phenomenological models as well as TCAF (including refection models as well if necessary), the energy-resolved timing analysis to diagnose the dominance of different energy bands in different phases of variabilities and from the variation of dynamic photon index. The rapid variability and occasional non-variability could be associated with the interplay of the Keplerian and sub-Keplerian components. In the case of GRS 1915+105, it turns out that the accretion-ejection feedback mechanism needs to the incorporated as well to explain the observed spectro-temporal features.

6.2 Future Plans

The analysis of λ class data of GRS 1915+105, which encompasses the quasi-periodic occurrences of low-intensity plateau states and high-intensity bursts (burst-off and burst-on states respectively) is underway. Analysis of this class can provide important clues regarding the manifestation of large intensity variation in the very short time intervals in this class in the light of accretion-ejection coupling, accretion flow feedback and inner disk evaporation.

We are going to perform an analysis on two other important classes as well: class α and class β. They are distinguishable by their morphologies, X-ray color and time-scale of evolution. Both of them are associated with extended periods of spectrally hard dips but the duration of a hard dip in α class is nearly twice that of β class. The termination of the dip in α class is characterized by rapid X-ray oscillations. In the case of β class, the morphology is more complex. The hard dip extends for a few hundred seconds and is ended by a spectrally soft spike, followed by near monotonic increase in intensity. After attaining the peak flux, the X-ray begins rapid, large-amplitude oscillation. Contemporaneous infra-red (IR) ventures have demonstrated that as x-ray dip ends, the IR flare is triggered. In the case

of the β class, the IR flare is detected after the sharp X-ray spike, called the 'trigger spike'. Such features are interesting in their own right, because they mark the transition from quasi-stable phase to flaring phase, and potentially have a connection with the accretion-ejection interaction. The QPO evolution in different energy bands during the hard dip, the transition into flares, and subsequent rapid oscillation would be an interesting aspect to study. The evolution of the TCAF fitted parameters and the other additive or multiplicative components (if required) would be very important in obtaining an insight into the accretion flow evolution in this complex morphology.

In near future, we are also going to undertake the broadband study (including X-ray, radio and IR) of these two sources to derive a holistic picture of the accretion flows and the manifestation of the physical phenomena in different frequency intervals. A more thoroughgoing analysis would also be done to understand the possible similarities and differences regarding the launching mechanism of the powerful jets by GRS 1915+105 and AGNs.

Bibliography

Abramowicz, M., Jaroszynski, M., & Sikora, M., 1978, JAA, 63, 221

Abramowicz, M., & Zurek, W. H. 1981, ApJ 246, 314

Abramowicz, M. A. 1985, PASJ, 37, 727

Agarwal, P. C., Yadav, J. S., Antia, H. M., et al. 2017, JApA, 38, 30

Altamirano, D., Belloni, T., Krimm, H., et al. 2011a, ATel, 3230

Altamirano, D., Belloni, T., Krimm, H., et al. 2011b, ATel, 3299

Altamirano, D., Linares, M., van der Klis, M., et al. 2011c, ATel, 3225

Altamirano D. et al., 2011d, ApJ, 742, L17

Altamirano, D. & Belloni, T., 2012, APJ, 747, 4-9

Antia, H. M., Yadav, J. S., Agrawal, P. C., et al. 2017, ApJS, 231, 10

Arnaud, K. and Dorman, B. 2002, XSPEC (An X-ray Spectral Fitting Package), version 11.2x (NASA/GSFC/HEASARC, Greenbelt)

Banerjee, A., Bhattacharjee, A., Debnath, D. & Chakrabarti, S. K., 2020a, RAA, 20, 208

Banerjee, A., Bhattacharjee, A., Chatterjee, D. et al., 2020b, arXiv:2007.05273v1

Banerjee, A., Bhattacharjee, A., Debnath, D. & Chakrabarti, S. K., 2021, arXiv:2101.11854v1

Barr, P., White, N. E. & Page, C.G., 1985, MNRAS 216, 65

Belloni, T., Klein-Wolt, M., Mendez, M., et al., 2000, A&A 355, 271

Belloni T., Méndez M., King A.R. et al. 1997a, ApJ 479, L145

Belloni T., Méndez M., King A.R. et al. 1997b, ApJ 488, L109

Belloni, T., Psaltis, D., van der Klis, M., 2002, ApJ, 572, 392

Bhattacharjee, A., Banerjee, I., Banerjee, A., et al. 2017, MNRAS, 466, 1372

Bhattacharjee, A. & Chakrabarti, S. K., 2017, MNRAS, 472, 1361

Bhattacharjee, A. & Chakrabarti, S. K., 2019, ApJ, 873, 119

Bhattacharjee, A., 2018, in Exploring the Universe: From Near Space to Extra-galactic Mukhopadhyay, B & Sasmal, S. (Eds.), ASSP, 53, 93, Springer (Heidelberg)

Blum J. L., Miller J. M., Fabian A. C. et al. 2009, ApJ, 706, 60

Bondi, H., 1952, MNRAS, 112, 195

Brocksopp, C., Fender, R. P., Larionov, V., et al. 1999, MNRAS 309, 1063

Castro-Tirado A.J., Brandt S., Lund S., 1992, IAU Circ. 5590

Coe, M. J., Engel, A. R. and Quenby, J. J. 1976, Nature 259, 544

Chakrabarti, S. K., 1985, ApJ 294, 383

Chakrabarti, S. K. 1989, ApJ, 347, 365

Chakrabarti, S. K. 1990, ApJ, 362, 406

Chakrabarti S. K., 1995, in Bohringer H., Morfil G. E., Trumper J., eds, Seventeenth Texas Symposium on Relativistic Astro-physics and Cosmology, Vol. 759. New York Academy of Sciences, p. 546

Chakrabarti, S. K., 1995, Proc. of 17th Texas Symposium, 1994, (arXiv:9502040)

Chakrabarti, S. K. 1996a, ApJ, 464, 664

Chakrabarti, S. K. 1996b, Physics Reports, 266, 229

Chakrabarti, S. K., 1997, ApJ, 484, 313

Chakrabarti, S. K. 1999a, A&A, 351, 185

Chakrabarti, S. K. 1999b, InJPB, 73, 931

Chakrabarti, S. K. 2016, in Proc. of the 14th Marcel Grossmann Meeting on General Relativity 2015, World Scientific, ed. R. Ruffini, R. Jantzen, & M. Bianchi (arXiv: 1604.05955)

Chakrabarti, S. K. & Das, S., 2004, MNRAS, 349, 649

Chakrabarti S. K., Debnath D., Nandi A., Pal P. S., 2008, A&A, 489, L41

Chakrabarti, S. K., & D'Silva, S. 1994, ApJ, 424, 138

Chakrabarti, S.K. & Nandi,A., 2000, Ind. J. Phys., 75(B), 1 (astro-ph/0012526)

Chakrabarti, S.K., & Manickam, S.G., 2000, ApJ, 531, L41

Chakrabarti, S. K., & Molteni, D. 1993, ApJ, 417, 671

Chakrabarti, S.K. & Molteni, D., 1995, MNRAS, 272, 80

Chakrabarti, S.K., Mondal, S. & Debnath, D., 2015, MNRAS, 452, 3451

Chakrabarti, S. K., & Nandi, A. 2000, InJPB, 75, 1

Chakrabarti, S. K., Nandi, A., Manickam, S. G., Mondal, S., Rao, A. R., 2002. ApJ., 579, L21

Chakrabarti, S. K., & Titarchuk, L. G. 1995, ApJ, 455, 623

Chatterjee, D., Debnath, D., Chakrabarti, S. K, et al. 2016, ApJ, 827, 88

Chatterjee, D., Debnath, D., Jana, A., & Chakrabarti, S. K., 2019, Ap&SS, 364, 14

Chatterjee, K., Debnath, D., Chatterjee, D., Jana, A., & Chakrabarti, S. K., 2020a, MNRAS, 493, 2452

Chatterjee, K., Debnath, D., Banerjee, A., et al., 2020b, RAA (submitted) (arXiv:2006.09077)

Chang, K. M., & Ostriker, J. P. 1985, ApJ, 288, 428

Di Salvo, T., Done, C., Zycki, P. T., et al. 2001, ApJ 547, 1024

Capitanio, F., Bazzano, A., Ubertini, P., et al. 2006, ApJ, 643, 376

Capitanio, F., Del Santo, M., Bozzo, E., et al. 2012, MNRAS, 422, 3130

Chatterjee D., Debnath D., Chakrabarti S. K., Mondal S., Jana A., 2016, ApJ, 827, 88

Chatterjee, D., Debnath, D., Jana, A.et al., 2019, AP&SS, 364, 14

Corbel, S., Fender, R. P., Tzioumis, A. K., et al. 2000, A&A 359, 251

Corbel, S., Kaaret, P., Jain, R. K., et al. 2001, ApJ 554, 43

Das, T. K., & Chakrabarti, S. K. 1999, CQGra, 16, 3879

Debnath D., Chakrabarti S. K., Nandi A., 2010, A&A, 520, 98

Debnath D., Chakrabarti S. K., Nandi A., 2013, Adv. Space Res., 52, 2143

Debnath, D., Chakrabarti, S. K., & Mondal, S. 2014, MNRAS, 440, L121

Debnath, D., Jana, A., Chakrabarti, S. K., et al. 2017, ApJ, 850, 92

Debnath, D., Molla, A. A., Chakrabarti, S. K., & Mondal, S. 2015a, ApJ, 803, 59

Debnath, D., Mondal, S., & Chakrabarti, S. K. 2015b, MNRAS, 447, 1984

Debnath, D., Mondal, S., & Chakrabarti, S. K., 2014, MNRAS, 440, L121

Debnath D., Chatterjee D., Jana A., Chakrabarti S. K., Chatterjee K., 2020, RAA, 20, 175

D'Silva, S., & Chakrabarti, S. K. 1994, ApJ, 424, 149

Done, C., Mulchaey, J. S., Mushotzky, R. F. & Arnaud, K. A. (1992), ApJ 395, 275

Done C., Wardziński G., Gierliński M., 2004, MNRAS, 349, 393

Di Salvo T., Méndez M., van der Klis M., Ford E. C., Robba N. R., 2001, ApJ, 546, 1107

Dhawan, V., Mirabel, I. F. and Rodriguez, L. F. 2000, ApJ 543, 373

Eardley, D. M., Lightman, A. P., & Shapiro, S. L. 1975, ApJ, 199, 153

Fabian, A. C., Iwasawa, K., Reynolds, C. S. & Young, A. J. (2000), PASP 112, 1145

Fender, R. P. 2001, MNRAS, 322, 31

Fender, R., Corbel, S., Tzioumis, T., et al. 1999, ApJ 519, L165

Fender, R. & Belloni, T. 2004, ARA&A, 42, 317

Fender, R. P., Belloni, T. & Gallo, E., 2004, MNRAS, 355, 1105

Friedman, H., Lichtman, S. & Byram, E., 1951, Phys Rev., 83, 1025

Frontera, F., Amati, L., Zdziarski, A. A., et al. 2003, ApJ 592, 1110

Fuchs Y. et al., 2003, A&A, 435, L35

Galeev, A. A., Rosner, R., & Vaiana, G. S. 1979, ApJ, 229, 318

Garain S. K., Ghosh H. & Chakrabarti S. K., 2012, ApJ, 758, 114

Garain, S. K., Ghosh, H., & Chakrabarti, S. K. 2013, ASInC, 8,

George, I. M. & Fabian, A. C., 1991, MNRAS 249, 352

Ghosh, A. & Chakrabarti, S. K., 2019, MNRAS, 485, 4045-4051

Ghosh A., Banerjee, I., & Chakrabarti S. K., 2018, MNRAS, 479, 1210

Giacconi, R., Gursky, H., Paolini, F. R. & Rossi, B. B., 1962, PhRvL 9, 439

Giri K., & Chakrabarti S. K., 2013, MNRAS, 430, 2836

Greiner, J., Morgan, E.H. & Remillard, R.A., 1996, ApJ 473, 107

Greiner J., Cuby J. G., McCaughrean M. J. et al. 2001, A&A, 373, L37

Grove, J. E., Johnson, W. N., Kroeger, R. A., et al. 1998, ApJ 500, 899

Haardt, F., & Maraschi, L. 1993, ApJ, 413, 507

Hannikainen, D., Campbell-Wilson, D., Hunstead, R., et al. 2001, ApSSS 276, 45

Hannikainen, D. C., et al. 2005, A&A, 435, 995

Hazard, C., Mackay, M. B. & Shimmins, A. J., 1963, Nature, 197, 1037

Homan, J., Wijnands, R., van der Klis, M., et al. 2001, ApJS 132, 377

Homan J., Miller J. M., Wijnands R. et al., 2005, ApJ, 623, 383

Holzer, T. E., & Axford, W. I. (1970). The Annual Review of Astronomy and Astrophysics, 8, 31

Hoyle, F. & Lyttleton, R. A., 1939, PCPS, 35, 405

Ingram A. & van der Klis M., 2015, MNRAS, 446, 3516

Ingram A., Done C. & Fragile P. C., 2009, MNRAS, 397, L101

Iyer, N., Nandi, A., & Mandal, S. 2015, ApJ, 807, 108

Jahoda, K., Markwardt, C. B., Radeva, Y. et al., 2006, ApJ, 163, 401

Jana, A., Debnath, D., Chakrabarti, S. K., et al. 2016a, ApJ, 803, 107

Jana, A., Debnath, D., Chakrabarti, S. K., et al. 2016b, ApJ, 819, 107

Jana, A., Chakrabarti, S. K. & Debnath, D. 2017, ApJ, 850, 91

Jana, A., Debnath, D., Chakrabarti, S. K., & Chatterjee, D., 2020a, RAA, 20, 28

Jana, A., Debnath, D., Chatterjee, D., et al. 2020b, ApJ, 897, 3

Jana, A., Debnath, D., Chakrabarti, S. K., & Chatterjee, D., 2020, RAA, 20, 3

Janiuk A. & Czerny B., 2005, MNRAS, 356, 205

Janiuk A., Czerny B. & Siemiginowska A., 2000, ApJ, 542, L33

Kahn, S. M. & Blissett, R. J. 1980, ApJ, 238, 417

Klein-Wolt, M., Fender, R. P., Pooley, G. G., et al. 2002, MNRAS, 331, 745

Kozlowski, M., Jaroszynski, M., & Abramowicz, M. A., 1978, Acta Astronomica, 63, 209

Krimm, H. A., Barthelmy, S. D., Baumgartner, W., et al. 2011, ATel, 3144

Krimm H. A., Kennea J. A., 2011, Astron. Telegram, 3148

Kuulkers, E., Lutovinov, A., Parmar, A., et al. 2003, ATel, 149

Lightman, A. P., & Eardley, D. M. 1974. ApJ, 187, 1

Lynden-Bell, D. 1978, Phys. Scri., 17, 185

Klein-Wolt, M., Fender, R. P., Pooley, G. G., et al. 2002, MNRAS 331, 745

Koljonen, K., Vera, R., Lahteenmaki, A., & Tornikoski, M. 2019, The Astronomer's Telegram, 12839, 1

Kong, A. K. H., McClintock, J. E., Garcia, M. R., et al. 2002, ApJ 570, 277

Kubota, A., Makishima, K. and Ebisawa, K. 2001, ApJ 560, L147

Kubota A., Ebisawa K., Makishima K., Nakazawa K., 2005, ApJ, 631, 1062

Kuulkers, E., van der Klis, M., Oosterbroek, T., et al. 1994, A&A, 289, 795

Laor, A. (1991), ApJ 376, 90

Lee, J. C., Reynolds, C. S., Remillard, R., et al. 2002, ApJ, 567, 1102

Liang, E. P. T., & Thompson, K. A. 1980. ApJ, 240, 271

Lightman A. P. & Eardley D. M., 1974, ApJ, 187, L1

Magdziarz P. & Zdziarski A. A., 1995, MNRAS, 273, 837

Malkan M. M. & Sargent W. L. W., 1982, ApJ, 254, 22

Mandelbrot, B. B. 1999, Multifractals and 1/f Noise: Wild Self-Affinity in Physics (Heidelberg,Springer-Verlag)

Markoff, S., Falcke, H. and Fender, R. (2001), A&A 372, L25

Markwardt C. B., Swank J. H., Taam R. E., 1999, ApJ, 513, L37

Martocchia A., Matt G., Belloni T. et al., 2006, A&A, 448, 677

Matsumoto, R., Kato, S., Fukue, J., & Okazaki, A. T. 1984, Publications of the Astronomical Society of Japan, 36, 71

McClintock, J. E., Garcia, M. R., Caldwell, N., et al. (2001), ApJ 551, L147

McClintock, J. E., Narayan, R., Garcia, M. R., et al. 2003, ApJ 539, 435

McClintock J., Remillard R., 2006, in Lewin W., van der Klis M., eds, Compact Stellar X-Ray Sources. Cambridge University Press, p. 157

Mendez, M. and van der Klis, M. 1997, ApJ 479, 926

Merloni, A., Fabian, A. C. and Ross, R. R., 2000, MNRAS 313, 193

Meszaros, P., 1975, A&A, 44, 59

Mikles, V. J., Eikenberry, S. S., & Rothstein, D. M. 2006, ApJ, 637, 978

Miller, J. M., Fabian, A. C., Wijnands, R., et al. (2002a), ApJ 570, L69

Miller, J. M., Fabian, A. C., Wijnands, R., et al. (2002b), ApJ 578, 348

Mineo T. et al., 2012, A&A, 537, 18

Mineshige S., Hirano A., Kitamoto S. J., et al., 1994, ApJ, 426, 308

Mirabel, I. F., Dhaman, V., Chaty, S., et al. 1998, A&A, 330, L9

Misra, R., Yadav, J. S., Verdhan Chauhan, J., et al. 2017, ApJ, 835, 195

Mitsuda K. et al. 1984, PASJ, 36, 741

Miyamoto, S. & Kitamoto, S. 1991, ApJ 374, 741

Miyamoto, S., Kimura, K., Kitamoto, S., Dotani, T., & Ebisawa, K. 1991, ApJ, 383, 784

Mondal S., Chakrabarti S. K., Debnath D., 2015, ApJ, 798, 57

Mondal, S., Chakrabarti, S.K., & Debnath, D., 2016, Ap&SS, 361, 309

Molla, A. A., Debnath, D., Chakrabarti, S. K., et al. 2016, MNRAS, 460, 3163

Molla, A. A., Chakrabarti, S. K., Debnath, D., & Mondal, S. 2017, ApJ, 834, 88

Mondal, S., Debnath, D., & Chakrabarti, S. K. 2014, ApJ, 786, 4

Mondal S., Chakrabarti S. K., Debnath D., 2016, Ap&SS, 361, 309

Molteni D., Lanzafame G. & Chakrabarti S. K., 1994, ApJ, 425, 161

Molteni, D., Sponholz, H., & Chakrabarti, S. K., 1996, ApJ, 457, 805

Motta S., Williams D., Fender R., Titterington D., Green D., Perrott Y., 2019, The Astronomer's Telegram, 12773

Motta, S. E., Kajava, J. J. E., Giustini, M., et al. 2021, arXiv:2101.01187

Morgan, E.H., Remillard, R.A. & Greiner, J., 1997, ApJ 482, 993

Muno, M. P., Morgan, E. H. & Remillard, R. A., 1999, ApJ 527, 321

Nandi, A., Chakrabarti, S. K., Vadawale, S. V. & Rao, A. R., 2001a, A&A, 380, 245

Nandi A., Debnath D., Mandal S., Chakrabarti S. K., 2012b, A&A, 542, A56

Naik, S. & Rao, A.R., 2000, A&A 362, 691

Nandi, A., Manickam, S. G., & Chakrabarti, S. K. 2000a, Indian J. Phys., 74B, 331

Nandi A., Manickam S. G., Chakrabarti S. K., 2000b, preprint (astro-ph/ 0012523)

Nandi, A., Chakrabarti, S. K., Vadawale, S. V. & Rao, A. R., 2001a, A&A, 380, 245

Nandi A., Manickam S. G., Rao A. R., Chakrabarti S. K., 2001b, MNRAS, 324, 267

Nayakshin S. & Rappaport S., 2000, ApJ, 535, 798

Nayakshin S., Rappaport S. & Melia F., 2000, ApJ, 535, 798

Negoro H., et al., 2018, The Astronomer's Telegram, 11828

Nobili L., Turolla R., Zampieri L., Belloni T., 2000, ApJ, 538, L137

Nowak, M. A. 2000, MNRAS, 318, 361

Novikov, I. D. and Thorne, K. S., 1973, in Black Holes, eds. C. DeWitt and B. DeWitt (New York, Gordon & Breach)

Paczyński, B. & Wiita, P. J., 1980, A&A , 88, 23

Pahari, M., Antia, H. M., Yadav, J. S., et al. 2017, ApJ, 849, 16

Pahari, M., Bhattacharyya, S., Yadav, J. S., & Pandey, S. K. 2012, MNRAS, 422, L87

Pahari M. & Pal S., 2010, MNRAS, 409, 903

Pahari, M., Yadav, J. S., Verdhan Chauhan, J., et al. 2018, ApJL, 853, L11

Pal, P.S., Chakrabarti, S.K. & Nandi, A., 2013, AdSpR 52, 740

Pal, P. S., Chakrabarti, S. K., 2015, Advances in Space Research, 56, 1784

Parker, E. N., 1958, ApJ, 128, 664

Peris, P. S., Remillard, R. A., Streiner, J. F. et al., 2016, ApJ, 822, 60

Poutanen, J., & Svensson, R. 1996, ApJ, 470, 249

Pringle, J. E. and Rees, M. J. 1972, A&A 21, 1

Rao A. R., Naik S., Vadawale S. V., Chakrabarti S. K., 2000, A&A, 360, L25

Rao, A., & Vadawale, S. V. 2012, ApJL, 757, L12

Rau A. & Greiner J., 2003, A&A, 397, 711

Reid M. J., McClintock J. E., Steiner J. F. et al., 2014, ApJ, 792, 2

Remillard R. A., McClintock J. E., 2006, ARA&A, 44, 49

Remillard, R. A., Morgan, E. H., McClintock, J. E. et al. 1999, ApJ 522, 397

Remillard, R. A., Sobczak, G. J., Muno, M. P. and McClintock, J. E. 2002, ApJ 564, 962

Revnivtsev, M., Gilfanov, M., Churazov, E., & Sunyaev, R. 2003, ATel, 150

Reynolds, C. S. and Nowak, M. A. (2003), Phys. Rep. 377, 389

Rodriguez, J., Durouchoux, Ph.,Mirabel, I. F., Ueda, Y. et al., 2002, A&A, 386, 271

Rodriguez J., Corbel S., Hannikainen D. C. et al., 2004, ApJ, 615, 416

Rodriguez, J., Corbel, S. & Caballero, I. et al., 2011, A&A, 533L, 4

Rybicki, G. B., & Lightman, A. P., 1979, Radiative Process in Astrophysics, Wiley-VCH Verlag GmbH & Co

Takahashi, K., Inoue, H. and Dotani, T. 2001, PASJ 53, 1171

Salpeter, E., 1964, ApJ, 140, 796

Shakura, N. I. and Sunyaev, R. A. 1973, A&A 24, 337

Shang J. R., Debnath D., Chatterjee D. et al., 2019, ApJ, 875, 4

Shapiro, S. L., 1973, ApJ, 180, 531

Shapiro, S. L. & Salpeter, E. E., 1975, ApJ, 198, 671

Shimura, T. & Takahara, F. 1995, ApJ 445, 780

Singh, K. P., Stewart, G. C., Westergaard, N. J., et al. 2017, JApA, 38, 29

Smith, D. M., Heindl, W. A. & Swank, J. H., 2002, ApJ., 569, 362

Sobczak, G. J., McClintock, J. E., Remillard, R. A., et al. 1999, ApJ 520, 776

Sobczak, G. J., McClintock, J. E., Remillard, R. A., et al. 2000a, ApJ 531, 537

Sobczak, G. J., McClintock, J. E., Remillard, R. A., et al. 2000b, ApJ 544, 993

Sobolewska M. A. & Zýski P. T., 2003, A&A, 400, 553

Stella L., Vietri M., 1999, Physical Review Letters, 82, 17

Stirling, A. M., Spencer, R. E., de la Force, C. J., et al. 2001, MNRAS 327, 1273

Sun W. & Malkan M. M., 1989, ApJ, 364, 68

Sunyaev, R. A. & Titarchuk, L. G., 1980, A&A, 86, 121

Sunyaev, R. A. & Titarchuk, L. G., 1985, A&A, 143, 374

Taam, R., Chen X.-M., Swank, J., 1997, ApJ, 485, 83

Tagger M. & Pellat R., 1999, A&A, 349, 1003

Tananbaum, H., Gursky, H., Kellogg, E., et al. 1972, ApJ 177, L5

Tanaka, Y., Nandra, K. & Fabian, A. C. (1995a), Nature 375, 659

Tanaka, Y., & Lewin, W. 1995b, in X-Ray Binaries, Eds. W. Lewin, J. van Paradijs, & P. van den Heuvel, Cambridge Univ. Press, Cambridge, 126

Takahashi, K., Inoue, H. & Dotani, T. (2001), PASJ 53, 1171

Thorne, K. S. & Price, R., 1975, ApJ 195, L101

Tomsick, J. A., Kaaret, P., Kroeger, R. A. and Remillard, R. A. 1999, ApJ 512, 892

Trudolyubov S. P., 2001, ApJ, 558, 276

Trushkin, S. A., Nizhelskij, N. A., Tsybulev, P. G., Bursov, N. N., & Shevchenko, A. V. 2019, The Astronomer's Telegram, 12855, 1

Ueda Y., Yamaoka K., Remillard R., 2009, ApJ, 695, 888

Vadawale, S.V., Rao, A.R., Nandi, A. & Chakrabarti, S.K., 2001, A&A 370, 17

Vadawale, S.V., Rao, A.R., Naik, S., et al., 2003, ApJ 597, 1023

Vadawale, S. V., Chattopadhyay, T., Rao, A. R. et al., 2015, A&A., 578, A73.

Vierdayanti K., Mineshige S., Ueda Y., 2010, PASJ, 62, 239

Wu et al., 2002, ApJ., 565, 1161

Wilms, J., Nowak, M. A., Dove, J. B., et al. 1999, ApJ 522, 460

Yadav, J.S., Rao, A.R. & Agrawal, P.C., 1999, ApJ 517, 935

Yadav, J. S. 2001, ApJ, 548, 876

Yadav J. S., 2006, ApJ, 646, 385

Yadav, J. S., Agrawal, P. C., Antia, H. M., et al. 2016a, Proc. SPIE, 9905, 99051D

Yadav, J. S., Mishra, R., Chauhan, J. V., et al. 2016b, ApJ, 833, 27

Zeldovich, Y. B. & Novikov, I. D., 1971, Relativistic Astrophysics (University of Chicago Press, Chicago)

Zdziarski A. A., Grove J. E., Poutanen J. et al., 2001, ApJ, 554, L45

Zdziarski, A. A., Lubinski, P., Gilfanov, M., et al. 2003, MNRAS, 342, 355

Zhang, S. N., Cui, W. and Chen, W. 1997, ApJ 482, L155